The fabrication and property investigation of graphene and carbon nanotubes hybrid reinforced Al_2O_3 nanocomposites

Submitted by

Bahareh Yazdani

To the University of Exeter as a thesis for the degree of Doctor of Philosophy in Engineering

October 2015

I certify that all material in this thesis which is not my own work has been identified and that no material has previously been submitted and approved for the award of a degree by this or any other University.

Signature: ……..

Abstract

In the last decade, carbon nanotubes (CNTs) and Graphene nanoplatelets (GNPs) have attracted a lot of attentions in various polymeric and ceramic composite systems, in an effort to improve their mechanical and functional properties. Al_2O_3 has attracted considerable interests in ceramics community, in particular as a matrix material for composite fabrications. The high stiffness, excellent thermal stability and chemical resistance of Al_2O_3 make it practically a very important engineering material, and if we can overcome its brittleness issue, its applications will be much wider. Adding CNTs as a reinforcement to the Al_2O_3 matrix to improve the toughness is one of the most promising methods. Similarly, GNPs have recently also been shown to be very promising for the same purpose. It has been demonstrated that by adding a mixture of the 2D-GNPs and 1D-CNTs into a polymer matrix, the toughest or strongest man-made ropes have been made. However, the homogenous dispersion of CNTs or GNPs is more of a challenge in a ceramic matrix than in polymeric matrices, owing to the tendency of CNT agglomerations and more steps are needed to completely transfer the useful properties of CNTs and GNPs into ceramics.

In this thesis, nanocomposites of Al_2O_3 reinforced with a hybrid of GNTs (a blend of GNPs and CNTs) were first fabricated. The hybrid GNT reinforcements were mixed with the Al_2O_3 using a wet chemical technique under ultrasonic treatment. The effects of varied GNT contents on the microstructural features and mechanical properties of the nanocomposites were then investigated. It is found that the well-dispersed GNT fillers resulted in high sintered densities (>99%) in the composites, whilst the fracture mode alteration, grain refinement and improved flexural strength of the composites are all associated with the inclusion of CNTs and GNPs. The average fracture toughness of the nanocomposites reached up to 5.7 $MPa \cdot m^{1/2}$, against 3.5 $MPa \cdot m^{1/2}$ of the plain Al_2O_3, and the flexural strength improved from 360 MPa to 424 MPa respectively, at a hybrid addition of 0.5 wt% GNPs and 1 wt% CNTs. The toughening mechanisms attributed with the unique morphologies and structures of the GNT fillers were also discussed based on analyses on the morphology, grain sizes and fracture mode.

The effects of hot-pressing (HP) and spark plasma sintering (SPS) methods on the grain size, microstructural features, and mechanical behaviour of GNT-reinforced Al_2O_3 nanocomposites were then comprehensively studied. Identical overall reinforcement contents at various GNP/CNT ratios were selected to prepare the composites using both HP and SPS. Highly densified samples (>98%) were obtained at 1650°C under 40 MPa in Ar atmosphere, with dwell times of 1 h and 10 min for HP and SPS respectively. Both types of sample showed a mixture of inter- and trans-granular fracture behaviour. A 50% grain size reduction was observed for samples prepared by HP, compared with the SPS samples. Both types of samples achieved a high flexural strength and fracture toughness of > 400 MPa and 5.5 $MPa \cdot m^{1/2}$, respectively, whilst the properties of the SPS samples peaked at relatively lower GNT contents than those of the HP samples. Based on analyses of the morphology, grain sizes and fracture mode, similar toughening mechanisms for both types of sample were observed, involving the complex characteristics of the combined GNT fillers.

The tribological performance of the HPed pure Al_2O_3 and its composites containing various hybrid GNT contents was further evaluated under different loading conditions using a ball-on-disc method. Benchmarked against the pure Al_2O_3, the composite reinforced with a 0.5 wt% GNP exhibited a 23% reduction in the friction coefficient along with a promising 70% wear rate reduction, and a hybrid reinforcement consisting of 0.3 wt.% GNPs + 1 wt.% CNTs resulted in even better performance, with a 86% reduction in the wear rate. The extent of damage to the reinforcement phases caused during wear was studied using Raman spectroscopy. The wear mechanisms for the composites were analysed according to the mechanical properties, brittleness index and microstructural characterization. The combination between GNPs and CNTs contributed to the excellent wear resistance properties for the hybrid GNT-reinforced composites. The GNPs played an important role in the formation of a tribofilm on the worn surface by exfoliation; whereas the CNTs contributed to the improvement in fracture toughness and prevented the grains being pulled out during the tribology test.

Finally, Graphene Oxide (GO) was used to replace the GNPs in the hybrid, to prepare Al_2O_3-GONT nanocomposites, by adopting a new sol-gel processing, in addition to powder mixing. It has been found that sol-gel process leads to an impressive grain size reduction of 62%, the fracture toughness and flexural reached 6.2 $MPa \cdot m^{1/2}$ and

420 MPa (i.e. 70% and 14% improvement), respectively, than those of pure Al_2O_3, which even marginally outperformed the previously optimised Al_2O_3-GNP nanocomposites by 8% in fracture toughness. The success of our new sol-gel strategy opens up new opportunities for choosing hybrid reinforcements for the fabrication of advanced ceramic nanocomposites.

Peer reviewed journal papers

- **Bahareh Yazdani**, Fang Xu, Iftikhar Ahmad, Xianghui Hou, Yongde Xia, Yanqiu Zhu, Tribolological performance of Graphene/Carbon nanotube hybrid reinforced Al_2O_3 composites, *Scientific reports 5,* 2015.

- **Bahareh Yazdani**, Harshit Porwal, Yongde Xia, Mike J. Reece, Haixue Yan, Yanqiu Zhu, Role of synthesis method on microstructure and mechanical properties of Graphene/carbon nanotube toughened Al_2O_3 nanocomposites, *Ceramics International,* 2015, 41, 9813–9822.

- **Bahareh Yazdani,** Yongde Xia, Iftikhar Ahmad, Yanqiu Zhu, Graphene and carbon nanotube (GNT)-reinforced alumina nanocomposites, *Journal of the European Ceramic Society,* 2015, 35, 179–186.

- Iftikhar Ahmad, **Bahareh Yazdani**, and Yanqiu Zhu, Recent Advances on Carbon Nanotubes and Grapheme Reinforced Ceramics Nanocomposites, *Nanomaterials* 2015, 5, 90-114.

- Iftikhar Ahmad, Mohammad Islam, AbdulhakimA. Almajid, **Bahareh Yazdani**, Yanqiu Zhu, Investigation of yttria-doped alumina nanocomposites reinforced by multi-walled carbon nanotubes, *Journal of Ceramic International*, 2014, 40, 9327–9335.

- Iftikhar Ahmad, Mohammad Islam, Hany Sayed Abdo, Tayyab Subhani , Khalil Abdelrazek Khalil, Abdulhakim A. Almajid, **Bahareh Yazdani**, Yanqiu Zhu, Toughening mechanisms and mechanical properties of graphenenanosheet-reinforced alumina, *Journal of Materials and Design,* 2015, 88, 1234–1243.

Conference presentations

- Bahareh Yazdani, Y.Q. Zhu, Graphene and carbon nanotube (GNT)-reinforced alumina nanocomposites**,** European Congress and Exhibition on Advanced Materials and Process, September 2013, Seville, Spain.

- Bahareh Yazdani, Yongde Xia, Yanqiu Zhu, New process to produce Carbon nanotube and graphene (GNT)-Ceramic nanocomposites with improved mechanical properties, The 21st Joint Annual Conference of CSCST-SCI, October 2014, University of Surrey, UK.

- Bahareh Yazdani, Yanqiu Zhu, and Yongde Xia, New approach to produce highly dispersed graphene oxide-carbon nanotube hybrid reinforcement into alumina matrix, 2nd China International Congress on Composite Materials CCCM-2, 2015.

Contents

Acknowledgments

I would like to express my thanks to Professor Yanqiu Zhu for his guidance, daily support and encouragements without which this research and subsequent thesis would not have existed. His attitude, enthusiasm and insight in the research are appreciable and will always be source of inspiration and motivations.

I wish to give thanks to Dr Xia Yongde for his support and Imaging suit staff: Drs Lesley Wears and Hong Chang for their constant help on equipment. Thanks to Dr Yat-Tarng (Tommy) Shyng for his assistance on mechanical testing. I am grateful to Professor Mike Reece and Dr Harshit Porwal of Queen Marry University of London for assistance with the SPS experiments. My thanks also go to Professor Xianghui Hou and Dr Fang Xu of The University of Nottingham for the assistance in the tribological tests. Special thanks go to Professor Iftikhar Ahmad of the Advanced Manufacturing Institute, King Saud University, for his advice and collaborations. Special thanks to University of Exeter for the scholarship support.

I appreciate the friendship and technical help from group members: Dr Zhuxian YANG, Dr Chunze Yan, Dr Sakineh Chabi, Mr Binling Chen, Mr Nannan Wang, Ms Thummavichai Kunyapat and Mr Deng Laicong.

My deepest gratitude goes to my parents, my husband and my daughter for their love, caring, understanding and moral support. They are the most important people in my world and I dedicate this thesis to them. Admirable thanks to my beloved husband who did a fantastic support during my PhD.

List of Figures and Tables

List of Abbreviations

CNT	Carbon nanotube
GNP	Graphene nanoplatelet
GNT	A blend of GNP and CNT
GO	Graphite oxide
GONT	A blend of GO and CNT
1D	One-dimensional
2D	Two-dimensional
HP	Hot-pressing
SPS	Spark plasma sintering
TEM	Transmission electron microscope
HRTEM	High-resolution Transmission electron microscope
MWCNT	Multi-walled nanotube
SDS	Sodium dodcyle sulphate
SDBS	Sodium dodecyl benzene sulfonate
DMF	Dimethylformamide
NMP	N-Methyl-2-pyrrolidone
SEM	Scanning electron microscope
SENB	Single edge notched beam
SWCNT	Single-walled nanotube
XRD	X-ray diffraction
UT	Ultrasonic
BM	Ball mill

Chapter 1 Introduction

Among structural ceramics, Al_2O_3 is one of the most used materials in industry due to its superior hardness, chemical inertness and electrical/thermal insulation properties. These useful characteristics make Al_2O_3 suitable for a wide range of functional applications, such as high speed cutting tools[1], dental implants, chemical and electrical insulators[2], armouries[3], wear resistant parts and various coatings[4,5]. However, the extremely brittle nature of Al_2O_3 has restricted it being used in numerous structural applications, such as in aircraft engine parts, rocket materials surviving in extreme environments and other space engineering applications[6]. The inferior fracture toughness of Al_2O_3 is attributed to the presence of impurities, pores and cracks formed during sintering; the elimination of such processing flaws in monolithic Al_2O_3 is extremely expensive and advanced processing technology is thus required. An alternative and practical way to convert Al_2O_3 into a more useful material is to fabricate composites. The most promising approaches to overcoming this deficient during last decades are by way of second phase additions, such as by introducing particulates ranging from metals (Fe[7], Mo[8], Cr[9], and Ni[10]), to ceramics (ZrO_2[11], MgO[12], and SiC[13]), long or short fibres such as carbon fibres[14,15], and moderate improvements in the fracture toughness have been reported. Recent advances in nanoresearch have produced numerous new nanomaterials possessing extraordinary properties. Accordingly, some of these nanomaterials with distinct morphologies and properties have been used to reinforce monolithic ceramics[16]. In particular, the exceptionally high mechanical properties and outstanding multifunctional features of CNTs have made them the wonder materials, standing out from many other nanomaterials, among different research communities. To date, CNT-reinforced ceramic nanocomposites have been reported to convert them into tough, strong, electrically and thermally conductive materials[17-22]. CNT-reinforced Al_2O_3 nanocomposites have shown wide variations in density, flexural strength, hardness and fracture toughness[23]. Consistently improved mechanical properties at a low addition of CNTs (< 2 wt%) have been obtained, however widely-scattered values for the fracture toughness are also observed, especially when the CNT content is high (> 2 wt%)[21,24,25]. This phenomenon was believed to have

arisen from porosity in the composites, lack of uniformity in the CNT dispersion, weak interfacial connections and possible damage to the CNTs[26,27].

The leading challenge in ceramic-CNT nanocomposites manufacturing is the homogenous dispersion of CNTs, because CNTs tend to agglomerate due to their high aspect ratio (length/diameter) and strong Van der Waals interactions. The main causes of inferior quality of nanocomposites are CNT agglomerations and weak interfaces between the CNT and matrix. In most cases, the additions of CNT as reinforcements improved the fracture toughness, but decreased the hardness and strength. Achieving a homogenous dispersion of CNTs in ceramics, with strong bonding between the CNT and matrix, represents rather more of a challenge than incorporating CNTs into a polymer.

Graphene, known as a monolayer of carbon atoms arranged in a honeycomb lattice, has shown similar properties to CNTs with impressive thermal, mechanical, and electrical properties, and is a promising alternative to CNTs in various applications[28,29]. Compared with CNTs, graphene also has large specific surface areas and it does not form agglomerates in a matrix when handled appropriately, thus an ideal nano-filler for composite materials. In this regard, the low-cost, high quality and commercially more viable a-few-layer-thick graphene nanosheets, designated as graphene nanoplatelets (GNPs) are more promising for practical engineering applications, thus attracting considerable research interests for advanced ceramic matrices. Indeed, various crucial ceramics such as Al_2O_3, Si_3N_4 and ZrO_2 have been reinforced by the GNP fillers and obvious improvements in fracture toughness, thermal and electrical properties have been obtained[30-36]. However, research into ceramic-GNP nanocomposites is in its infancy, and more thorough and systematic studies are required. Further, an hybrid filler by combining the advantages of 1-D and 2-D reinforcements may lead to further improved properties in ceramic-based nanocomposites. Indeed, this concept has recently been pioneered in polymer-based composites, and the synergetic effect through hybridization of CNTs and GNPs resulted in the toughest and strongest man-made polymer nanocomposite ropes[37-41]. Inspired by this idea, to explore the effects of the hybrid reinforcement of GNPs and CNTs, namely GNTs, in a ceramic matrix is very interesting to overcome the challenge of CNT dispersion difficulties in ceramic matrixes by tailoring the roles of both GNPs and CNTs in toughening Al_2O_3 matrix, to obtain super tough Al_2O_3-GNT

nanocomposites. Furthermore, recent studies have proven that GO, with the hydrophilic oxidation groups on graphene surface, can be readily dispersed into water to form stable colloidal suspensions, and it can be used to disperse CNTs in an aqueous solution via non-covalent interactions without any surfactant agents and polymer dispersants[42,43]. By changing the weight ratio between GO and CNTs, a hydrogel of GO/CNT can form, which indicates the strong π-π interactions. This strong synergetic effect between the GO and CNTs can be a new route to overcome the key challenge in CNT dispersion in ceramic-based composites. They have mainly been synthesized in bulk form for energy storage applications including lithium ion batteries[44], supercapasitors[45], or water purifications[46], and less attentions have been made on using such GONT hybrid reinforcement in composites. Indeed, there are few reports on applying GO and CNTs as a hybrid reinforcement into polymer matrixes[37], but there is no report on applying this synergetic hybrid reinforcement in ceramic matrixes for improved functional properties.

In the last few decades, Al_2O_3 is increasingly being used in sliding components such as bearings, cylinders liners, valve seats, piston rings in automobile engines and mechanical seals[6,47]. However, the low fracture toughness of Al_2O_3 remains a stumbling block for combined applications in tribological environments. To fill this technological gap, ceramics reinforced with carbon fibers have been considered and it was found that such composites not only reduced the risk of fracture but also lowered the friction coefficient through self-lubrication[48]. To date, extensive research has been reported regarding enhancing the fracture toughness of ceramics matrices however, less attention was paid to explore their potential tribological features. Some tribological properties of CNT- and/or GNP-reinforced ceramic nanocomposites have been reported, and a significant reduction in wear volume has been achieved[23,49,50]. Therefore, the complete understanding for the tribological performance of Al_2O_3-based nanocomposites requires further research.

This thesis has been organized into eight chapters. Chapter 1 introduces the motivation, objectives and organization of the thesis. Chapter 2 consists of literature review for Al_2O_3-CNT nanocomposites and Al_2O_3-GNP nanocomposites. Chapter 3 describes the various techniques employed in this research, to investigate the structure and properties of the nanocomposites.

Chapter 4 presents the fabrication of the Al_2O_3-GNT nanocomposites, including methods adopted for the dispersion of GNT within the matrix. Al_2O_3-GNT nanocomposites with various GNP/CNT ratios have been prepared, to obtain the optimum GNT content in terms of structural features and mechanical properties. Two sintering techniques, Hot-press and SPS, were selected to prepare the nanocomposites, and the structural features of the resulting nanocomposites also will be described in this chapter. Chapter 5 investigates the mechanical properties of the Al_2O_3-GNT nanocomposites, including the toughening mechanisms of nanocomposites at various GNP/CNT ratios. Chapter 6 assesses the role of GNT contents on the tribological performance and wear properties of the nanocomposites under various loads, and also investigates the wear mechanism.

Chapter 7 describes the synthesis and characterisation of Al_2O_3-GONT nanocomposites, using a blend of GO and CNTs as the reinforcement. The effect of various GO/CNT ratios on the structural features and mechanical properties has been investigated and toughening mechanisms analysed.

Finally, the conclusions of this thesis are summarised in Chapter 8.

Chapter 2 Literature review

2.1 Introduction

This chapter describes the main research progresses of the CNT- and GNP-reinforced composites. First, I focus on CNT-reinforced nanocomposites and their toughening mechanisms, and then move onto the GNP-reinforced nanocomposites. The mixing techniques, sintering methods, mechanical and other functional properties will be summarised.

2.2 CNT-Reinforced Ceramic Nanocomposites

Ceramics are potential contestants for diverse sophisticated engineering applications, and a plenty of attentions have been focused onto further improving their properties by adopting emerging technologies. As a result, much deeper understandings and significant amounts of improvement in their structures and properties have been achieved after decades of effort. However, many challenging issues limit their wide applications, such as the degradation of high temperature mechanical properties of non-oxide Si_3N_4 and SiC, and low fracture toughness, poor creep, thermal shock resistance of oxide ceramics like Al_2O_3 and ZrO_2[51].

Among structural ceramics, Al_2O_3 as one of the most used materials in industry has found some niche applications, from high speed cutting tools, dental implants, chemical and electrical insulators, to wear resistance parts and various coatings, due to their high hardness, chemical inertness and high electrical and thermal insulating properties[4]. The intrinsic low fracture toughness restricts ceramics from applications in aircraft engine parts and in extreme environments for space engineering[6]. For decades, the addition of a second reinforcing phase in ceramics has been an effective way to improve their toughness, converting brittle ceramics to practical engineering materials.

Recent advances in nanomaterials have offered the opportunity to tailor the ceramic structures at nanometre scale, for the development of new classes of stronger, tougher engineering ceramics with added functionalities. Some nanomaterials with distinct morphologies and properties have been investigated

to reinforce monolithic ceramics, and these nanomaterials include nanoparticles, nanorods and nanoplates[52] (Fig. 2.1 a-c). It is expected that these reinforcements could either deflect the crack propagations or provide bridging elements, so that hindering further opening of the cracks. Another concept is to incorporate metallic ligaments into the ceramic matrix, to form crack bridging elements that absorb energy by plastic deformations.

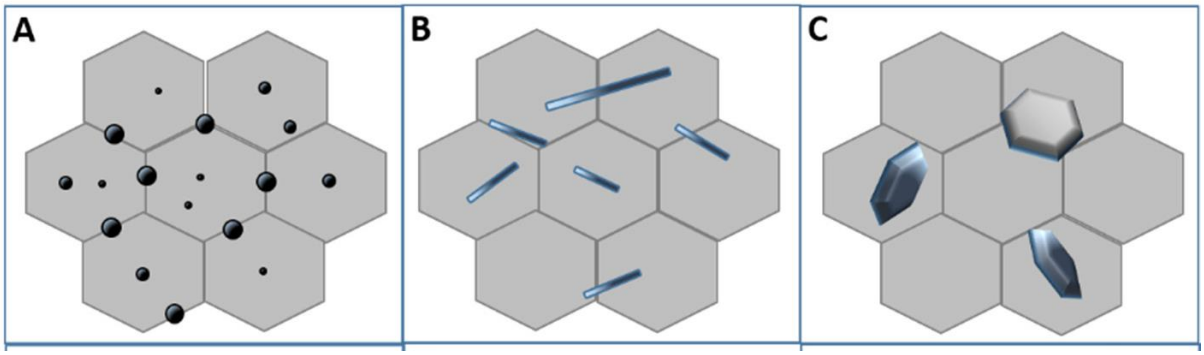

Fig. 2.1 Scheme of common (nano)composite structures for ceramic materials, (a) Micro/nano composite, with rounded nanoparticles occupying both inter- and intra-granular positions inside a micronic matrix; (b) Micro/nano composite, with elongated nanometre scale reinforcements embedded in a micronic matrix; (c) Micro/nano composite, with platelet-like nano-reinforcements embedded in a micronic matrix[52].

Since Ijima discovered CNTs[53], their exceptional mechanical properties (Young's modulus~1 TPa and tensile strength up to 60 GPa) and outstanding multifunctional features made them a wonder material, standing out from many other nanomaterials. For example, CNTs are extremely flexible under large strains, and can resist failure under repeated bending[54]. Accordingly, the ceramic community rapidly considered of using CNTs as reinforcements for brittle ceramic matrices, hoping to create novel engineered ceramic matrix composites (CMCs) with superior mechanical performance and tailored thermal and electrical properties. Many documented researches reported to incorporate a type of CNT (multi-walled or single-walled) in brittle ceramics to convert them into tough, strong, electric and thermal conductive materials[20,21,25,55-58], as shown in Fig. 2.2 b.

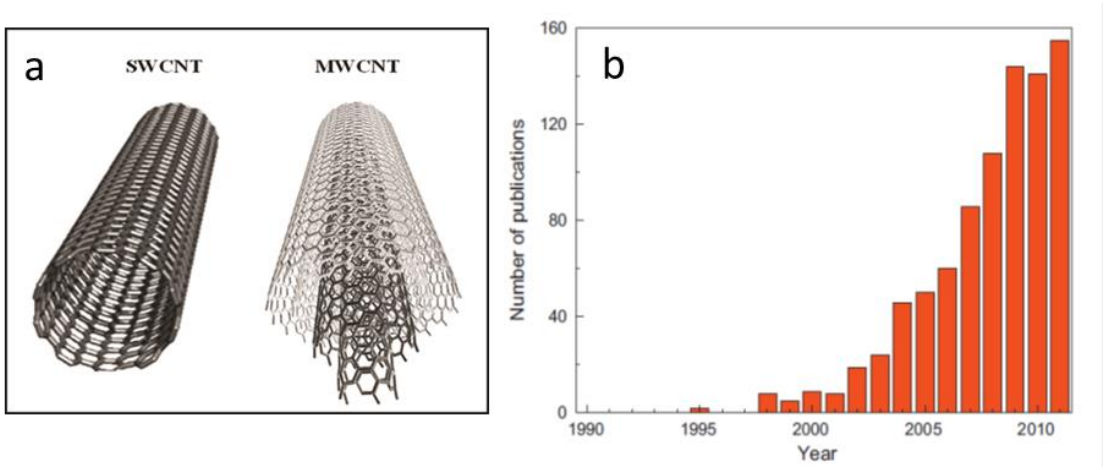

Fig. 2.2 (a) The simulated model of an ideal SWCNT and MWCNT, (b) a histogram of CNT-reinforced CMCs publications in the last 20 years. Source: ISI Web of Knowledge.

2.3 The toughening mechanisms of CNT-ceramic composites

The reinforcement (fibres or whiskers) pull-out is the main toughening mechanism in conventional ceramic composites, which is further associated with the weak interfacial connections between the reinforcement and the matrix.

This classical approach was logically proposed to explain the toughening mechanism in CNT-reinforced ceramic composites in several initial reports. However, in later research Padture et al. and many others observed that the microstructural features of CNT-ceramics were immensely dissimilar from those of conventional composites, and these new observations strongly suggested that the existing microscale mechanism may not be fully applicable to the new nanoscale CNT–ceramic systems[59,60]. The microstructure of conventional ceramic composites consists of inflexible and straight reinforcements that are two to five orders of magnitude larger than CNTs, and their interface is optimally designed in such a way that it deboned on applied loads, as shown in Fig. 2.3. Imagine, when a reinforcement encounters a crack, it then bridges the crack in its wake, and its pull-out does the frictional work. These actions together effectively make the crack propagation more difficult than in plain ceramics. Specifically, the large dimensions of the reinforcement lead to a longer crack-wake bridging zone than nanoscale reinforcements, and consequently they worked effectively to result in higher toughness. However, these large

reinforcements prompt larger flaws, therefore turning the strength to lower values[61].

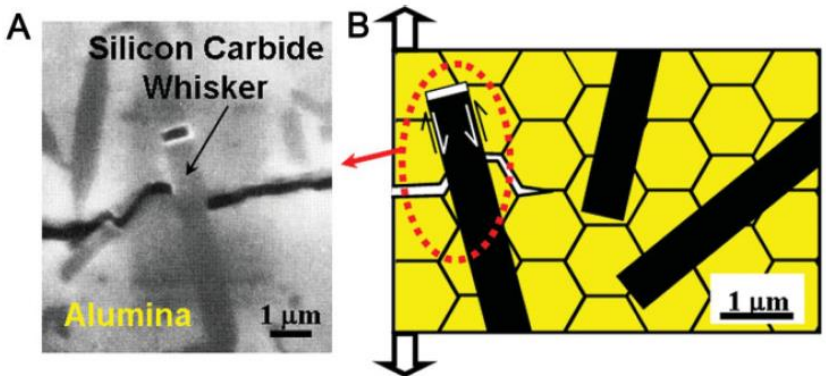

Fig. 2.3 a) SEM image of a SiC whisker in Al_2O_3 matrix, and (b) a schematic showing the frictional pull-out and the crack bridging in a composite[17].

In contrast, CNTs are highly flexible, hollow, and nanometre sized fibres, therefore the toughening mechanism may be entirely different from the conventional micro-sized ones, and the frictional pull-out mechanism may not be true in this case. Accordingly, new concepts and philosophies of uncoiling and elastic stretching of CNTs during the crack propagation were proposed as the new toughness mechanisms by Padture et al.[17]. During the crack propagation, an initial uncoiling of CNTs occurs in the crack wake, and when the crack further propagates, the uncoiled CNT stretches elastically, serving as stretched CNT bridges instead of conventional frictional pull-out bridges. Thus, they impede the crack propagation, as shown in Fig. 2.4, through the stage of crack propagation. During deformation, the CNT reinforcements can absorb energy through their highly flexible elastic behaviour, so that they can increase the fracture toughness, which is especially important for nanotube-based CMCs. These concepts are convincingly identified the role of CNTs in CMCs, as an individual entity which can be further extended to their cluster form.

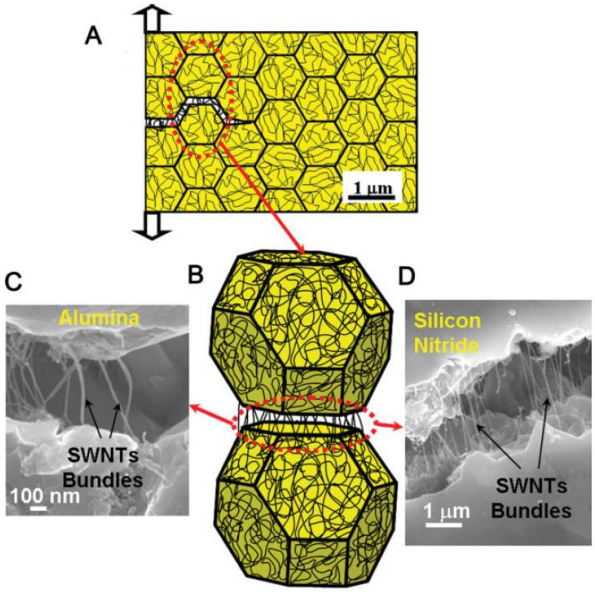

Fig. 2.4 The proposed toughening mechanisms in CNT-ceramic nanocomposites. (a) A model of an inter-granular crack within the ceramic matrix, (b) A schematic toughening within ceramic grains, and (c, d) SEM images of the CNT bridging the crack in Al_2O_3-CNT nanocomposites[17].

2.4 Graphene – reinforced ceramic composites

2.4.1 Graphene synthesis

Graphene was first produced by micromechanical cleavage of graphite using a simple scotch tape in 2004 [28]. Other methods to fabricate graphene include chemical vapour deposition and growth on crystalline SiC substrate[62,63]. While these approaches can yield a largely defect-free material with exceptional physical properties, they are not really suitable for the preparation of graphene containing composites which require a large amount of samples for the fabrication.

Recently, a new cost-effective, high-quality carbon-based phase was developed in the form of graphene platelets, also called graphene nanoplatelets (GNPs) or multilayer graphene nanosheets[64]. This offers an excellent alternative to the more expensive nanotubes for composite applications. These platelets usually contain several graphene layers, in contrast to the mono-layered graphene. Typically, GNPs can be produced by the mechanical exfoliation[65], or by the reduction of GO[66], in high volume, which satisfies the demand for composite applications.

Mechanical exfoliation:

In the mechanical exfoliation or mechanical cleavage, a commercial graphite powder was milled intensively in a high efficient attritor mill, in the presence of ethanol, for 10 h [65], which leads to the production of GNPs at grams level.

Hummer's method:

In the Hummers method[66], a commercially available graphite powder was treated with sulphuric acid (H_2SO_4) and potassium permanganate ($KMnO_4$), to induce functional hydroxyl groups on the graphite surfaces and interfaces (Fig. 2.5), to form GO. The interlayer spacing in GO increased from 0.336 nm in graphite to 0.6-1 nm, depending on the humidity due to the existence of these functional groups. Additionally, GO is suitable for large scale and cost-effective production, which is the key factor for composite preparations. In particular, GO can be exfoliated in water due to the hydroxyl group, thus it is a favourable characteristic for composite preparation using water-soluble methods to obtain good distribution in the matrix.

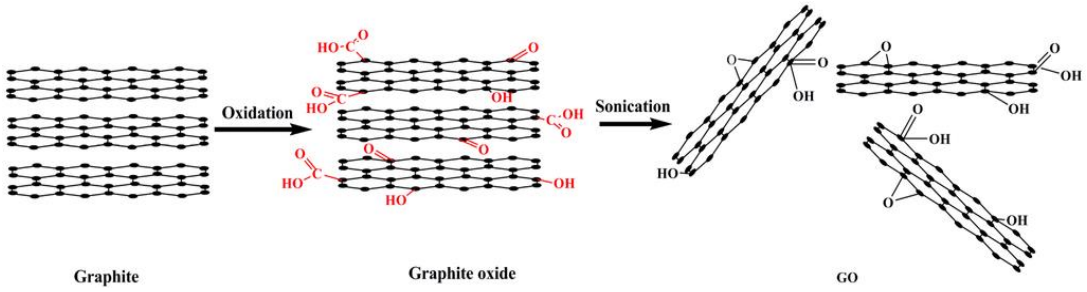

Fig. 2.5 Scheme of GO preparation by Hummer's method[67].

In general, both the mechanical exfoliation and Hummer's methods suffer from different problems. For instance, there is not enough control over the quality of the GNPs prepared by high energy milling, and the resulting GNPs have various sizes and thicknesses (layer numbers), which would pose negative effects on the final properties of CMCs. The oxidation in the Hummer's process causes damage to the GO, and the high level of structural defects in the flakes would degrade the properties in composites. Thus, these issues need to be solved to achieve better

control over the structural and chemical quality of GNPs. This will be discussed in the ceramic-GNP dispersion techniques in section 2.5.

2.4.2 Graphene microstructure and properties

Graphene is a monolayer of sp^2-hybridized carbon atoms arranged in a two-dimensional lattice. There are three in-plane (σ) bond atoms. These bonds are extremely strong and form the rigid backbone of the hexagonal structure (Fig. 2.6). The π orbitals are perpendicular to the plane, and the out-of-plane π bonds control interaction between different graphene layers and are responsible for the electron conduction[63].

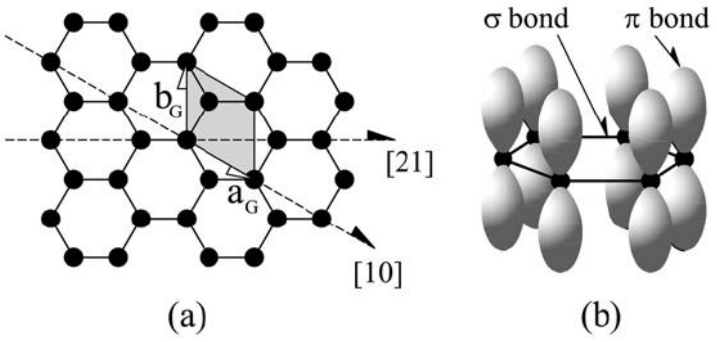

Fig. 2.6 (a) Graphene hexagonal structure of identical carbon atoms, and (b) Schematic of the in-plane σ bonds and the π orbitals perpendicular to the plane of the sheets[63].

This 2D material was characterised to possess exceptional electrical, mechanical and thermal properties. It was verified that those electrons move ballistically within graphene layers with a mobility which exceeds 200,000 $cm^2\ V^{-1}\ s^{-1}$. Besides that, the graphene was found to have unique thermal conductivity: ~ 5300 W/mK. It has superior mechanical properties, with Young's modulus of approximately 0.5–1.0 TPa. Interestingly, despite of their non-perfect structure, the suspended GO sheets retained an impressively high Young's modulus of 0.25 TPa. These values imposed graphene as a promising alternative of CNTs in several applications ranging from nano-electronics to sensing devices[68], and to nanocomposites.

These properties suggest that graphene can be applied as an excellent reinforcement to ceramic materials, and it is expected that their addition will significantly improve the properties of the final composites.

2.4.3 GNP-ceramic toughening mechanisms

Evaluating the toughening effects of reinforcement in CMCs is one of the main objectives of the ceramic community, due to the brittleness problem in ceramics. GNPs have similar mechanical properties to CNTs, with larger surface areas and better dispersion properties than CNTs, thus appear to be an ideal alternative to replace CNTs in CMCs. Tapaszto et al. have showed that GNPs were easier to process and disperse in Si_3N_4, compared with CNTs, thus resulted in better mechanical properties than using the same amount of CNTs in the composites, although both have improved the facture toughness[30]. However, it should be noted that the interface between the GNPs and the matrix may have played a more important role in the toughening mechanisms than other factors.

Similar to CNTs, literatures to date have shown that GNPs offer the same effective grain bridging and pull-out toughening mechanisms during crack propagation. However, a new toughening mechanism has recently been introduced based on the flexible 2D structural feature of the GNPs, to account for the improving effect, called anchoring effect[34]. As seen in Fig. 2.7, the GNP flake can roll up around the ceramic grains, hence increasing the required energy to be pulled-out during the crack propagation. Given the larger contact areas, it is believed to be more effective than that of CNTs. This new toughening mechanism can considerably improve the fracture toughness in GNP-ceramic composites. In the case of strong bonding between graphene and the matrix, the high strength and increased contact areas of graphene will hinder a crack to propagate through and if the crack eventually manages to propagate, it has to take a more tortuous route.

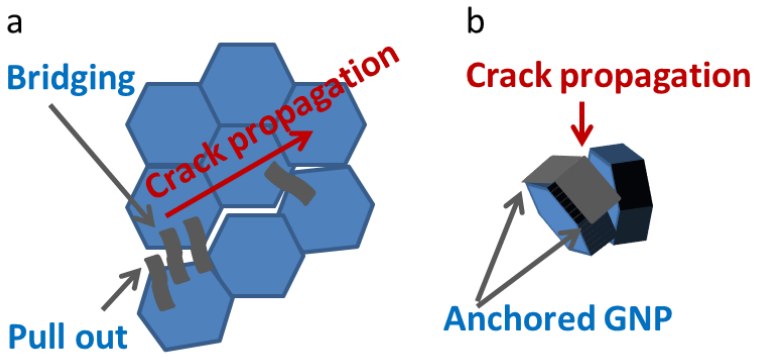

Fig. 2.7 A model of the proposed anchoring toughening mechanism induced by graphene anchored with various ceramic matrix grains.

Recently, Walker et al. reported a fracture toughness improvement of 235% with only 1.5 vol% graphene addition in a Si_3N_4-GNP composite[34]. Fig. 2.8c shows a large platelet that lies along the grain boundaries of the matrix. The long and continuous GNP appears failed to deflect the crack propagation path in-plane, however the crack indeed does not break or penetrate through the GNP neither. Therefore, the crack seems to be arrested at the GNP and has to change directions, i.e., negotiates with the GNP and undergoes an out-of-plane deflection. Fig. 2.8d is an SEM image of a fractured surface at a different location of the same nanocomposite, and it shows how the GNP (at the centre of the image) is anchored securely at the matrix grain boundaries. This is the first time that such a toughening mechanism was evidenced.

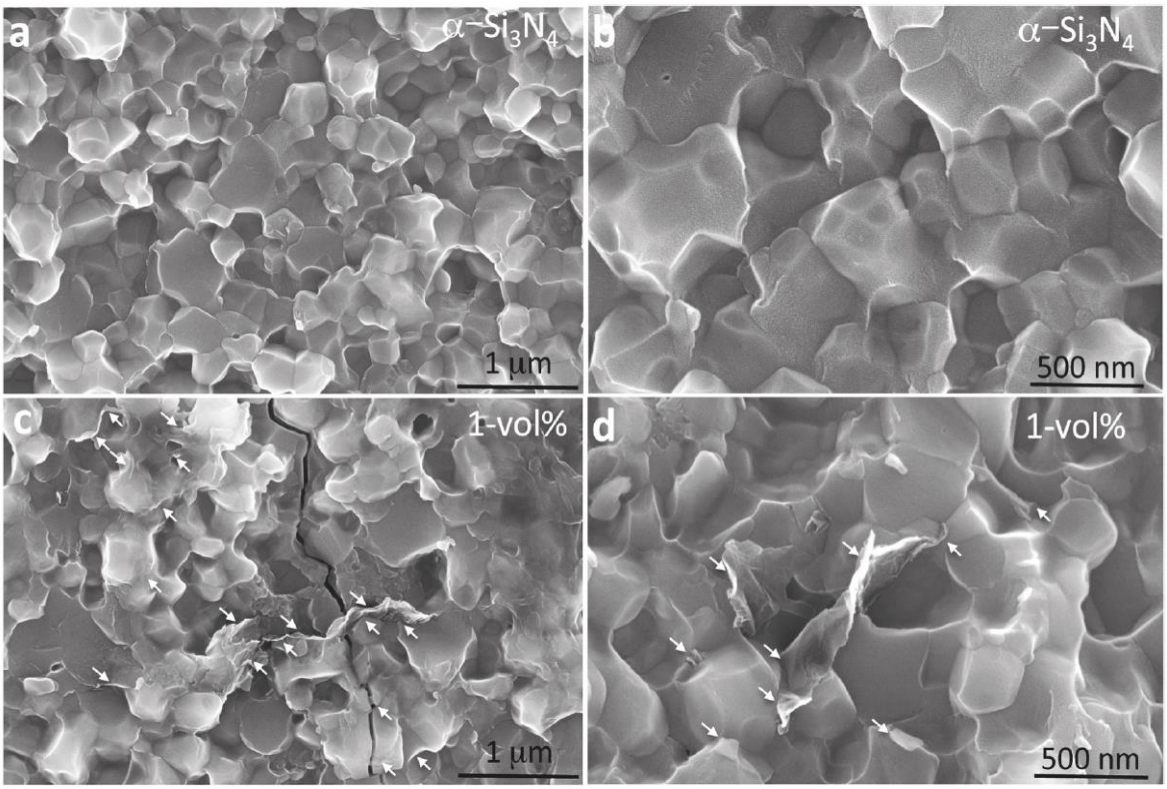

Fig. 2.8 SEM images from fractured surface of Si_3N_4-GNP nanocomposites. (a) Low- and (b) high-magnification images of the high-density monolithic Si_3N_4 showing an homogeneous grain microstructure. (c) Low and (d) high-magnification images of the Si_3N_4-GNP 1.0 Vol% nanocomposites[34].

Jian Liu et al. also reported the same anchoring toughening effective when adding GNPs to Al_2O_3[69], and they obtained a 31% increase in flexural strength and a 27% increase in fracture toughness for the Al_2O_3 CMCs. In their research, they observed the securely anchored GNPs around the Al_2O_3 grains forming a large area of interface. They claimed that such high contact areas between the GNP and ceramic matrix increased the interfacial friction; accordingly, they believed that the energy required for pulling-out the GNPs from the matrix would be greater than pulling-out CNTs from the matrix. In their earlier work from the same group[35], Liu et al. incorporated GNPs to ZrO_2-Al_2O_3 by powder processing, followed by SPS densification, and the resulting ZrO_2-GNP exhibited a 40% improvement in the fracture toughness at only 0.81 vol% GNP addition to the composite. This provides further evidence that the crack propagation was restricted by the role of GNP bridging.

2.5 CNT and GNP dispersion in ceramic matrices

CNTs trend to agglomerate into parallel ropes or bundles due to the Van der Waals forces, as a consequence of their high surface areas and high aspect ratios, which is strongly undesirable for making composites. Therefore, to achieve a uniform and homogeneous CNT distribution, ideally individual CNTs are well-separated from each other and uniformly dispersed throughout the ceramic matrix, is a major technical challenge for material scientists. Different approaches have been attempted to deal with the CNT dispersion issue. Initial studies adopted the conventional powder processing, which involved the use of ultrasounds or ball milling to apply shear forces to de-agglomerate the CNTs[25,70]. Then the colloidal processing was reported[71], in which dispersants, surfactants or acid treatment were utilized to modify the CNT surfaces for increased stability of the suspension and enhanced interaction with the ceramic powders. Other techniques include the sol–gel processing[72], which entraps the pre-dispersed CNTs within the gel network.

Indeed, the mixing is the most challenging step in preparing graphene-CMCs. First, we need to avoid any damages to the flakes, and we also need to eliminate re-stacking/agglomerations of the GNPs, both of which will have strong influences on the mechanical and physical properties of the final composites. Although similar to CNTs, the GNP dispersion seems to be easier than that of CNTs. The difficulties associated with CNT dispersion, such as the high aspect ratios and Van der Waals interactions that cause CNT bundling, are not as severe as in CNTs in the case of GNPs. In fact, the characters of high specific areas and the 2D geometry of GNPs allowed them to possess better disperseability in ceramic matrices[73]. Due to the intrinsic nature in the all carbon family, the mixing procedures for CNT-reinforced ceramics have normally been used as a reference to assess the process for GNP-CMCs.

2.5.1 Conventional powder processing

CNT-reinforced ceramic composites:

Conventional powder processing method is the most commonly applied technique to disperse second phase particles in ceramics, and has been first reported to disperse CNTs throughout different ceramic matrices, including

Al_2O_3[25,74], ZrO_2[75], Si_3N_4[76,77], SiO_2[78] and borosilicate glass[79]. In this technique, the filler material is first de-agglomerated using various methods including ultrasonication, and then mixed with the ceramic powder in a solvent. A conventional ball milling or high energy ball milling is then used to produce slurries of well-dispersed powder mixtures. During the ball milling, CNTs could be shortened or damaged, which might lead to a less effective reinforcement with undesirable effects on physical properties of the composites. Finally the blend needs to be dried, crushed and sieved, if necessary, before the densification stage.

GNP reinforced ceramic composites:

In the case of GNPs, different solvents such as isopropyl alcohol[33,80], NMP[81], and DMF[82-84] were used as the dispersing media. Planetary or attritor ball milling machines were all used, with significantly different milling time ranging from 3–30 h. Obviously, this is a time and energy consuming process. Similarly, various ceramic matrices such as Al_2O_3[36,85], Si_3N_4[30] and ZrO_2 have been studies[35], and the results are successful. For example Liu et al used DMF to disperse GNP purchased from Graphene Industries Ltd. Al_2O_3 (50 g) powder was added and then the mixture was further sonicated for 10min.This was followed by a ball milling procedure at 100rpmin in planetary ball mill (PM 100,Retsch,UK) for 4h. GNPs were well dispersed in the matrix and the flexural strength and fracture toughness of the GNP-reinforced Al_2O_3 ceramic composites improved by 30% and 27% respectively over monolithic Al_2O_3[69]. However, one problem associated with these solvents is their high boiling points, which require high temperature to remove them during processing. Recently, other low boiling solvents such as chloroform, acetone and isopropanol were also demonstrated[86]. In addition to solvent removal difficulties, ball milling is both energy and time consuming process and might cause damage to GNPs. Therefore, other mixing strategies also have been developed for GNP dispersion in the ceramic matrix.

In-situ synthesis of graphene-ceramic composites:

Some recent studies have shown that the in-situ synthesis of GNPs in ceramic powder using high energy milling is an effective way, and the quality of the as-prepared GNPs is better than the commercial ones. For example, Fan et al reported the synthesis of graphene within a ceramic powder by planetary milling for long durations[36]. They first heated commercially available expandable graphite to 1000°C for 60 s under N_2, and the sudden heating allowed the graphite to expand along its planes which made the later exfoliation easier during the planetary milling. Further extensive ball milling for 30 h in N-methyl-pyrrolidone (NMP) dispersing media, the expanded graphite powder would form GNPs with mixed Al_2O_3 powder. Tapaszto et al extended this method to the Si_3N_4 matrix[30], using a high efficiency union process type attritor mill, instead of the planetary mill, and produced GNPs with lateral dimensions of a few microns and thickness of a few nanometres (1–30 layers). Compared with commercial GNPs, the in-situ composites exhibited better mechanical properties (bending strength, elastic modulus), as reported by Kun et al[87]. In their study, they used an high efficiency attritor milling operated at 600 rpm for 30 min, to mix the Si_3N_4 powder with the GNPs using ethanol as the dispersing media. Ting et al reported the successful production of 3–4 nm thick GNPs after 30 h of milling[73]. Fig. 2.9b shows a TEM image of the Al_2O_3-GNP powder mixture milled for 30 h. It is obvious that long time ball milling leads to the crumpling and rolling of GNPs, which could also damage of GNP integrity.

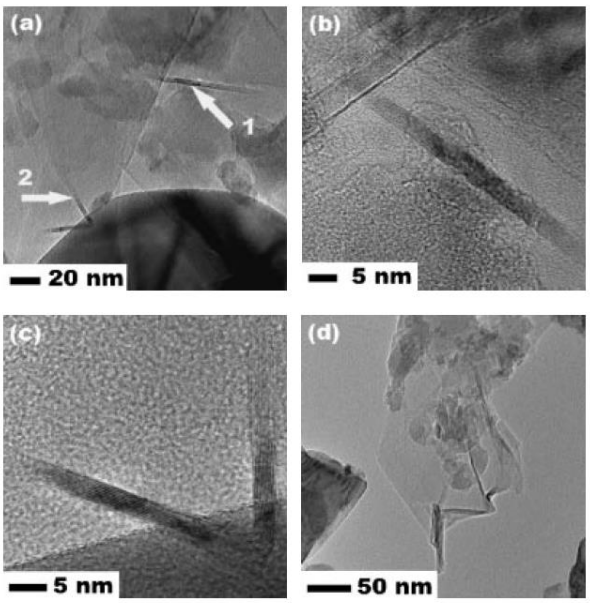

Fig. 2.9 (a) HRTEM images of the Al_2O_3-5 vol%C powder mixture milled for 30 h. (b) and (c) GNPs of 3–4 nm in thickness, corresponding to marks 1 and 2 in (a), respectively. (d) Scrolls produced by ball milling[73].

2.5.2 Colloidal processing

CNT-reinforced ceramic composites:

Colloidal processing is a technique for producing ceramic suspensions on the basis of colloidal chemistry. The basic strategy is to coat CNTs with ceramic particles by adjusting surface chemistry, stabilizing suspensions as well as reducing repulsion between CNTs which prevent agglomeration and facilitate the homogeneous dispersion in the matrix. The most commonly used coating method is the heterocoagulation of nanoparticles which occurs when two stabilised suspensions are mixed. Opposite charge between CNTs and ceramic matrix particles is the driving force that promotes the coating process in the final suspension. To apply opposite charges, surface modification of both the CNTs and the matrix is required, by using surfactants which generate same/opposite electric charges. Attempted anionic surfactants for CNTs are mainly sodium dodecyl sulphate (SDS)[88], whilst typical cationic surfactants are polyethylene glycol (PEG) and polyethylene amine (PEI)[89]. SDS and SDBS can decrease the aggregative tendency of CNTs in water[90]. The heterocoagulation approach achieved some success in producing well-dispersed CNT-ceramic composites[55]. Fan et al used SDS to apply electronegative charge onto the CNT surfaces, and PEG to produce the positively charged Al_2O_3 particles[55]. Wei et al reported similar

approach for the Al_2O_3-SWCNT system, and obtained the fracture toughness of 6.40±0.3 MPa.m$^{1/2}$[56]. Other systems have also been investigated using this heterocoagulation process, such as Al_2O_3[20,91], ZrO_2[92] and Si_3N_4[93].

GNP-reinforced ceramic composites:

Unsurprisingly, same heterocoagulation technique has been tested in the fabrication of GNP-ceramic composites. Depending on the exfoliation procedure, GNPs can be dispersed with the aid of a range of surfactants. For example, obtained via liquid phase exfoliation of graphite in water, GNPs can be dispersed using the following surfactants: SDS, SDBS, LDS, cetyltrimethyl ammoniumbromide (CTAB)[94]. This water-based process avoided the use of high boiling point, toxic solvents, which is advantageous. During the process, it is believed that the dissociation of the head group ions will result in the formation of an electrical double-layer on GNP surface, and the resultant Coulomb repulsion from the double-layer stabilizes the sheets. The repulsion is generally characterized according to the ζ potential, i.e. the electrical potential at the edge of the layer of bound surfactant molecular ions.

Based on this mechanism, Walker et al successfully dispersed GNPs into Si_3N_4 homogenously using CTAB in both the GNP and ceramic suspensions, to develop the electrostatic repulsion, and obtained good dispersion[34]. As a cationic surfactant, CTAB produced positive charges on both the ceramic and graphene surfaces. For good dispersion effect, the concentration of surfactant needs to reach a critical micelle concentration, and they found out 1 wt% of CTAB is adequate. Fig. 2.10 shows the exfoliated GNPs mixed with Si_3N_4 particles they have produced by colloidal processing, which displays the well-dispersed Si_3N_4 particles on the GNP surfaces[34].

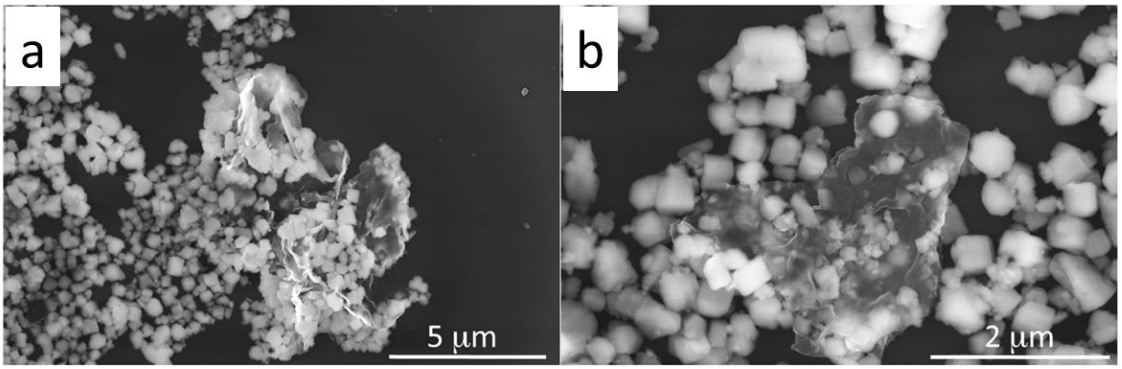

Fig. 2.10 (a) Low- and (b) high-resolution SEM images after colloidal processing, exhibiting the partially exfoliated GNP mixed with well-dispersed Si_3N_4 particles[34].

Using electrostatic attractions between GO and ceramic particles to obtain homogenous dispersions is another effective strategy to produce GNP-ceramic composites. For example, Wang et al have functionalized graphite to GO first, then obtained well-dispersed GO in Al_2O_3 powders[95]. Followed by subsequent GO reduction, they obtained Al_2O_3-GNP composites, which exhibited a 53% and 13 orders of magnitude improvement in the fracture toughness and electric conductivity, against their monolithic Al_2O_3 counterpart.

2.5.3 Sol-Gel

Sol-gel processing is another route for producing CNT-ceramic composites. The key of this method is to create a precursor that can undergo a condensation to produce a green body which contains well-dispersed reinforcing fillers. The first step involves the production of a sol that containing the ceramic particles, and then the CNTs are mixed and entrapped in the sol, to form a gel network. The final step is the calcination of the dried gel, to obtain a dense composite. For this reason, this technique can mainly be used for sol-gel forming systems, such as glass ceramic matrices SiO_2[96,97], and alumino-borosilicate[98,99]. However, for the few polycrystalline ceramics, the sol-gel process has been shown effective to some extent. CNTs agglomerates still exist, although appear to be smaller than that observed in conventional powder processing[72]. The advantages of using sol–gel processing are that it can be used to obtain transparent and mechanically stable films and bulk materials[100]. Watcharotone et al used this technique to prepare SiO_2-GNP composite films as transparent conductors[101], and for SiO_2 coated GO composites for electrochemical sensing of dopamine[102], and even

GNP aerogels as highly efficient counter electrode materials for dye sensitized solar cells[103].

2.6 CNT and GNP-ceramic Densification techniques:

Achieving near full density, without damaging the CNT structure and morphology, is a fundamental requirement and another important challenge in ceramic matrix nanocomposite, as most of the mechanical properties are strongly affected by the density. CNTs existing at the grain boundaries hinder the ceramic grains coalescence, which tends to lead to poorly densified microstructures[104]. For this reason, pressure-assisted solidification processes are generally used to counter this problem.

The increasingly popular technique to fabricate CNT-reinforced ceramic composites is spark plasma sintering (SPS), due to the fact that SPS allows sintering fully dense composites at lower temperatures and shorter holding times which can avoid CNT degradation[70,84,105,106]. In SPS, an electrical current flows through the graphite punches and die which generates very high heating rate to the powder sample (few hundred °C/min) by the Joule effect. Pressure as high as 1 GPa can also be applied to the samples, in order to sinter them quickly (3–10 min) and at relatively low temperatures (Fig. 2.11a). A statistics has shown that about 76% ceramic nanocomposites were consolidated by pressure-assisted sintering,, of which SPS and hot-pressing (HP) have a share of 50% and 26%, respectively[107].

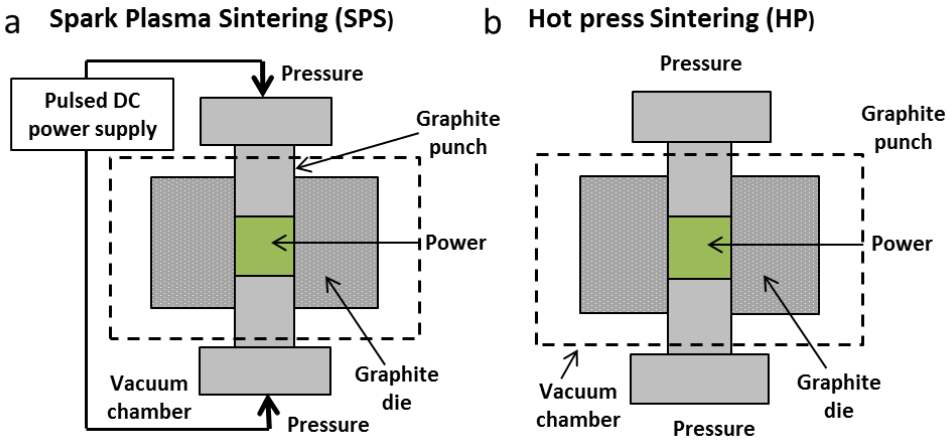

Fig. 2.11 Schematic representation of (a) SPS process, and (b) HP process.

Hot-pressing provides simultaneous high pressures and high temperatures to powder systems, which in turn gives high densities, thus good mechanical properties to either pure ceramics and their composites. As shown in Fig. 2.11, the primary difference between SPS and HP lies in how the thermal energy is transferred to the powder pellet. In an SPS, it is via the Joule effect; whilst in an HP, the graphite heating elements surrounding the pressing tool provide the heat via radiation/convection. Therefore, the heating rate in HP is limited to up to 20°C/min. A few studies used both methods for the same composites, to compare their negative and possitive points[82]. The fast heating rate in SPS saves time, and importantly energy[108], however it may yield low density and inhomogeneous microstructures, sometimes resulting in large grain sizes[109,110].

Pressureless sintering (PLS) offers a convenient and cheaper consolidation alternation, but wide variations in earlier results have made this technique un-attractive and debatable. In PLS, the green body samples are placed in an Al_2O_3 boat and then moved to the centre of an Al_2O_3 working tube inside a tube furnace. After heating, the furnace is allowed to cool down naturally to room temperature (Fig. 2.12)[111]. Using this technique, Zhan et al and Ahmad et al claimed widely different densities for similar samples, as high as 99% and as low as <90% for 1 wt% CNT-reinforced Al_2O_3, respectively[111,112]. In recent reports, Sarkar et al densified Al_2O_3 containing 0.3 vol% of CNTs to >99% at 1700°C using PLS; and Michalek et al and Ghobadi et al. obtained 99.9% and >98% densities for Al_2O_3 reinforced with 0.1 wt% and 1 vol% CNTs, respectively[113-115].

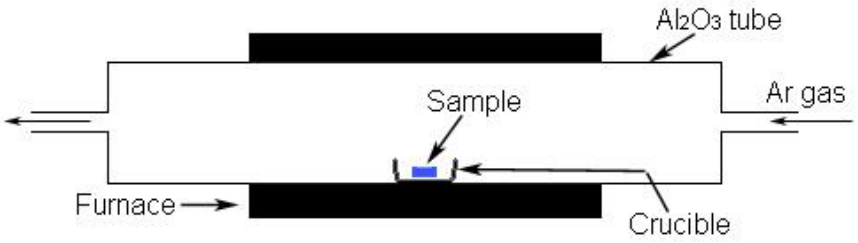

Fig. 2.12 Schematic representation of pressureless sintering process.

For other ceramic systems, Tatami et al recorded a drop in relative densities from 100% to 90% for 0 to 5 wt% CNT additions for Si_3N_4-CNT composites at 1700 °C under N_2 atmosphere[116], against much higher densities >96% for 5 wt% CNT additions by using HP. Therefore it seems that using very low volume fraction is quite important for this technique.

Microwave sintering is another inspiring and "green" sintering technique, with the advantage of lower densification temperatures and shortened processing time. This technique has been successfully used to consolidate most mainstream industrial ceramics (e.g., Al_2O_3, ZrO_2, Si_3N_4), both pure and composite forms, and resulted in high densities[117]. Despite the mixed large and fine grained microstructure of the final ceramic consolidated by microwave sintering that made it bit divisive, this technique exhibits great potentials for densifying CNT-reinforced ceramics. The advantageous features such as short sintering time and low densification temperatures are not deleterious for CNT structures; furthermore the localize heating at the grain boundaries may be helpful in constructing strong interfaces between CNTs and the matrices; and finally, the grain coarsening seems not a big issue in microwave sintered CNT-reinforced ceramics, possibly owing to the grain refining tendency of CNTs. Table 2.1 summarises the key features of HP, PLS and SPS.

Table 2.1 key features of HP, PLS and SPS

References	Matrix	CNT types	Purification methods	Dispersion procedures	Sintering techniques
[118]	Si_3N_4	SW	P	UT of CNTs with surfactant (C16TAB) and Si_3N_4	SPS under vacuum
[20]	Al_2O_3	MW	Oxidation at 500 °C for 90 min	UT of CNTs in ethanol	SPS at 1500 °C for 10 min under 50 MPa
[57]	Al_2O_3	MW	AT (H_2SO_4 + HNO_3)	UT of CNTs into water and SDS then incubation for 2 weeks	HP at 1600 °C, 60 min, 40 MPa
[119]	Mulite	MW	P	CNTs dispersion into ethanol by MS and UT	HP at 1600 °C for 60 min under Ar atmosphere at 30 MPa
[120]	Si_3N_4	MW	P	24 h ball milling the CNTs and Si_3N_4 slurry	HP at 1750 °C for 60 m under 30 MPa
[121]	ZrB_2-SiC	MW	P	20 min UT of CNTs and matrix with subsequent 24 h ball milling	HP at 1900 °C for 60 min under 30 MPa
[122]	$BaTiO_3$	MW	P	-	HP, 1200 °C, 60 min
References	**Matrix**	**CNT types**	**Purification methods**	**Dispersion procedures**	**Sintering techniques**
[123]	Al_2O_3	MW	-	DG (CVD at 750 °C for 15 min for direct CNTs growth on Al_2O_3 nano-particles)	SPS at 1150 °C for 10 min under 100 MPa
[124]	Al_2O_3	SW	Pristine	UT of CNTs in ethanol	SPS at 1520 °C under 80 MPa
[125]	Al_2O_3	MW	P	35 h UT in water	SPS at 1300 °C, 20 min, 90 MPa
[126]	Al_2O_3	MW	AT (H_2SO_4 + HNO_3 in 3:1 for 7 h)	surfactant (SDS) using combination of UT and 24 h BM	HP at 1550 °C for 1 h under 30 MPa using Ar gas
[127]	Al_2O_3+ZrO	MW	AT (heating in 65% HNO_3 at 80 °C for 8 h)	2 min UT of CNTs with surfactant (SDS)and 24 BM then freezing with Nitrogen	HP at 1500 °C for 2 h under 30 MPa in Ar atmosphere
[128]	Al_2O_3	SW	AT (H_2SO_4 + HNO_3)	UT for 24 h	SPS at 1300 °C for 5 min under 75 MPa
[129]	Al_2O_3	MW	AT	UT of CNTs and Al_2O_3 in water followed by 2 h and BM of CNTs/Al_2O_3	PLS at 1600 °C, 15 min, Ar

[114]	Al_2O_3	MW	AT (heating in 65% HNO_3at 80 °C for8 h)	BM and Surfactant (Darvan C–N)	PLS at 1500 °C for 2 h using Ar
[130]	Al_2O_3	MW	AT (H_2SO_4 + HNO_3) for 3 h	24 h BM of ball Al_2O_3 powder and 30 min UT of CNTs in water and then BM of CNTs/Al_2O_3 mixture	PLS at 1500–1600 °C,120–240 min, Ar

Unsurprisingly, SPS processes have been widely used for graphene-ceramic composites, due to the great success on other carbon nano fillers[31,32,34-36,69,80,95], except that a few studies have found that HP produced improved properties[82,131-133]. For example, in Rutkowski et al report[131], they used HP to produce Si_3N_4-GNP nanocomposites and reported an improvement in thermal properties. After comparing the structural stability of graphene in Al_2O_3 sintered by HP and SPS, Inam et al[82] have found that the HPed samples possess higher crystallinity, thermal stability and electrical conductivity than those of the identically SPSed composites. They have attributed these improvements to the thermally induced graphitisation caused by the longer sintering durations; therefore a shorter sintering does not necessarily produce high quality graphene.

2.7 Microstructural and interface studies for CNT-reinforced ceramics

Sharp reduction from coarser grains in monolithic ceramics (Fig. 2.13a) to finer grains in CNT-reinforced ceramics (Fig. 2.13b) is a major structural change. This is believed to arise from the pinning of matrix grains by the CNT which restricted the grain growth during sintering[57]. Fracture mode alteration from inter-granular in monolithic ceramics (Fig. 2.13a) to trans-granular in the CNT-reinforced ceramics (Fig. 2.13c) is another interesting feature of change. To fully appraise these morphological features is very important for analysing interface, strengthen mechanisms and even other properties. Behind such changes. In the case of monolithic Al_2O_3, it shows clearly the edge and corner fractural features (Fig. 2.13a), representing the typical inter-granular fracture mode; and conversely a blurry and glaze-like surface appears for CNTs-reinforced Al_2O_3 (Fig. 2.13c), indicating the trans-granular mode of fracture[57]. These observations mean that CNTs, as the second phase, must be responsible for altering the fracture modes. Indeed, when CNTs were homogenously dispersed within the ceramic matrix,

they arranged themselves at various locations such as along grain boundaries (Fig 2.13f), across grains boundaries (Fig 2.13g), inside single grains (Fig. 2.13h), contributing to strengthening the composites at nanometre level by making bridges across grains and sharing the grains, as discussed in prior studies [57,134]. Presumably, all these interesting arrangements of CNTs in ceramic matrices promoted the trans-granular fracture, rather than inter-granular fracture as did in the pure ceramic. In very recent report, Ahmad et al obtained 5-fold finer grain size in Al_2O_3-MWCNTs nanocomposites by 300 ppm Y_2O_3 doping than its un-doped Al_2O_3 counterpart, and mixed inter/intra fracture mode in Y_2O_3 doped nanocomposites was observed[135]. However this fracture mode change phenomenon is another grey area that is not fully understood for CNTs-reinforced ceramics, which offers opportunities for prospective thinking and further research work.

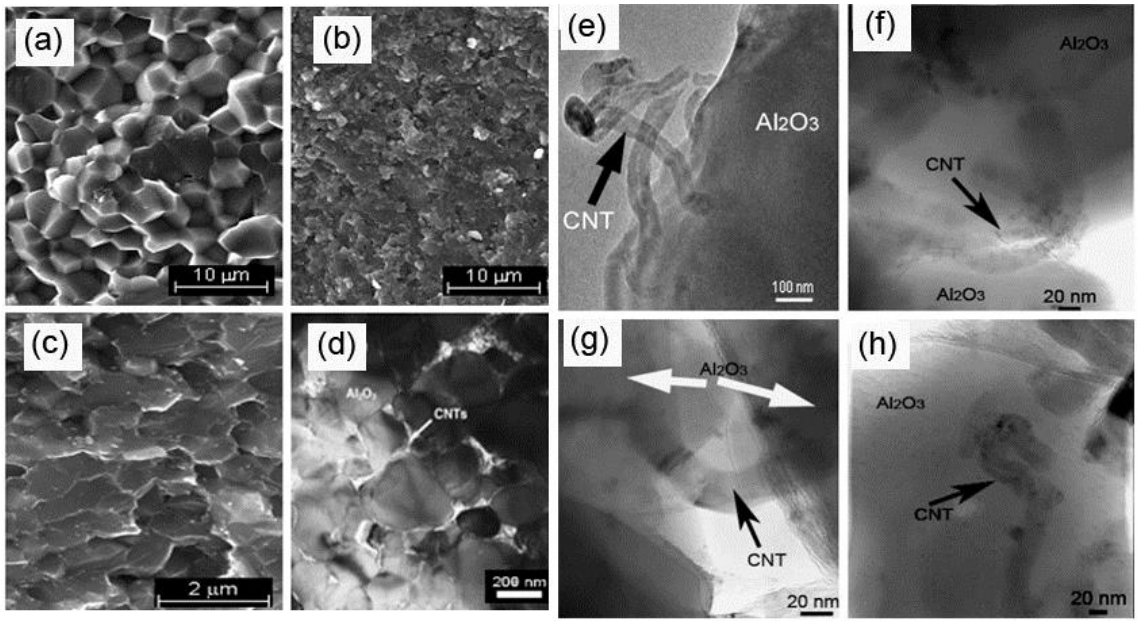

Fig. 2.13 Structural features of (a) monolithic Al_2O_3 showing large grains with inter-granular fracture; (b) Al_2O_3-CNTs nanocomposites with fine grains; (c) Trans-granular fracture mode in Al_2O_3-CNTs nanocomposites; and (d) single-walled (SW)CNTs at grain boundary of Al_2O_3 matrix. TEM images exhibiting the CNT–ceramic interactions (e) multi-walled (MW) CNTs (black arrow) showing their morphology in nanocomposite; (f) a single MWCNT existing at grain boundary; (g) in porosity and (h) embedded within a single ceramic grain.

Recent developments in the electron microscope technology and technologies associated with them for sample preparation are changing the research approaches significantly. They allow us to examine sample interfaces at very fine

details, to unveil much deeper information, and it reflects the recent research attentions focusing on tailoring the interface structures at atomic level. This approach could allow for the construction of 'defect-free' interface to offer maximum properties or optimal functionalities. For example, FIB-SEM (focused ion beam scanning electron microscopy) has made the preparation process for TEM (transmission electron microscope) sample of hard ceramic composites much easier and samples can be prepared in hours. In particular, due to the interesting reaction of Al_2O_3 with alkaline, Al_2O_3-CNT nanocomposites can be sieved after sintering and etched using NaOH aqueous solution. The remained CNTs with a thin layer of Al_2O_3 residue can be used for interface study under TEM. For CNT-reinforced ceramics, the interface is a complex transitional region layer between the CNT and matrix, which controls the CNT de-bonding, pull-out and crack-bridging at micron and nanometre level. Thus, controlling the interface chemistry and tailoring smart microstructures are essential for producing exceptionally tough and strong nanocomposites.

Dedicated efforts to explore the CNTs-ceramic transition region have been reported, and each addressed in interesting way[20]. Yamamoto et al first proposed that acid treatment did not significantly damage the overall structures of CNTs[20], however localized etches of the cylindrical body at different locations created nanoscale defects (nano-pits) along the tube axis, as shown in Figure 3b. These nano-pits having depths of ~15 nm are anchored by the matrix grains (Fig. 2.14c), forming locks and resistance in CNTs' sliding over the matrix, thus leading to good connection of composite constituents at the interface[20]. Further, a close cross-sectional examination of the MWCNT shown in Fig. 2.14 of the high resolution TEM image reveals its uneven surface, hollow core and graphitic layers. These layers are not concentrically on a long distance and many compartments exist, which is a typical feature of MWCNTs synthesized by CVD. Ahmad et al postulated that high surface roughness of the CNTs could resulted in two potential advantages[136], (1) the chemically highly reactive, and (2) physically difficult to slide out of the matrix, compared with a smooth surface. The former could help to improve the interfacial bonding with the matrix and the latter could pose much larger friction forces to stop the CNT pull-out[136].

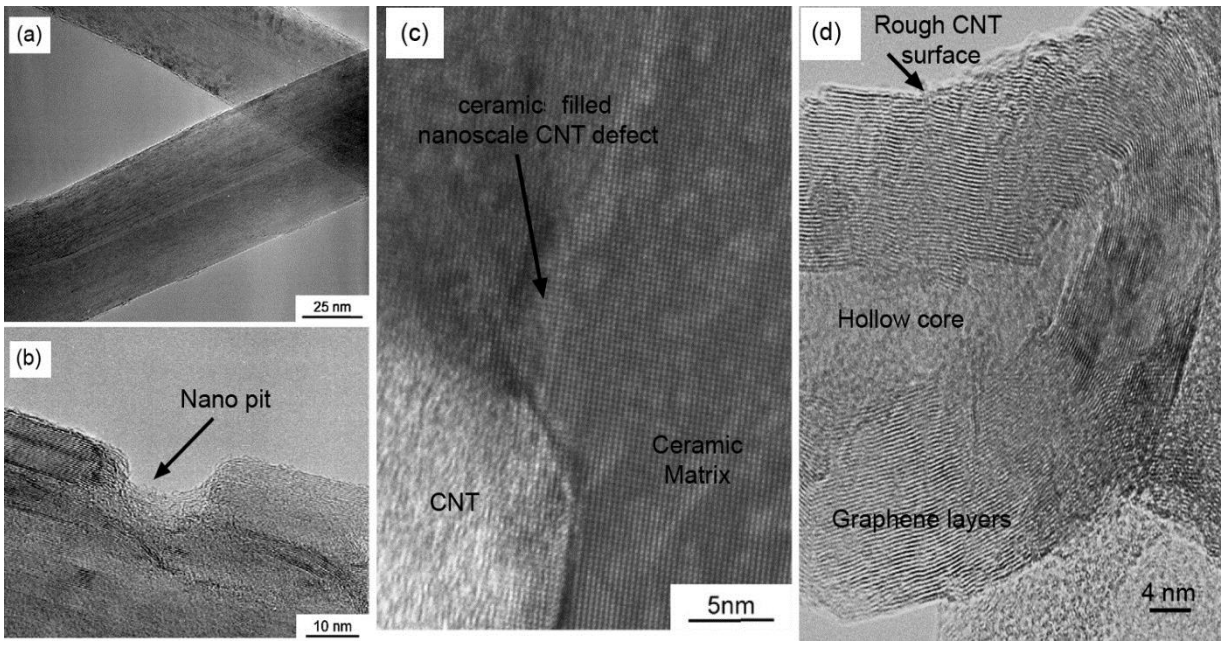

Fig. 2.14 (a) TEM image of the pristine CNTs; (b) High-magnification TEM image of the acid-treated CNT surface. Arrow indicates the nano-pit; (c) Nano-pit on the acid-treated CNTs is filled up with Al_2O_3 crystal; and (d) Rough surface of CNT produced by chemical vapour deposition (CVD) method.

The CNT's surface unevenness and its anchoring with the ceramics matrix are a good physical explanation of enhanced frictional forces at the interface. However, the chemical interactions of CNTs with the ceramics remained unattended for several years. Estili et al. studied the interfacial areas of Al_2O_3-CNT nanocomposites using high resolution-TEM[137], but they were unable to identify any interfacial phases or intermediate compounds at the Al_2O_3-CNT interface. A recent attempt addressed this topic and explained the chemical activity taken place at the Al_2O_3-CNT interface during HP process[136]. They reported the formation of an extremely thin (1–2 nm) intermediate phase of Al_2OC, which is possibly produced due to the carbothermal reduction of Al_2O_3 by CNTs. Fig. 2.15a–b shows a clear evidence of a CNT sticking with Al_2O_3 at the interface.

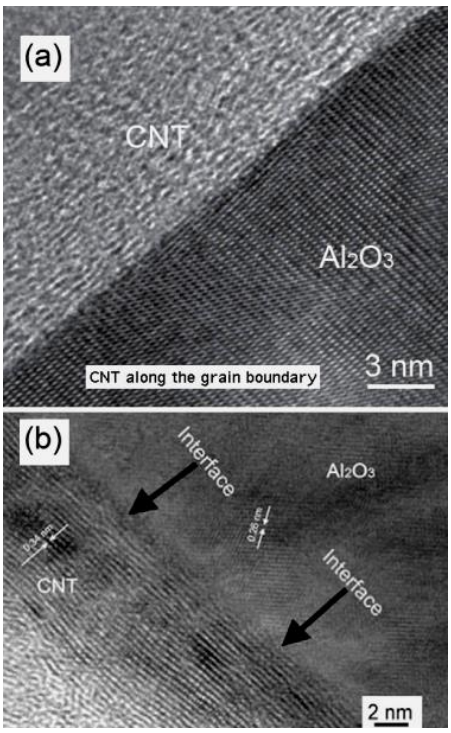

Fig. 2.15 (a,b) High-resolution TEM images showing CNT/ceramic interfaces[57,112].

The multi-layered structure of CNTs allows such chemical and physical reactions to accommodate the formation of nano-pits, with only a few outer layers being involved for Al_2OC or Al_4C_3 formation. This may not be true for SWCNTs which contain only a single graphene layer while forming the tubular structure, even though plenty of studies have claimed tremendous property improvements in ceramics composites[22,138]. This raises one big question, as to being only one layer how it reacts with the matrix to form a good interface, following the toughening mechanisms proposed above. Therefore, this mystery remains unresolved. The understanding of the nanostructure characteristics and the interfacial relationship between SWCNTs and the ceramic matrices is far from satisfactory, which opens new windows of potential research in this advanced area of nanotechnology[57,60,123,139].

2.8 Microstructural and interface studies for GNPs-reinforced ceramics

The microstructure of the GNP-reinforced composite is strongly affected by the dispersion behaviour of GNPs in the ceramic matrix, because the number of GNP layers affects the grain growth behaviour and fracture mode of the ceramic matrix. Using mechanically exfoliated GNPs from 3 to 15 vol.% in Al_2O_3 matrix[36], Fan et al compared the fracture surface of pure Al_2O_3 with the composite containing 1

vol.% GNPs, and they concluded grain size reduction in the composites. This homogeneous grain sizes conjugating with increasing the trans-granular fractures in Al_2O_3-GNP composite (Fig 2.16b) are due to success in their strategy in preparing and dispersing of GNPs which include the proper choice of planetary ball milling and NMP as solvent which has good surface chemistry with graphene.

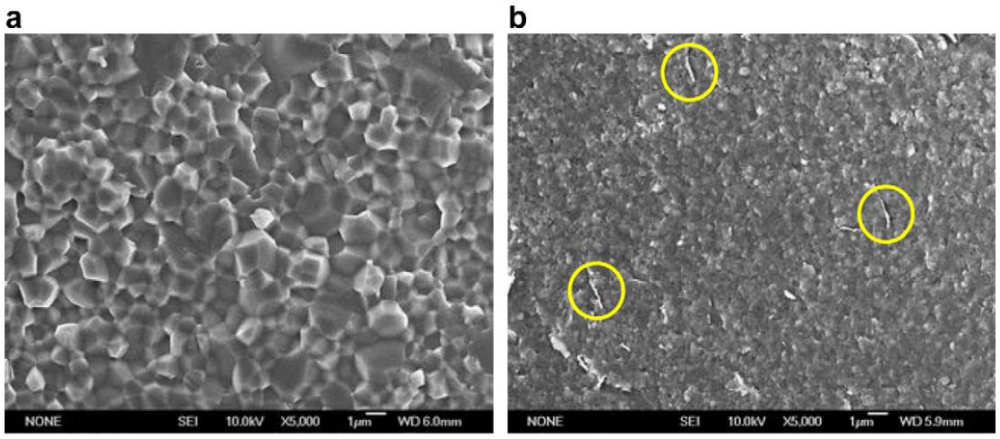

Fig. 2.16 SEM images of fractured surfaces of (a) a pure Al_2O_3 ceramic, (b) a Al_2O_3-GNP composite containing 1 vol.% GNPs[36].

Using TEM showed that more than half of the GNPs in Fan et al composites are below 10 nm in thickness and some of the GNPs are as thin as 2.5 nm, as shown in Fig. 2.17a[36]. They also revealed the nanosheets semi-wrapped around the matrix grains forms a network structure Fig. (2.17b). However, such a network was not created in composites prepared by Duza et al[64]. They presented Si_3N_4-GNP composite with a significantly higher fraction of overlapped GNPs in comparison to Fan et al (Fig. 2.17c) and the observed GNPs are usually with thicknesses higher than 20 nm. Such difference indicating the effectiveness of Fan et al strategy in preparing and dispersing of GNPs.

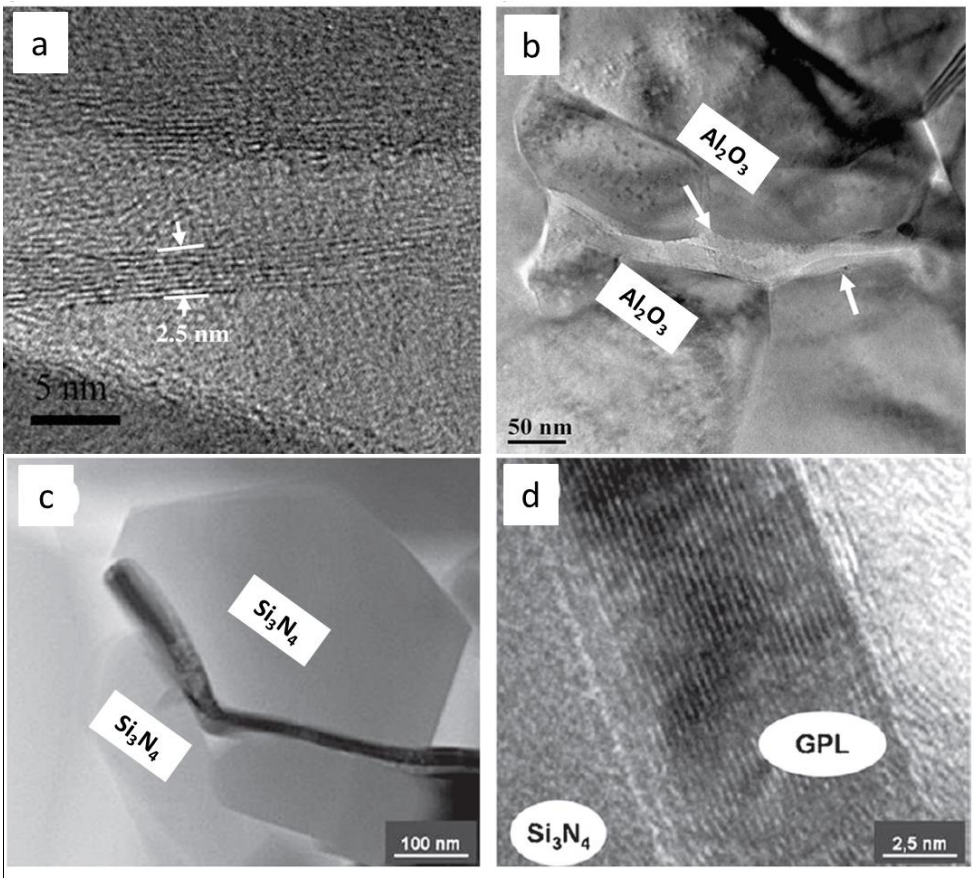

Fig. 2.17 (a) Al_2O_3-GNP composite containing 5 vol.% GNPs with a thickness of 2.5 nm, (b) overlaped GNPs between Al_2O_3 nano-particles with the thickness of 10nm, (C) GNP at the grain boundary of Si_3N_4/Si_3N_4 with the thickness of 25 nm characteristic for all composites and (d) platelet with the thickness of 10 nm [36,64].

2.9 Mechanical and other functional properties for CNT-reinforced ceramic composites

In view of the vast applications of the economically viable Al_2O_3 ceramics in industry, lots of studies have been done to improve their fracture toughness by CNT additions. For example, Table 2 shows that the higher fracture toughness values of CNTs-reinforced Al_2O_3 were obtained at lower CNT additions (< 2 wt%), and declining trend can be seen at higher CNT levels in all cases, except from the values reported by Zhan et al[112]. Furthermore, the composite fracture toughness reported by Zhan et al. was the highest in Table 2. However, this value may be due to various factors: (1) the use of SPS techniques (positive); (2) reinforcement phase being SWCNTs (positive); and (3) the assessment of the fracture toughness by an unreliable direct crack method, DCM, (negative). Yamamoto et al[20] used the SPS to sinter similar composite reinforced with CNTs,

and used the single-edged notched beam (SENB) method to assess the fractures toughness, however the results were not as good as the results reported by Zhan et al[112] and Ahmad et al[135]. In case of the high values reported by Ahmad et al[57], it is probably due to the better dispersion of CNTs within the matrix, as they adopted a unique method. Further, Huang et al[122] showed tremendous improvements in fracture toughness (57%, 114% and 328%) values for $BaTiO_3$ ceramic after reinforced with (0.5, 1 and 3 wt%) CNTs; whereas a 15% improvement was recorded by Tian et al for 2 wt% CNT-reinforced ZrB_2-SiC ceramics[121]. However, these inconsistent results (Table 2.2) put a question mark on these triumphs, and core issues in such discrepancies could be depending on the CNT dispersion methods, choice of sintering process and techniques adopted for characterisation.

Table 2.2 Properties of CNTs-reinforced ceramics.

References	Matrix	CNT contents	Relative density (%)	Hardness (GPa)	Flexural strength (MPa)	Fracture toughness (MPa. $m^{1/2}$)
118	Si_3N_4	0	99.2	15.7	1046	4.8
		1 wt%MWCNTs	98.7	15.0	996	6.6
20	Al_2O_3	0	95.6	17.3	500	4.4
		0.5 wt% MWCNTs	99.2	16.8	685	5.9
		1 wt% MWCNTs	98.9	15.9	650	5.7
112	Al_2O_3	0	-	-	-	3.3
		3 wt% SWCNTs	-	-	-	7.9
57	Al_2O_3	0	99.8	16	356	3.5
		2 wt% MWCNTs	99.5	18	402	6.8
		5 wt% MWCNTs	99.1	-	423	5.7
113	Al_2O_3	0	99.5	17.5	222	3.92
		0.15 vol% MWCNTs	98.4	21.4	242	5.27
114	Al_2O_3	0	-	16.9	-	5.5
		1 vol% MWCNTs	-	13.5	-	6.0
119	Mulite	0	-	-	466	2.0
	($3Al_2O_3 + 2SiO_2$)	2 wt% MWCNTs	-	-	512	3.3
140	SiC	0	939	-	303	3.3
		10 wt% MWCNTs	94.7	-	321	3.8
121	ZrB_2-SiC	0	-	15.8	582	4
		2 wt% MWCNTs	-	15.5	616	4.6
122	$BaTiO_3$	0	98.5	-	-	0.7
		98.50	98.5			0.7
		0.5 wt% MWCNTs	97.3			1.1
		1 wt% MWCNTs	99.2			1.5
		3 wt% MWCNTs	98.6			3.0
141	Al_2O_3	0	-	-	395	4.41
		20 vol% MWCNTs	-	-	403	4.62

[142]	Al_2O_3	0	-	-	-	3
		1 wt% MWCNTs	-	-	-	5
[143]	Al_2O_3	0	-	15.71	-	3.24
		5 wt% MWCNTs	-	0.72	-	4.14
[144]	Al_2O_3	0	-	18.2	-	4.5
		2.5 wt% MWCNTs	-	15.75	-	11.4
[145]	Al2O3	0	99.9	22.9	-	3.54
		10 vol% MWCNTs	97.4	11	-	2.76

Recently, Sarkar et al[113] calculated fracture toughness values of the Al_2O_3–CNT nanocomposites by employing DCM method using Niihara (5.3 MPa. $m^{1/2}$) and Liang models (5.5 MPa. $m^{1/2}$), and reported better fracture toughness values than those obtained using SENB technique (5.1 MPa. $m^{1/2}$); whereas Ahmad et al[57], reported higher fracture toughness values attained from SENB method than those obtained from DCM method using Chantikul model. These conflicting reports suggest that engineering components cannot be validated for structural load-bearing applications using DCM method; however this convenient method is widely employed for fracture toughness comparisons. Similar inconclusive and controversial fracture toughness values regarding CNT-reinforced Si_3N_4 were also reported by Corral et al and Pasupuleti et al[118],*[120]*, both consolidated Si_3N_4 with 1 wt% CNTs and obtained a 30% reduction (by SENB method) and 40% increment (by ISB method) in fracture toughness, respectively.

Other mechanical properties such as hardness and elastic modulus are also intensively investigated. Yamamoto et al reported a drop in hardness and rise in flexural strengths at low CNT additions to Al_2O_3[20], and further reductions in both properties at high CNT additions. This tendency has been confirmed by many others[118,120],, as shown in Table 2[20].

The dual role of CNTs, indirectly enhancing the mechanical properties and directly acting as a lubricant, converts ceramic composites into an attractive wear resistance material, and various reports demonstrated the steady reduction of friction coefficient with CNT additions[136]. High thermal and electrical properties of the CNTs have been predicted and several attempted to incorporate CNTs into insulated ceramics in order convert them into highly electrical and thermally conductive materials[141]. Ceramics exhibited higher electric conductivity (EC) when reinforced with SWCNTs (10^6 S/m) than with CNTs (10^3–10^5 S/m)[123,134].

Sarkar et al reported that the EC of CNT-reinforced composites was dependent on the formation of electrically conductive networks, and on the grain sizes of the final nanocomposites[146]. Homogenous dispersion help the network formation, whereas large grain size with less grain boundaries eliminate resistance, thus both contribute to the better results. To date the highest EC values of 4816 S/m reported by Estili for Al_2O_3-20 vol% CNTs is 43% higher than that reported by Zhan et al[134,141]. Further studies of the effects of surface functionalization of SWCNTs on the EC by Zanman et al have shown that the hydroxyl group functionalized SWCNT offered ~10 times higher EC in 1 wt% SWCNT-reinforced Al_2O_3 nanocomposites than those functionalized by carboxylic acid group[147]. Moreover, Bi et al reported a drop in the electrical percolation by increasing the aspect ratios of MWCNTs[148].

Although the thermal conductivity (TC) of SWCNTs and CNTs ranges from 3000–6000 W/m·K[149], their ceramic nanocomposites with barely demonstrated any good thermal performance. Compared with the unreinforced Al_2O_3, Zhan et al reported lower (7.3 W/m·K) TC in nanocomposites reinforced with 15 vol% SWCNTs than their monolithic counterpart (27.3 W/m·K)[134]. But other reports reported higher TC values (63.52 and 6 W/m·K) in nanocomposites with (8 and 4 wt%) CNTs than those of pure Al_2O_3 (19.96 and 5.37 W/m·K) samples[123],[150], respectively. This area of research is inconclusive, and needs further investigations.

2.10 Mechanical and other functional properties for GNP-reinforced ceramic composites

Although several authors have reported an improvement in the mechanical properties of advanced structural ceramic through the incorporation of GNP in the matrix, the special attention in terms of mechanical properties is to the fracture toughness due to brightness problem is ceramics. However, the fracture toughness of GNP-reinforced ceramics needs more studies since the mechanical strength of the ‘graphene’ filler exhibits remarkable variations depending on the synthesis methods, the source of GNPs and sintering techniques, which affect the mechanical properties of GNP-reinforced ceramics.

Authors have mainly used two techniques to measure the fracture toughness: Vickers indentation fracture toughness (VI); and single edge notched beam (SENB). Vickers indentation is the most commonly used technique due to the limited availability of sample and the advantages in terms of ease of use[151]. However, it should be noted that it does not provide absolute values for fracture toughness because it measures the toughness of the material locally in the sample under a complex stress field[70,152]. Whereas the SENB method gives the fracture toughness values for the bulk under mode I crack opening[18]. Therefore it is recommended to use the SENB method if absolute fracture toughness values are required.

For the first time, Walker et al. reported the unexpected anchoring toughening mechanism for SPSed Si_3N_4-GNP nanocomposites[34]. They measured fracture toughness of 6.6 MPa.$m^{0.5}$ for the composite with 1.5 vol% of GNP which was significantly higher than the value measured for the monolithic silicon nitride. Due to their 2D flexible microstructure; GNPs wrapped or anchored around the Si_3N_4 grains and formed a continuous network along the grain boundaries hence cracks were not able to propagate through the graphene walls and were arrested.

Same anchoring mechanism was also reported by Liu et al for GNP reinforced zirconia toughened Al_2O_3 (ZTA) nanocomposites using SPS[69]. The fracture toughness of their material, measured by SENB method, resulted in an increment of 40% for only 0.8 vol. % loading of GNPs. Similar to other graphene ceramic composites they also observed toughening mechanism such as pull-out, bridging and crack deflection on fractured surfaces with GNPs trapped and anchored in between grain boundaries. Such impressive improvements in mechanical properties have been obtained with very small GNP loading in ceramic composites. However, in the case of CNTs, a higher concentration (1-10 vol%) was generally required for toughening and strengthening of ceramics. For example, 2wt% GNP addition to Al_2O_3-GNP composites prepared by Wang et al[95] resulted in 53% improvement in fracture toughness (5.21 MPa. $m^{1/2}$ in composite over 3.40 MPa. $m^{1/2}$ in pure Al_2O_3) and 13 orders of magnitude improvement in conductivity compared to pure Al_2O_3. They also observed that the addition of graphene in the Al_2O_3 matrix resulted in grain size refinement from 1000 nm in pure Al_2O_3.

The quality and dispersion grade of GNPs in Si_3N_4-based nanocomposites have been investigated by Kun et al[87], and Kvetkova et al[133]. Both prepared and characterized Si_3N_4-based nanocomposites with different amounts of carbon reinforcement in the form of multilayer graphene, graphite nanoplatelets and nanographene platelets. Kun et al showed both bending strength and elastic modulus decreased by the addition of multilayer graphene while Kvetkova reported an improvement in fracture toughness for all 1wt% Si_3N_4-GNP composites using multilayer graphene prepared by mechanical milling and commercially available graphene nanoplatelets. There was a 45% improvement in fracture toughness for multilayer graphene composite. They observed various toughening mechanisms, including crack bridging, crack branching and crack deflection. However, the hardness of all the composites was lower than the pure silicon-nitride material except for the multilayer graphene composite.

Recently, Kim et al. synthesized unoxidized Al_2O_3-GNP composites[50]. They used The EG (electrochemically expanded, chemically exfoliated graphene) which has a nature of unoxidized graphene with much smaller defects and functional groups. Only 0.25–0.5 vol%, ultra-thin graphene (platelet thickness of 2–5 nm) was enough to reinforce the composite. The wear resistance of the composites was increased by one order of magnitude even as a result of a tibological effect of graphene along with enhanced fracture toughness (KIC) and flexural strength (sf) of the composites by 75% and 25%, respectively, compared with those of pure Al_2O_3.

Fan et al. prepared fully dense Al_2O_3-GNP composites[36]. The GNPs after ball milling are 2.5–20 nm in thickness and homogeneously dispersed in the ceramic matrix. The percolation threshold of the as-prepared Al_2O_3-GNP composites was around 3 vol.% and the composite behaved as a semimetal in the temperature range from 2 to 300 K.

Ramirez et al. also investigated the influence of GNPs addition on the electrical conductivity of Si_3N_4-GNP composites containing 12 and 15 wt% of GNPs[31]. According to the results, due to their aspect ratio and stiffness, the GNPs become self-oriented, lying on their a–b plane, during the spark plasma sintering process

which determines the final microstructure of the composite as well as its electronic response. As the platelet content increases, improved inter-GNP contacts lead to an outstanding increase in the conductivity of the composites.

2.11 Hybrid GNP and CNT reinforced composites.

In recent years, attempts have been made to combine graphene and CNTs to prepare electrode material for lithium ion batteries[44,153]. CNTs have bridged the defects for electron transfer as well as increased the layer spacing between graphene sheets, so these self-assembled hybrid structures delivered remarkable electrochemical performance compared with the neat CNT electrodes[45]. More interestingly, the unique synergistic effect of 1D CNTs and 2DGNP sheets resulted in the formation of 3D GNP/CNT aerogels, which is useful for energy storage applications, water purifications[46], and oil sorption[154].

Such synergy could be very helpful in composites, as the CNTs could help to prevent the GNP restacking, and much higher interfacial interactions between them and the matrix can be produced. Thus, hybrid filler by combining the advantages of 1-D and 2-D reinforcements may lead to further improved properties in nanocomposites. Indeed, this concept has recently been pioneered in polymer-based composites[37], and they have reported the toughest and strongest man-made polymer nanocomposite ropes. All the hybrid GNT reinforced composites studied to date are polymer-based matrices. Inspired by this idea, to explore the effects of the hybrid reinforcement of GNPs and CNTs, namely GNTs, in a ceramic matrix is a very interesting.

For the dispersion of fillers in polymer matrixes the method is similar to ceramic-based composites (section 2.5). Two main strategies have been applied since now. One is using water-based systems with the aid of surfactants. The role of the surfactant is creation of effective surface charge in the surface of CNTs or GNPs which in turns results in Coulomb repulsion between nearby charged colloidal particles. This approach allows composite production with a relatively homogeneous dispersion of the nanofiller into the polymer matrix and improved functional properties. The most popular light weight surfactants which have strong synergy with GNP and CNT are SDBS and SDS which are very effective to decrease the aggregate tendency in CNTs. The other approach is using

organic solvents such as DMF and NMP. Shin et al. used SDBD to disperse hybrid RGO and CNT into PVA matrix by wet spinning method[37]. The synergetic effect between RGO and CNT formed well-aligned structure resulted in super tough PVA composite fibres (Fig. 2.18)[37].

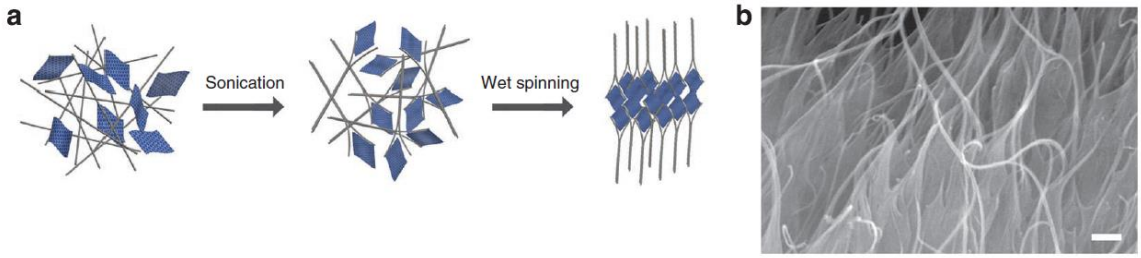

Fig. 2.18 (a) Schematic diagram showing the formation of the oriented interconnected network of RGOFs (curved rectangles) and SWNT bundles (grey lines) as a result of sonication and subsequent wet spinning. (b) SEMimage of the cross-sectional area of a RGOF/SWNT/PVA fibre.

2.11.1 Mechanical, thermal and electrical properties

The combined effect GNP and CNT on mechanical, electrical and thermal properties of various polymers such as epoxy[155], PVA[156], PANI[157], has been investigated and the results showed improvement compared to using single CNT or GNP as filler in polymer-based matrixes. Wang et al. have showed the mechanical properties of epoxy-reinforced GNTs are highly dependent on CNT/GNP ratios[158], and in specific CNT/GNP ratios the flexural strength, tensile strength and flexural modulus can be improved by 26.4%, 33.7% and 24.7% over monolithic epoxy, respectively. They suggest that when CNTs were added to the GNPs, they entangled the GNPs and filled gaps between GNPs' interlayer. In addition to that CNTs/GNPs hybrids restricting cracks growth in resin, these hybrids could effectively suppress or deter crack propagation in the composite laminates. Yang et al. declared that long and tortuous CNTs can bridge within GNPs layers hence effectively inhibit the stacking on individual two dimensional GNPs resulting high contact area between hybrid agents and polymer matrix[159]. Shin et al. suggests super tough PVA composite reinforced with reduced graphene oxide (RGO)/carbon nanotube agents using water soluble SDBD as surfactant for mixing process followed by wet spinning technique which caused self-aligned composite fibres[37].

2.12 Hybrid GO and CNT (GONT) composites

On the other hand, Graphene oxide (GO), with the hydrophilic oxidation group, can be easily dispersed into water to form stable colloidal suspensions. This oxygenated graphene molecule, can be produced easily from oxidation of graphite flakes by hummer's method and currently is an inexpensive precursor used for large-scale production of chemically converted graphene. The oxygen-containing groups render GO sheets hydrophilic and highly dispersible in water, whereas the aromatic regions offer active sites to make it possible to interact with other aromatic molecules through π-π supramolecular interactions. Such a unique chemical structure offered new strategy to disperse un-functionalised CNTs in water with the aid of GO through π-π interactions without any surfactant. Studies on hybrid GO/CNT materials mainly focused in their energy storage applications however very few papers applied GO/CNT hybrid into polymer matrixes and obtained interesting properties.

2.12.1 Mechanical, thermal and electrical properties

The presence of GO facilitates the dispersion of CNTs, but Zhang have revealed that it is not the only reason for enhancing the thermal properties in PVDF/CNT/GO composites compared with the PVDF-CNT composites[160]. They indicate the presence of GO changed the crystalline behaviour of PVDF mainly to γ-form which is very dense structure and caused improved thermal conductivity.

Compared with the composite containing only 0.5 Vol% MWCNTs, the specific wear rate of the composite with the additional of 0.1 Vol% GO is further reduced by about 40%[155]. Two reasons were explained for improved tribological properties. One is the dispersion of MWCNT is greatly improved with the presence of GO due to its hydrophilic regions which can adsorb pristine MWNTs through p-stacking interaction, which would lead to a more stable dispersion of MWNTs in epoxy. On the other hand, the existence of reactive OH, carboxyl and epoxy groups on the GO nanosheets and their good mechanical interlocking arising from the wrinkled rough surface of GO would lead to an excellent interfacial adhesion between GO and epoxy.

Such beneficial approach in combining GO and CNT in composites can be applied into ceramic matrixes. In this regard, we tried to prepare well dispersed hybrid suspension of GO and MWCNT in Al_2O_3 to provide Al_2O_3-GONT nanocomposites with improved mechanical properties.

2.13 Potential Applications

Owing to the improved fracture toughness and ancillary benefits of electrical and thermal properties, ceramics reinforced with CNTs and GNPs are promising for numerous prospective applications in the field of photonics, biomedical, automotive and aerospace engineering. Firstly, associated with the enhanced mechanical performance of Al_2O_3, the significantly improved wear resistance property of these composites could be suitable for a number of wear and sliding applications in automobile industry like cylinder lines, valve seat and piston rings[47]. Secondly, the SiC and Si_3N_4 systems filled with CNTs made them suitable for structural applications, such as bearings, seals, armour, liners, nozzles and cutting tools. Thirdly, the thermally and chemically stable ceramic composites could revise their high thermal conductivity and be suitable for high temperature components such as in jet engine and brake disks for aircrafts[161]. Further, CNTs/GNPs can also convert ceramics into functional materials for aerospace and automobile industries, such as knock sensors, seat pressure sensors, temperature sensors, oil sensors, impact sensors and road surface sensors, whilst the outstanding electrical properties of CNTs/GNPs make Al_2O_3 ceramic attractive for specific applications like heating elements, electrical igniters, electromagnetic/antistatic shielding of electronic components, electrode for fuel cells, crucibles for vacuum induction furnaces and electrical feed through[162-164]. Table 2.3 summarises the potential industries may have interests for ceramic nanocomposites reinforced with CNTs and graphene. As the research is progressing in this important area, novel CNT-reinforced ceramics with stunning properties may appeal for automobile and aerospace.

Table 2.3 Potential applications of key ceramic nanocomposites reinforced with CNTs and graphene.

References	Ceramic matrix	Reinforcing agent	Key properties	Parts/Components	Potential industries
165	Al_2O_3	CNTs or GNP	Wear resistance, high toughness, electrical properties, thermal properties	Cutting tools, corrosion/erosion resistance pipes, electrical contacts, armour plates	Automobile, petrochemical industry, electric component manufacturing, defence industry
166	Si_3N_4	CNTs or GNP	Excellent mechanical, chemical, and thermal properties	Gas turbines, aircraft engine components and bearings	Power generation, aerospace, automobile sector
167	$BaTiO_3$	CNTs or GNP	Ferroelectrics, piezoelectric and colossal magnetoresistor properties	Electric generator, computer hard disks, sensors	Renewable energy, power generation, electronic, computer manufacturing, data storage, aerospace industry
168-170	ZrO_2	CNTs or GNP	High mechanical properties, excellent fracture toughness, elevated temperature stability, high breakdown electrical field and large energy bandgap	Solid oxide fuel cells, oxygen sensors and ceramic membranes	Renewable energy, chemical industry, water desalination sectors
171-173	TiN and FeN	CNTs or GNP	Excellent electrical properties	Capacitors, electronic conductor in electronic devices	Electrochemical industry, power and electronic sector, aerospace and automobile industries
174	Mulite	CNTs or GNP	High in electric and optical properties	Sensor	Electronic industry, aerospace sector and automobile industry

2.14 Conclusion

Advances in the ceramics reinforced with carbon nanostructures (CNTs and GNPs) have been thoroughly reviewed. Successes in the purification and dispersions of CNTs are somehow satisfactory, however further research and standards for CNT dispersion are vital for addressing the quality and reliability with confidence. CNT-reinforced CMCs follow the combined, advanced toughening mechanisms of CNT's stretching/uncoiling and the classical fibre pull-out theory, as an energy dissipating process.

It is clear that graphene can play an important role as fillers in ceramics according to publications. In addition to the exceptional mechanical properties of GNPs which are similar to CNTs, researches have shown that GNPs can be more easily dispersed in ceramic matrix than that of CNTs which is the key challenge in preparing CMCs. Additionally its 2D and flexible microstructure introduces a new toughening mechanism to the ceramic matrix (anchoring around the grain) that could absorb significant energy against crack propagations and delay the fractures. However, work on graphene-CMCs is in its early stages and there are still considerable works that need to be done to optimise their processing, microstructure and interfacial properties, in order to obtain better multifunctional properties from graphene-CMCs.

Chapter 3 Methodology

3.1 Introduction

This chapter covers the generic experimental methodologies and procedures used for this research work. Detailed technical information associated with specific experimentations will be further described in each relevant chapter. The techniques and methodologies for the fabrication, structural characterisation and mechanical properties evaluation of the Al_2O_3-GNP and Al_2O_3-GONT nanocomposites will be presented.

3.2 Fabrication of Al_2O_3-GNT and Al_2O_3-GONT nanocomposites

The fabrication of Al_2O_3-GNT and Al_2O_3-GONT nanocomposites was carried out at three different stages, including selection of starting materials, mixing procedure which is a very important stage in terms of obtaining proper dispersion of reinforcements in the matrix to gain appropriate functional properties in the composites, and the last sintering procedure.

3.2.1 Materials

The CNTs used in this study, provided by Tsinghua University, China, were produced by a standard CVD route, having an average outer diameter of 40 nm. GNPs (6-8 nm thick × 5 μm long) were purchased from ABCR GmbH & Co, Germany. Graphite flake was purchased from Sigma-Aldrich UK, to prepare graphite oxide (GO) by Hummers method. The detail of the GO preparation will be explained in section 3.2.2.1. High purity dispersible AlOOH (boehmite) provided by Sasol, Germany, was subject to annealing at 1000°C for 5 h, to obtain the γ-Al_2O_3 nanoparticles which were then used as the powder matrix material. This mixing process called powder mixing. Using the as-received AlOOH nanopowder directly as ceramic matrix without annealing procedure was called the sol-gel mixing technique. Sodium dodecyl sulphate (SDS)

surfactant was purchased from Sigma-Aldrich UK, for assisting the dispersion of CNTs in this research. The materials specifications are summarised in Table 3.1.

Table 3.1 Specifications of the raw materials used for the manufacturing of nanocomposites.

Material	Formula	Physical Shape	Size (nm)	Density (g/cm^3)	Melting point (°C)
Aluminium Oxide hydroxide	AlOOH	particle	20-40	3.9	2040
Aluminium Oxide	Al_2O_3	particle	20-40	3.9	2040
Graphene nanoplatelet (GNP)	C	nanoplatelet	6-8 nm thick × 5 µm wide	1.9	3652-3697
Graphite flake	C	Flake		1.9	3652-3697
Carbon nanotube (CNT)	C	nanotube	outer diameter 40 nm	1.85	3652-3697
sodium dodecyl sulphate (SDS)	$NaC_{12}H_{25}O_4$	particle	-	-	204-207

3.2.2 Mixing procedure

To prepare nanopowder composites, two different mixing strategies were introduced and their effects on microstructure and mechanical properties were investigated. The first mixing procedure was powder processing. In this technique, γ-Al_2O_3 nanoparticles prepared from thermal annealing of the AlOOH nanopowder were used for the composite nanopowder preparation. In the second technique which named sol-gel mixing, AlOOH formed a stable sol in water and after mixing with the carbon materials, the dried gel was used directly for later sintering process. Accordingly, to obtain Al_2O_3-GNT or Al_2O_3-GONT nanopowder composites via powder processing or sol-gel, a typical four steps processing was developed, which includes:

1- Dispersion of CNTs, GNPs and GO separately in water, determining the required GNT or GONT hybrid reinforcement contents in the final composites.
2- Dispersion of Al_2O_3 or AlOOH in water, depending on which mixing technique is chosen.
3- Final mixing of all the previously prepared suspensions.
4- Drying the suspensions to obtain Al_2O_3-GNT or Al_2O_3-GONT nanopowders, for later sintering process.

3.2.2.1 Dispersion of all carbon materials, separately, in water

The CNT dispersion

The raw CNTs were first chemically processed with a H_2SO_4–HNO_3 solution, to remove the residual metal catalyst, and to improve their dispersive properties. Using mixed oxidizing acid causes the CNT surfaces to change from hydrophobic to hydrophilic due to the carboxylic groups[175]. As an example, 3 g of CNTs were placed into a reaction beaker, and 20 ml HNO_3 (70%) was gently poured into it, followed by a slow addition of 10 ml H_2SO_4 (98%). The acid suspension was then gradually heated up to 130°C. After 25 min boiling, it was cooled down to room temperature. The CNTs were then carefully filtered from the suspension and subsequently rinsed several times with distilled water to remove traces of acid. A selected amount of acid-treated CNTs, depending on the content designed for the composites, as summarised in Tables 3.2 and 3.3, was then dispersed in water under probe-sonication, at a concentration of 1 mg/ml. A small quantity of SDS (< 2 wt% of the CNTs) was added, followed by 30 min probe-sonication to form a stable suspension. This suspension was then incubated for 2 weeks to allow for the surfactant thoroughly adsorbed onto the CNT surfaces.

GNP dispersion

This process is similar to the CNT dispersion, and a GNP suspension (1 mg/ml) with the assistance of SDS < 2 wt% of GNPs was prepared. In contrast to CNTs, there is no Van der Waal force amongst the GNPs, therefore no incubation step was applied and it is ready for the next mixing stage.

Synthesis of GO

GO was synthesized by a modified Hummers method[176]. Briefly, the graphite flake was oxidized with $KMnO_4$ in a concentrated H_2SO_4. 100 ml H_2SO_4 (98%) and 3.5 g graphite were placed in a reactor cooled to 0 ^oC. After mixing the suspension for 30 min, 0.5 g $KMnO_4$ was added in small portions to keep the temperature in the reactor at no more than 10 ^oC. A dark blue colour of graphite bisulphate was observed to form. 30 min later, 10 g $KMnO_4$ was added to the suspension gradually with a rate of addition slow enough to prevent the temperature of the suspension exceeding 20 ^oC. After the $KMnO_4$ feeding was finished, the reactor was heated to about 35 ^oC, and kept at this temperature for an additional 30 min. As the reaction progressed, the suspension became pasty and brownish in colour. At the end of this 30 min period, 150 ml water was slowly stirred into the paste to prevent violent effervescence, causing an increase in temperature to 90 - 95 ^oC. The suspension was then further treated with a mixture of 35 ml hydrogen peroxide (30%) and 265 ml water to reduce the residual permanganate and MnO_2 to a soluble $MnSO_4$. The warm suspension was filtered, resulting in a yellow-brownish filter cake. The cake was then further washed three times with aliquots (45 ^oC, 500 ml) of a ~3% HCl solution, and dried for a week.

GO dispersion

As mentioned in Chapter 2, GO is strongly hydrophilic therefore, in contrast to CNTs and GNPs, it can be easily dispersed in water without the aid of any surfactant. In this regard, GO suspension was prepared with water (1 mg/ml) without any surfactant, under probe-sonication for only 10 min to avoid any damage to the GO flakes, and a stable suspension was then obtained for next mixing step.

3.2.2.2 Dispersion of ceramic powder (Al_2O_3 or AlOOH) in water

Al_2O_3 dispersion

30 g of Al_2O_3 nanopowder was probe-sonicated for 20 min in 250 ml distilled water, named as suspension-C. The sonication time was optimized based on TEM observations, from 5, 10 and 20 min. Large Al_2O_3 agglomerates remain if it is treated for less than 20 min.

AlOOH dispersion

As AlOOH nanopowder will provide a stable sol in water, 30 g of AlOOH nanopowder was mixed slowly with 150 ml water under magnetic stirrers to prepare a stable transparent sol. After completing this stage, only 5 min probe-sonication was carried out for preparation of highly dispersed AlOOH sol.

3.2.2.3 Final mixing of all previously prepared suspensions

Powder possessing

For powder processing method, the prepared Al_2O_3 suspension was mixed with GNP and CNT suspensions under probe-sonication for 30 min, to obtain a well-mixed light grey Al_2O_3-GNTsuspension. Shorter sonication will result in discrete portion of dark and light grey colours for the suspension, which is an indication of improper mixing. After drying at 120 °C using a hot plate, the mixture was ground into loose Al_2O_3-GNT nanopowders, for subsequent sintering (HP or SPS). To obtain the optimum condition in density and mechanical properties, different combinations of the GNPs, CNTs and Al_2O_3 were prepared, as listed in Table 3.2. The samples designated as S_{X-Y}, where X represents the GNP wt% and Y for the CNT wt% in the composites.

Table 3.2 Selection of composition and sintering process for the sample preparation.

Sample ID	Matrix	GNP (wt%)	CNT (wt%)	Consolidation process	
				HP	SPS
S_{0-0}	Al_2O_3	0	0	√	√
$S_{0.5-0}$	Al_2O_3	0.5		√	
$S_{0.5-0.5}$	Al_2O_3	0.5	0.5	√	√
$S_{0.5-1}$	Al_2O_3	0.5	1	√	√
S_{03-1}	Al_2O_3	0.3	1	√	√
S_{1-1}	Al_2O_3	1	1	√	√
S_{1-2}	Al_2O_3	1	2	√	
$S_{0.5-2}$	Al_2O_3	0.5	2	√	√
S_{0-2}	Al_2O_3	0	2	√	
$S_{2-0.5}$	Al_2O_3	2	0.5	√	
S_{2-0}	Al_2O_3	2	0	√	
S_{5-0}	Al_2O_3	5	0	√	
S_{2-2}	Al_2O_3	2	2	√	

Sol-gel mixing

In the sol-gel technique, firstly the GO and CNT suspensions were mixed together under 5 min sonication to obtain a well-dispersed GONT suspension. Then, the previously prepared AlOOH sol was mixed with the GONT suspension under another 5 min probe-sonication. The mixture was dried at 120 °C and the dried gel was grounded and used for the synthesis of Al_2O_3-GONT nanocomposites. To obtain the optimum condition in density and mechanical properties, different amounts of GO and CNTs were applied in the Al_2O_3 matrix. The Al_2O_3-GONT nanocomposites were also prepared from the γ-Al_2O_3 matrix, instead of AlOOH to compare the sol-gel processing with powder processing in terms of microstructure and properties. The details of the prepared composites are listed in Table 3.3. The Al_2O_3-GONT nanocomposites prepared by powder processing were named as SP_{X-Y}, where X represents the GO wt% and Y for the CNT wt%. The Al_2O_3-GONT nanocomposites prepared by sol-gel were named as SS_{X-Y}, where X represents the GO wt% and Y refers to the CNT wt%.

Table 3.3 Selection of composition and sintering process for the sample preparation.

	Sample ID	Matrix	GO (wt%)	CNT (wt%)	Synthesis procedure
Powder processing	SP_{0-0}	γ-Al_2O_3	0	0	HP
	$SP_{0.5-0}$	γ-Al_2O_3	0.5	0	HP
	$SP_{0.5-0.5}$	γ-Al_2O_3	0.5	0.5	HP
	SP_{1-1}	γ-Al_2O_3	1	1	HP
Sol-gel	SS_{0-0}	AlOOH	0	0	HP
	SS_{1-1}	AlOOH	0.5	1	HP
	SS_{1-2}	AlOOH	1	2	HP
	SS_{2-4}	AlOOH	2	4	HP

3.2.3 Sintering procedure

All the pre-mixed composite powers with different wt% of reinforcements were sintered either by HP or SPS.

HP sintering

A hot-press furnace (HP W 25, FCT system, Germany) located at the University of Exeter is used in this study. The furnace features includes:

1- Working temprature up to 2200 °C, provided by electric resistant heating with a maximum 40 KW heating power.
2- Vacume 5×10^{-2} mbar
3- Maximum pressing force of 250 KN, provided by hydrolic force control system.
4- Optional working gases of Ar/N_2.
5- The temperature measurement and control using either axial/radial pyrometer or flexible thermocouples.

In a typical sintering process for the Al_2O_3-GNT composite, 25 g of the pre-mixed Al_2O_3-GNT powders were poured into the cavity of the graphite die (Fig. 3.1a). After assembling into the furnace, an external pressure of 40 MPa was applied to both ends of the die using graphite plungers, and the temperature was increased to 1650 °C at

a heating rate of 10 °C/min and held for 60 min under Ar atmosphere. Samples of 51 (length) × 51 (breadth) × 2.4 (thickness) mm were obtained after sintering as shown in Fig. 3.1c. Monolithic Al_2O_3 samples were also prepared under identical experimental conditions, for comparison.

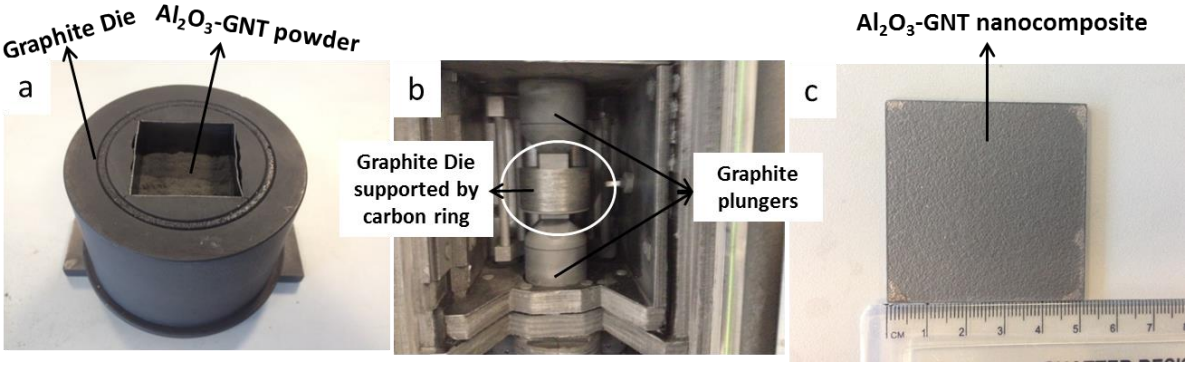

Fig. 3.1 (a) The graphite die with Al_2O_3-GNT powders inside during mould assembly, (b) Front view of the internal assembly of the HP furnace, and (c) The resulting Al_2O_3-GNT nanocomposite sample.

SPS process

A SPS furnace (HPD 25/1, FCT systems, Germany, Furnace) at Queen's Mary University of London was kindly offered for free access with technical support, for jointly assessing the effects of different sintering processes for the Al_2O_3-GNT composites. The main features of the furnace are:

1- Working temprature up to 2400 °C, with a maximum 25 KW heating power.
2- Vacume 5×10^{-2} mbar
3- Maximum pressing force of 250 KN, provided by hydrolic force control system.
4- Optional working gases of Ar/N_2.
5- Heating rate up to 1000 K/min (depending on tool size)
6- The temperature measurement and control were realised using either axial/radial pyrometer or flexible thermocouples.

Due to the smaller mould size in SPS than that of the HP machine, 10 g of Al_2O_3-GNT powders was assembled into the graphite die for each run (Fig. 3.2.). After the mould assembly, the sample was heated to 1400 – 1650 °C at a heating and cooling rate of 100 °C/min, with a simultaneously applied pressure of 40 MPa and a dwell time of 10 min under Ar atmosphere. After sintering, a disc sample of 20 mm diameter and 4 mm

thick was obtained. Monolithic Al_2O_3 samples were also prepared under identical experimental conditions.

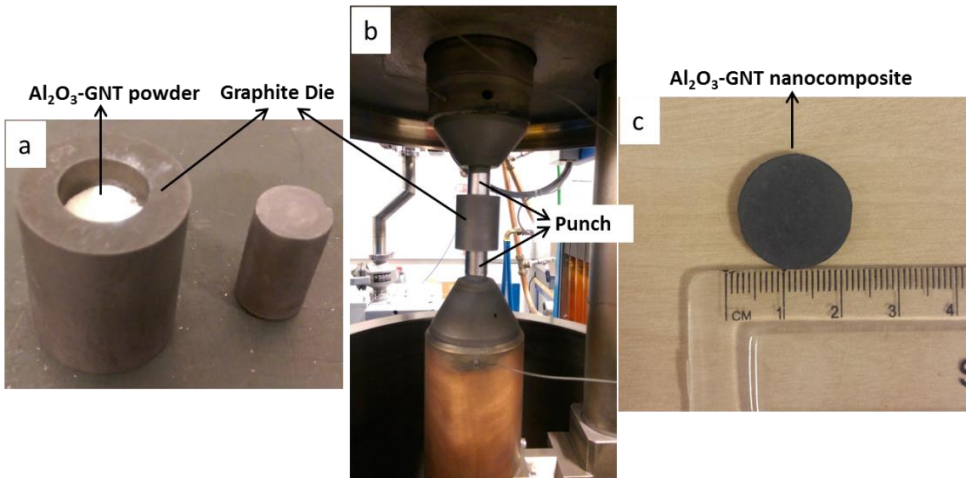

Fig. 3.2 (a) The graphite die with Al_2O_3-GNT powders inside during mould assembly, (b) The front view of the internal assembly of the SPS furnace, and (c) The as-synthesized Al_2O_3-GNT nanocomposite sample.

3.3 Structural Characterization

SEM

SEM is a powerful tool used to investigate the micro-structural features at high magnifications. In a standard SEM, a stream of electron produced by the filament (W or LaB6) is directed towards the sample, using a positive electrical potential. This stream is confined and focused by means of metal apertures and magnetic lenses onto a thin and focused monochromatic beam, as schematically demonstrated in Fig. 3.3(a)[177]. Electrons from the electron source either scatter elastically and produce back scattered electrons (BSE) or interact with the specimen resulting in the generation of x-rays and new electrons which are called secondary electron (SE). The signal produced by the SE is detected and processed using modern computer programmes and provides topographic information of surface of the sample. In this thesis, it is particularly suitable for observation of grain boundaries, cracks, pores and CNT pull-out on a fractured surface. This study used a Hitachi S3200N SEM to characterise the structural features, fractured samples and grain size measurements.

Prior to SEM observation, samples were carefully fractured to the required size and cleaned with acetone to remove any potential contaminations from the sample surface.

The fractured sample was then mounted using a conductive tape and was then coated with a very thin layer of Au to eliminate the problems associated with charging of the sample, and to provide a better conductive path between the sample and sample holder. To reveal the grain boundaries for grain size estimation using the SEM, the pre-polished samples were thermally etched for 15 min at 1400 °C under Ar atmosphere in a tube furnace.

TEM

TEM is capable of attaining very fine structural information from the projection of a material, to reveal its inside information. TEM uses electron beams in the similar fashion as described for SEM, however the electron beam is transmitted through an ultrathin specimen in this case, and an image is formed from the interaction of the electrons transmitted through the specimen. The image is magnified and focused with the help of electromagnetic lenses onto a florescent screen which is sensitive to electrons, so that the image can be further recorded on a photographic film or digitised to be stored onto a computer[177]. A schematic representation of a TEM is shown in Fig. 3.3(b)[177]. Besides direct electron microscopy imaging, TEM also records electron diffraction patterns from samples. These diffraction patterns are formed at the back focal plane and image plane of the objective lenses respectively, providing important information regarding crystal structures and crystal orientations of the sample. TEM images can be formed either using the direct beam or scattered electrons. For this purpose, an aperture is inserted into the back focal plane of the objective lens which allows the direct beam of electrons to go through, and the resulting image is called a bright-field image. Thicker regions of the sample or regions with a higher atomic number appear darker, whilst regions with no sample in the beam path appear brighter, hence termed as bright-field. In contrast to this, a dark-field image is formed when the scattered electrons are selected by the aperture. High-resolution transmission electron microscopy (HRTEM) allows the imaging of the crystallographic structure of a sample at an atomic scale. Because of its high resolution, it is an invaluable tool to study nanoscale features of crystalline materials, such as semiconductors, metals and composites.

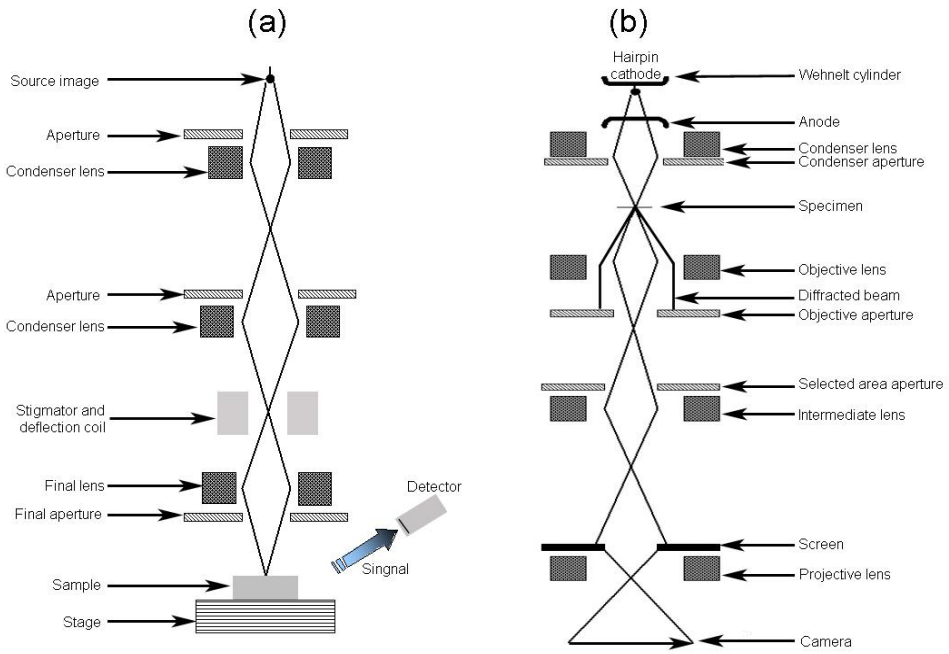

Fig. 3.3 Schematics of electron microscopes. (a) SEM, and (b) TEM[177].

A JEM2100, TEM (LaB6, 200 kV) was used to characterise the crystallinity of the composites, particularly the interfacial connection between GNP, CNT and the Al_2O_3 matrix. The conventional TEM sample preparation procedure is time consuming and complex. Therefore two methods, chemical etching and Ar ion milling, were adopted for the TEM sample. Both techniques produced good quality thin samples that were suitable for TEM investigations. Chemical etching is a rather simple, straightforward and efficient method for Al_2O_3. The TEM samples were prepared by deep etching of finely-milled sintered nanocomposites, using NaOH solution for two weeks followed by thorough rinsing with distilled water in order to remove traces of NaOH and by-products. The clean samples were dispersed in acetone, under probe sonication, and the suspension was then transferred dropwise onto a 3 mm, lacey carbon-coated Cu TEM grid. After the acetone was evaporated at room temperature, the sample was then ready for further observation. In the Ar ion milling method, thin sections from the bulk Al_2O_3-GNT samples were cut using a diamond cutting wheel (Struers, M0D08) with 0.15 mm blade thickness. The Al_2O_3-GNT samples were polished on both sides by 9 µm, 3 µm and 1 µm diamond suspension on polishing pad to obtain Al_2O_3-GNT samples of 100 nm thick, then were Ar ion milled to develop a hole. The area around the hole will produce the desired thickness to be used for TEM study.

XRD

X-ray powder diffraction (XRD) technique was employed to identify the crystallographic structure of the samples. When x-rays are directed to the surface of crystalline materials they produce constructive interference after reflection. The relationship between the incident and reflected X-rays is expressed by Bragg's equation 3.1[178].

$$n\lambda = 2d\sin\theta \quad (3.1)$$

where λ is the wavelength of the X-rays, d is the inter-lattice spacing, θ is the incident angle and n is an integer. Samples were characterised on the basis of patterns, shaped by plotting the diffracted peaks at 2θ and their respective intensities.

XRD investigations were performed using a Bruker D8 Advance X-ray Differactometer. Pre-polished solid samples and finely milled powder samples were used for the XRD measurements. The analysis was generally performed at a 2θ step rotation of 0.02°, with a dwell time of 5 s at room temperature (~25°C).

Raman

A Raman spectroscopy (Renishaw RM1000) was also used to evaluate the structural changes of both GNPs and CNTs before and after the sintering processes, and the wear testing.

When a laser light interacts with atoms in molecules, a Raman spectroscopy will detect the scattered light produced from vibrating atoms. The intensity of the scattered light (y-axis) for each energy (frequency) of light (x-axis) is spotted. The frequency is traditionally measured in a unit called the wavenumber (number of waves per cm, cm^{-1}). Raman spectroscopy is a very useful tool to study carbon atom that make up the structure of diamond, because it has a single crystal structure with regular arrays of identical carbon atoms, all in the same configuration. In these cases, there is often one dominant Raman band because there is just one molecular environment of the crystal). However, the dominant vibration mode for both CNT and GNPs is around 1585 cm^{-1} (the G band) assigned to the scattering of the E_{2g} phonon from sp^2 carbon (graphite lattice), and the D band around 1350 cm^{-1} resulting from the structural imperfections and finally another vibration around 2700 cm^{-1} which is 2D band.

Additionally, Raman is a non-destructive test, with little sample preparation required for a very small amount of materials[179].

3.4 Density and mechanical property evaluations

Density

In this study, the densities of sintered materials are measured by following the Archimedes principle, which states that the apparent weight of an object immersed in a liquid decreases by an amount equal to the weight of the volume of the liquid that it displaces, equation 3.2[180].

$$D = \frac{W_{air}}{W_{air} - W_{liquid}} \qquad (3.2)$$

where D is the bulk density, W_{air} is the weight of the sample in air and W_{liquid} is the weight of sample in liquid. Distilled water was used as the liquid and analytical balance with an accuracy of $\pm$ 0.01 mg was employed. The relative densities were calculated by dividing the apparent density by the theoretical density. 3.90 mg/m^3, 1.9 mg/m^3 and 1.85 mg/m^3 were adopted as the theoretical densities for Al_2O_3, GNP and CNT respectively[180].

Hardness

Hardness testing is a simple and fundamental technique to assess the mechanical property of materials, and is theoretically defined as the resistance of a material to a plastic deformation[181]. Prior to the hardness testing, the sintered samples were cut using a resin-bonded diamond disc cutter and cold mounted. During cold mounting, the samples were vacuum infiltrated using epoxy resin. After mounting, the samples were first ground on diamond pads of 120 and 220 grit and then polished to 6 µm and 1 µm by using DP-Suspension on polishing cloths. Vickers hardness testing was carried out at 5 kg loads for 15 sec using a Leco (V-100-A2) Hardness Tester. For each sample, an average of five indents (equally spaced) was recorded. The diagonal lengths of the indents were measured using the attached microscope and further

converted to Vickers hardness number (HV) using following relationship, equation 3.3[182].

$$H = 1.8544\left(\frac{P}{d^2}\right) \quad (3.3)$$

where the hardness (*H*) is related to the average diagonal length (*d*) of the indentation and the contact load (*P*), and the corresponding unit of hardness Vickers, HV, (kgf/mm^2) was further converted to Pascal (Pa).

Flexural strength

Flexural strength is defined as the strength of a material in bending at the instant of failure, and is expressed by equation 3.4 for three point bending which was used in this study[180]:

$$\sigma_f = \frac{3FL}{2bd^2} \quad (3.4)$$

where F is the load at the fracture point, L is the span length, b is the sample breath and d is the sample thickness. In this study, the flexural strength was measured using bending and tensile test machine model EZ20. The breaking load was measured by using a 500 N load cell. For each test, three samples were cut from the hot-pressed plate using a resin-bonded diamond cut-off wheel (Struers, UK). The size of specimens was 20 mm (length) × 2 mm (breadth) × 2.2 mm (height), according to the standard (ASTM C1161–13). Before testing, all faces of sample were carefully ground using diamond pads down to 220 grit followed by fine grinding down to 9 μm and then polished on cloths using 6 μm and 1 μm DP-Suspensions. The bending span and the loading speed were 20 mm and 0.5 mm/min, respectively.

Fracture toughness

The single edge notch beam (SENB)

As the SENB method is the most reliable method for fracture toughness measurement in ceramics, it was then used in this thesis to assess the fracture toughness of our samples. For each sample, four notched specimens with identical dimensions of 14 mm (length) × 2.6 ± 0.20 mm (breadth) × 2.2 ± 0.15 mm (height) were cut using the

resin bonded diamond blade. A U-notch was cut across the mid plane of each bar, as shown in Fig, 3.4. Before testing, all faces of sample were carefully polished to 1 μm using DP-Suspension on polishing cloths. The depth of the notch was determined by equation 3.5, according to the ASTM standard (ASTM C1421–99)[183].

$$\alpha = \frac{a}{W} = 0.5 \pm 0.05 \qquad (3.5)$$

where α is the depth of notch and *W* is the thickness of the sample. The depth of the notches was measured by an optical microscope to ensure it is in the standard range. The test was carried out using a bending span of 8 mm and a loading speed of 0.01 mm/min, to achieve slow crack propagations across the notch.

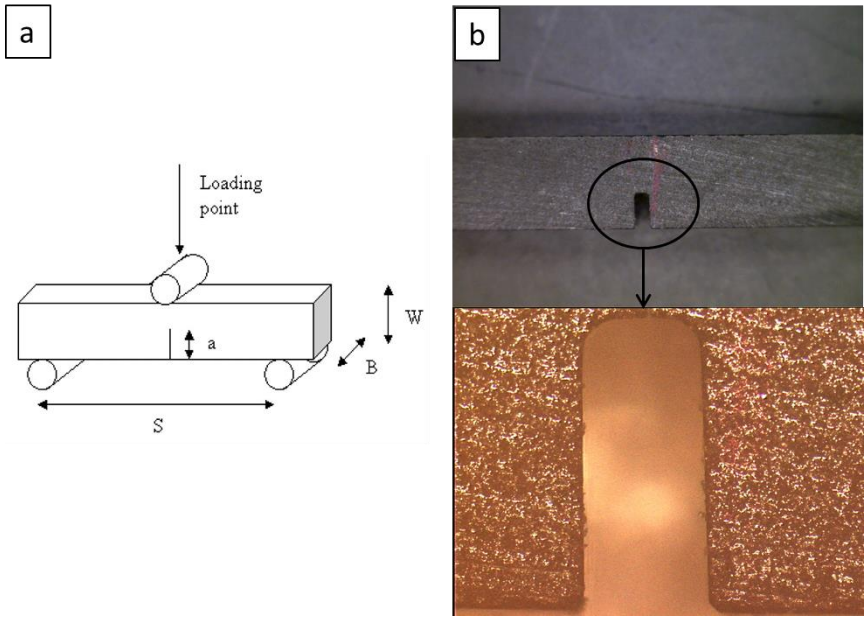

Fig. 3.4 a) Schematic of the fracture toughness measurement using the SENB method, and (b) the U shape notched specimen.

The fracture toughness, K_{IC}, was calculated according to equation 3.6[183].

$$K_{IC} = \frac{3P_{max}L}{2BW^{3/2}}\alpha^{1/2}Y \qquad (3.6)$$

where P is the breaking load, L is the bending span, B is the specimen width, W is the specimen height, and Y is the calibration factor which can be calculated using equation 3.7[183].

$$Y = \frac{1.99 - \alpha(1-\alpha)(2.15 - 3.93\alpha + 2.7\alpha^2)}{(1+2\alpha)(1-\alpha)^{1.5}} \quad (3.7)$$

Brittleness Index (BI)

It has been shown that the brittleness index (BI), defined as the H/K_{IC} ratio of a material which reflects the combined responses of the material, is a better parameter for the quantification of wear resistance than taking either the H or the K_{IC} alone separately[184]. Accordingly, BI was measured using equation 3.8, where *H* represents the hardness and K_{IC} for the fracture toughness of the material[184].

$$BI = H / K_{IC} \quad (3.8)$$

3.5 Tribological and wear testing

Wear properties of the Al_2O_3-CNT nanocomposite samples were evaluated in dry sliding against a Si_3N_4 ball counterpart, at various loads. Monolithic Al_2O_3 samples were also studied for comparison. The friction and wear experiments were performed at The University of Nottingham, using a ball-on-reciprocating flat sample surface, at room temperature using a wear rig as illustrated in Fig. 3.5.

The Si_3N_4 ball, purchased by Dejay Ltd, UK, having ϕ 6.3 mm, was used against flat sample surfaces which were polished to 1 μm finish with diamond slurry. Tests were carried out at loads of at 5, 15, 25 and 35 N, at a fixed sliding speed of 10 mm/sec, with the reciprocating stroke of 10 mm. Each test lasted for 120 min and three samples were tested in each case. The friction force was transferred to a load cell and an electrical output generated by the load cell was recorded throughout the tests to obtain coefficient of friction value.

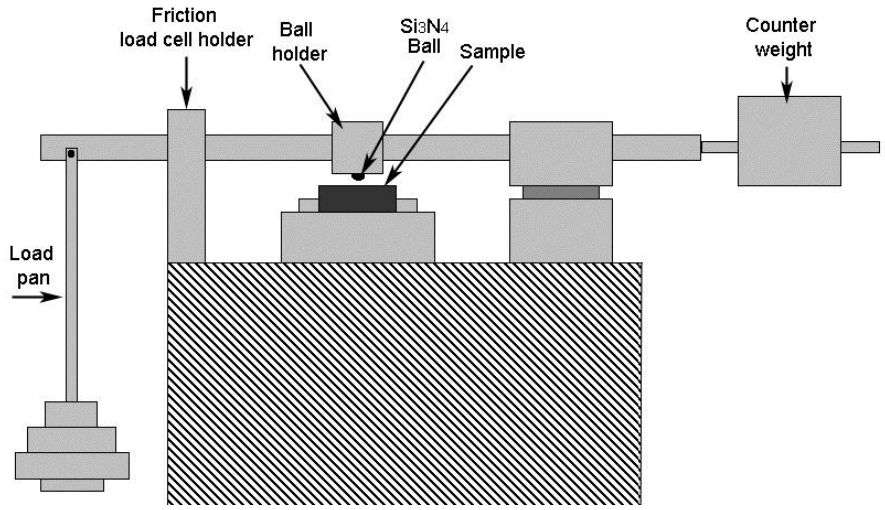

Fig. 3.5 Schematic diagram of the wear testing rig.

After testing, the worn surfaces of each sample were examined using the SEM. The cross-sectional area of the wear track was further measured using a TALYSURF CLI 1000 profilometer by Taylor/Hobson Precision, UK. The volume loss of the samples, calculated utilising the TalyMap Universal software, was used in wear rate calculations, defined by the following equation 3.9[185]:

$$W = \frac{V}{LF} \qquad (3.9)$$

where L is the sliding distance, F is the applied load, and V the wear volume.

Chapter 4 Fabrication and structural investigations of Al_2O_3-GNT nanocomposites

4.1 Introduction

For high quality Al_2O_3-GNT nanocomposite fabrication, eliminating the agglomeration of GNTs and achieving high sintering densities are the two main challenges. Bearing this in mind, two aspects will be presented in this Chapter: the first is to investigate the method of achieving homogenous dispersion of GNTs within the Al_2O_3 matrix; and the second aspect will cover the consolidation processes for high density Al_2O_3-GNT nanocomposites. Two different pressure-assisted sintering methods, named as HP and SPS, will be applied in this thesis. On the basis of the property and microstructure assessments, the roles of different GNT contents in the structural features of Al_2O_3-GNT composites are presented, and both consolidation processes will be compared against each other.

4.2 Al_2O_3-GNT nanopowder dispersion

The main challenge in the preparation of ceramic-based composites is to find the optimum conditions for the homogeneous dispersion of reinforcements with the ceramic nanoparticles, with minimal or without any damage to the reinforcement agents. Apart from using SDS as a surfactant, the sonication parameters such as the sonication time and the volume of the suspension play a very important role in achieving uniform dispersion of the starting materials. A short sonication time for the Al_2O_3 nanopowder (5 min) leads to large agglomerates remaining in the suspension, therefore the GNT reinforcements cannot properly attach to the surface of individual Al_2O_3 nanoparticles, as evident in Fig. 4.1a and b. However, a prolonged sonication can damage the GNT reinforcements, as revealed in Fig. 4.1c in which CNTs appear to be shortened and torn down into smaller parts after more than 30 min probe-sonication. The shortened length of the CNTs will lose their merit in functionalizing the composite matrix. Therefore, the optimized probe-sonication time was adjusted for 30 min for the preparation of stable CNT suspensions. As described in section 3.2.2.1, 2

week incubation time was allocated to the CNT suspensions, to allow the SDS thoroughly adsorbed onto the CNT surfaces.

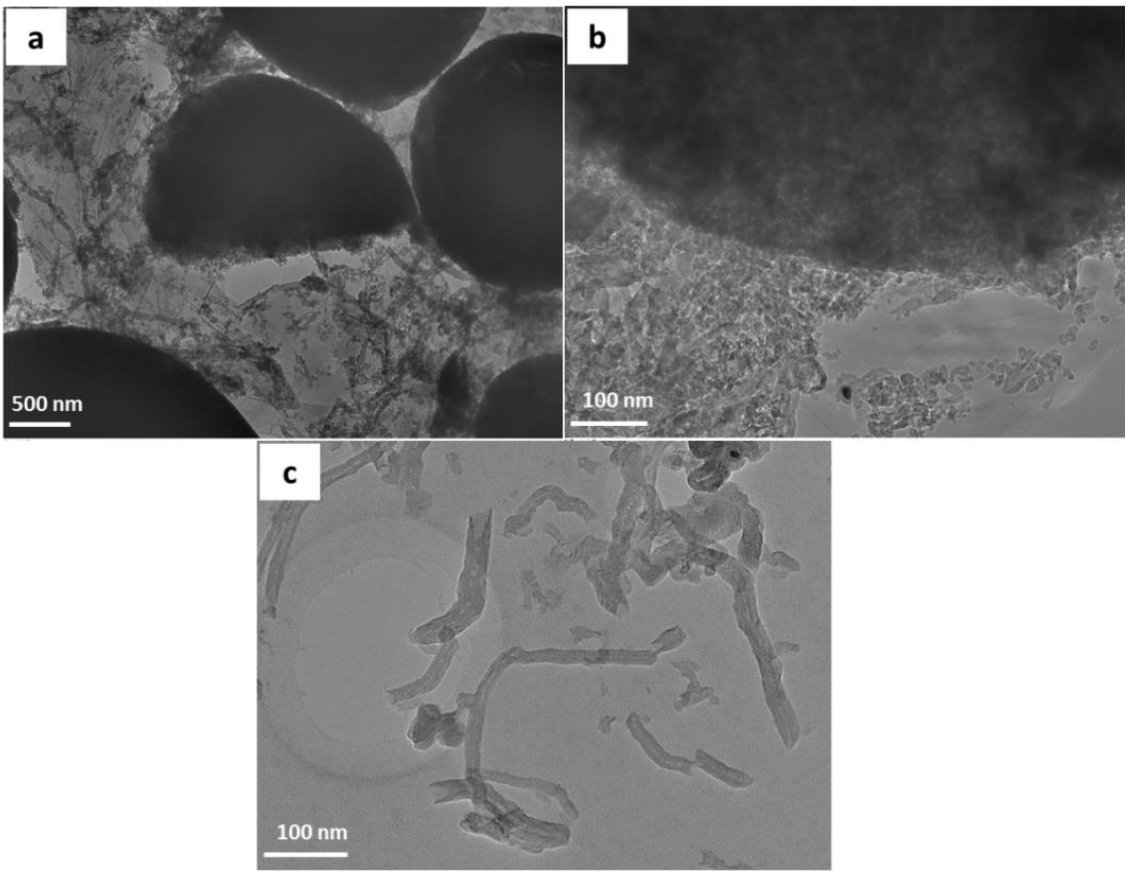

Fig. 4.1 TEM images of CNTs from different dispersion processes. (a) Al_2O_3-GNT nanopowders with hollow Al_2O_3 agglomerates, (b) Al_2O_3 agglomerates at higher resolution, and (c) Damaged CNTs appearing as broken and shortened small pieces, due to a prolonged probe-sonication of over 30 min.

After appropriately selecting the sonication time, undamaged and highly dispersed Al_2O_3-GNT nanopowders can be achieved, as shown in Fig. 4.2a. The Al_2O_3 nanoparticles were completely de-agglomerated, appearing to have a particle size of 20 nm attached to the surface of individual CNTs and GNPs (Fig. 4.2.b-c), and there is no damage to the GNT reinforcement under current mixing parameters.

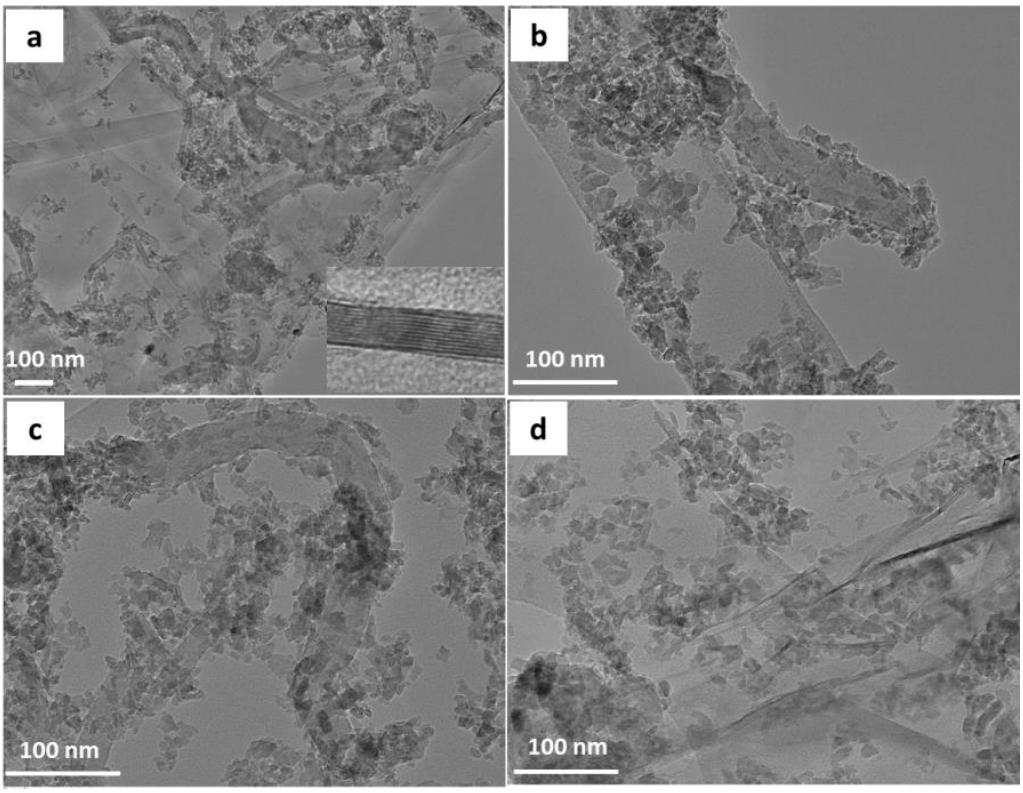

Fig. 4.2 TEM images. (a) Al_2O_3-GNT nanopowders after optimized probe-sonication time. (b) and (c) Al_2O_3 nanoparticles attached to the CNT, and (d) Al_2O_3 nanoparticles attached onto the GNP surfaces.

4.3 Consolidation of Al_2O_3-CNT nanocomposites

Al_2O_3 and its GNT-reinforced nanocomposites were consolidated using both HP and SPS. During sintering, the densification and grain growth occur simultaneously, which determines the final properties of the sintered materials. Therefore, the selection of a suitable sintering process is extremely important. The effect of sintering profiles and GNP/CNT additions on the density, microstructure and grain sizes of Al_2O_3-GNT nanocomposites will be discussed, as follows.

4.3.1 HP process

HP process involves the simultaneous application of pressure and heat to a powder system, to achieve higher densities and better mechanical properties than a pressureless sintering. During this process, the heat is transferred from the graphite

heating elements surrounding the pressing tool via radiation/convection, thus heating rate is limited to 20 °C/min. The slow heating, however, results in a homogeneous distribution of the heat within the sample, which is beneficial for achieving uniform structures.

4.3.1.1 Sintering profile

Fig. 4.3 shows a complete sintering profile applied to the HPed monolithic Al_2O_3. The blue line corresponds to the shrinkage rate which relates to the speed of piston traveling, the red line relates to the sintering temperatures, and the pressure profile is shown as the black line. The heating rate was 20 °C/min up to 900 °C, and then reduced to 10 °C/min to allow for uniform temperature distribution across the entire sample during the sintering process. The whole process takes 225 min (red graph).

The blue line or the shrinkage rate profile for Al_2O_3 shows two main peaks, which can be attributed to the phase transformation and densification processes, respectively. Since the starting Al_2O_3 powder was in gamma phase, the peak at ~1400 ^oC is believed to correspond to a phase change from the gamma to alpha, and such a phase transformation peak was not seen in other reports that used alpha-Al_2O_3 [84]. The second shrinkage rate peak at ~1600 ^oC corresponds to the densification of the Al_2O_3, which produced further volume shrinkage.

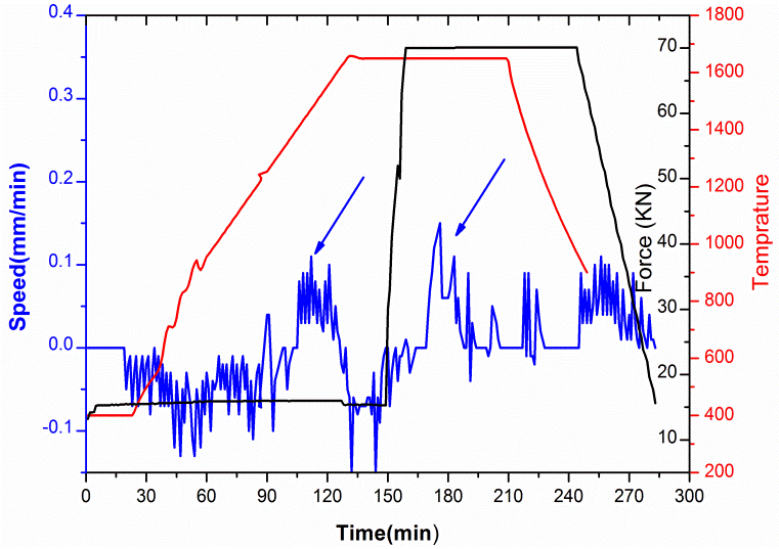

Fig. 4.3 The HP sintering profiles of pure Al_2O_3: the volume shrinkage rate (blue line), temperature (red line), and pressure (black line).

4.3.1.2 Effect of GNP/CNT combinations on the density of Al_2O_3-GNT

At various GNP/CNT ratios sintered under the same conditions, the densities of the resulting composites are presented in Table 4.1. The relative density of pure Al_2O_3 is 98%, which indicates a successful sintering procedure, thus the same heating recipe as described in section 4.3.1.1 has been used for other composites. At low GNT contents, the relative densities are very high, > 99%. However, with the addition of >0.5 wt% of GNPs and >1 wt% of CNTs, the densities of the composites started to decrease, in line with the associated difficulties in the GNT dispersion at higher contents.

The relative density in ceramic nanocomposites is an indirect indicator for assessing the dispersion of second phases in the matrix, as higher densities are indicative of a better dispersion and normally resulting in better mechanical properties[21,57]. In Table 4.1, samples at specific GNP/CNT ratios exhibited relative densities of > 99%. It seems that the dispersion of GNTs was quite successful, which is further supported by the SEM analyses (Fig. 4.5). The higher relative densities in composites than in the monnolithic Al_2O_3 in this work were also shown by other reports[186,187]. It is possible that the inclusion of GNTs (at some fractions) acted as a sintering agent, due to their lubricating effect which might help better packing of the Al_2O_3 particles during the

sintering process, thus resulting in an overall improved composite densities. Another possible reason for the higher density in the nanocomposites might be attributed to the 2D morphology of the GNPs in the matrix, as they have less an issue during the dispersion compared with CNTs, thus may help to improve the final density. All the controlling factors in CNT's poor dispersion such as fibrous morphology, high aspect ratio, Van der Waals interaction, and the presence of residue catalysts, do not exist in the case of GNPs, therefore their dispersion process was easier than that of CNTs.

Table 4.1 Theoretical and relative densities of the composites and their sintering conditions.

Sample	Matrix	GNP (wt%)	CNT (wt%)	Sintering Schedule	Relative density
S_{0-0}	Al_2O_3	0	0	1650 ºC/40 MPa/1 hour/Ar	98%
$S_{0-0.5}$	Al_2O_3	0	0.5	1650 ºC/40 MPa/1 hour/Ar	99.2%
$S_{0.5-0.5}$	Al_2O_3	0.5	0.5	1650 ºC/40 MPa/1 hour/Ar	99.3%
$S_{0.5-1}$	Al_2O_3	0.5	1	1650 ºC/40 MPa/1 hour/Ar	99.9%
S_{1-1}	Al_2O_3	1	1	1650 ºC/40 MPa/1 hour/Ar	99%
$S_{0.5-2}$	Al_2O_3	0.5	2	1650 ºC/40 MPa/1 hour/Ar	99%
S_{0-2}	Al_2O_3	0	2	1650 ºC/40 MPa/1 hour/Ar	97.5%
$S_{2-0.5}$	Al_2O_3	*2*	0.5	1650 ºC/40 MPa/1 hour/Ar	98%

4.3.1.3 Structural features

XRD

The XRD profiles show the typical peaks of α-Al_2O_3 in all nanocomposites, without any detectable carbide phases, indicating no significant reactions between GNTs and Al_2O_3 during the sintering. At increased GNP/CNT ratios, a new peak is observed at 26.3 degrees which corresponds to the crystalline graphite. The composites with 2 wt% GNP ($S_{2-0.5}$) showed the clear graphitic peak at 26.3 degrees; whilst almost no graphitic peaks for the composite containing 2 wt% CNTs ($S_{0.5-2}$). The platelet structure

of the GNPs makes the (002) planes dominant and easily detectable for XRD, compared with those containing the same amounts of CNTs.

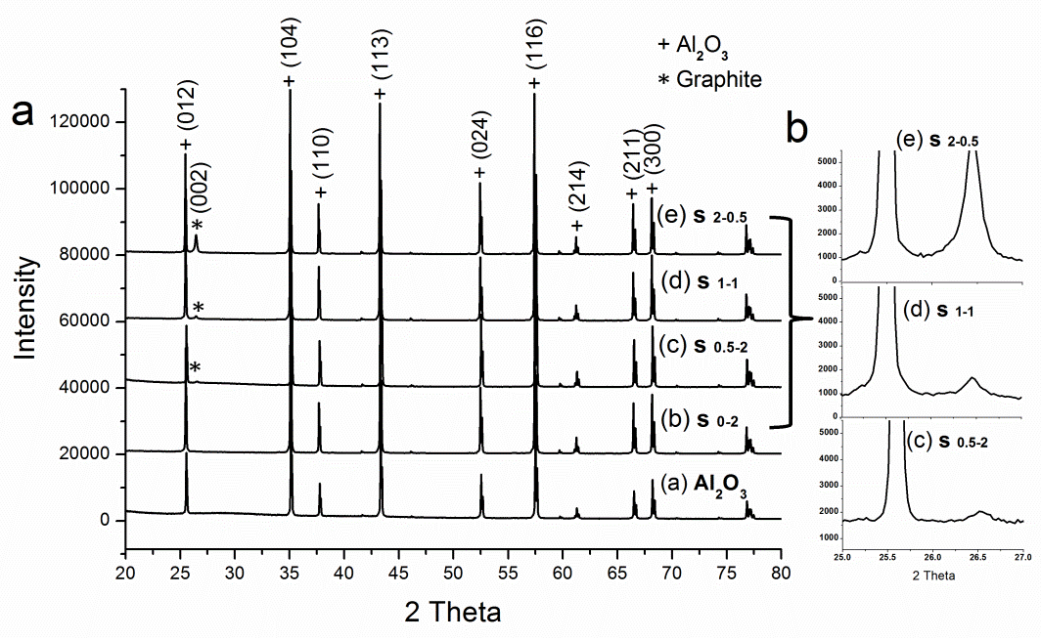

Fig. 4.4 (a) XRD patterns of the monolithic Al_2O_3 and Al_2O_3-GNT nanocomposites with different GNP/CNT contents, and (b) the zoomed sections of samples $S_{0.5\text{-}2}$, $S_{1\text{-}1}$ and $S_{2\text{-}0.5}$.

Raman

To investigate the effect of sintering process on the structure of GNP and CNT reinforcements, Fig. 4.5 shows the Raman spectra of the pure GNP, pure CNT, $S_{0.5\text{-}0}$ and $S_{0.5\text{-}1}$ composites. The G-band at ~1582 cm^{-1} has been observed in both spectra of the GNP and CNT samples. The G band is due to the stretching of the C-C bond in graphitic materials which is common to all sp^2 carbon systems, and it is very sensitive to any damage to the hexagonal symmetry of sp^2 carbon nanomaterials. The sharp G band after sintering in nanocomposites reinforced with CNT and GNP has indicated that the hybrid GNT reinforcements remained undamaged after the sintering.

The small band around 1350 cm^{-1} is known as the D band, is often referred to as the disorder band or the defect band theretofore it occurrence indicates the presence of some disorder to the graphene structure. Accordingly, the more prominent D band in the Raman spectra of pure CNTs compared with pure GNP indicates a more disordered structure of the CNTs. The spectrum of the composite also shows a similar

pattern in D band. In the other words, a higher intensity of the D band is observed in $S_{0.5\text{-}1}$ compared with $S_{0.5\text{-}0}$.

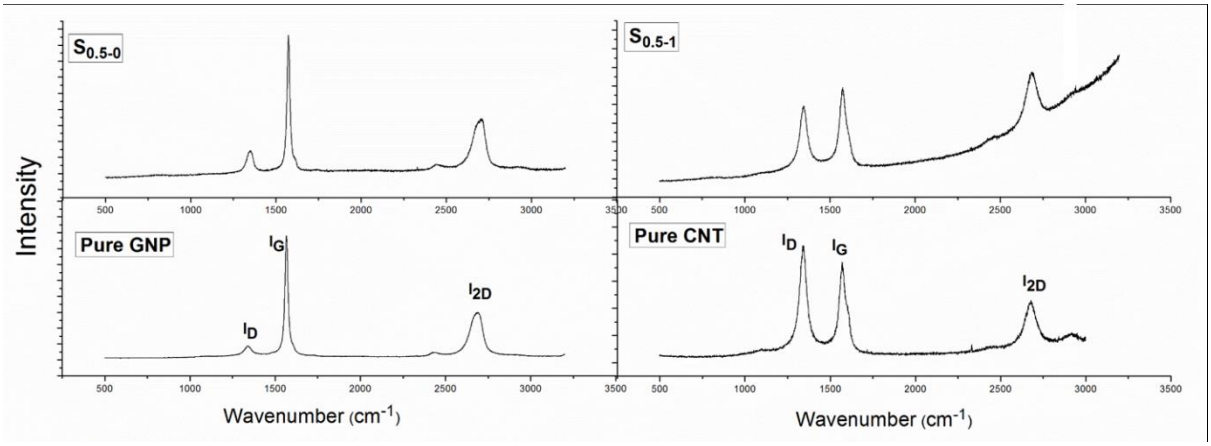

Fig. 4.5 The comparison of Raman scans of pure GNP, pure CNT, $S_{0\text{-}0.5}$ and $S_{0.5\text{-}1}$.

Effect of GNT additions on the microstructure

Fig. 4.6a-f shows SEM images of fractured surfaces of the m onolithic Al_2O_3 and Al_2O_3-GNT nanocomposites with various GNT contents. The fracture mode changed from inter-granular in the monolithic Al_2O_3 to blurry and glaze-like trans-granular mode in the composites. Such changes in the fracture mode is due to the addition of GNT reinforcement in the matrix. This means that the GNT addition made the grain bounderies stronger, and the fracture progressed from inside the grains instead of along the grain boundaries, compared with the pure Al_2O_3. The trans-granular fractured areas increased with increasing the GNT content, up to $S_{0.5\text{-}1}$. Higher addition of GNT at $S_{1\text{-}1}$ (Fig. 4.6.e) has led to severer GNP and CNT agglomerations, with inhomogeneous microstructure due to difficulties in dispersion. The large agglomerates of CNT can be seen in $S_{1\text{-}1}$, as shown in Fig. 4.6f.

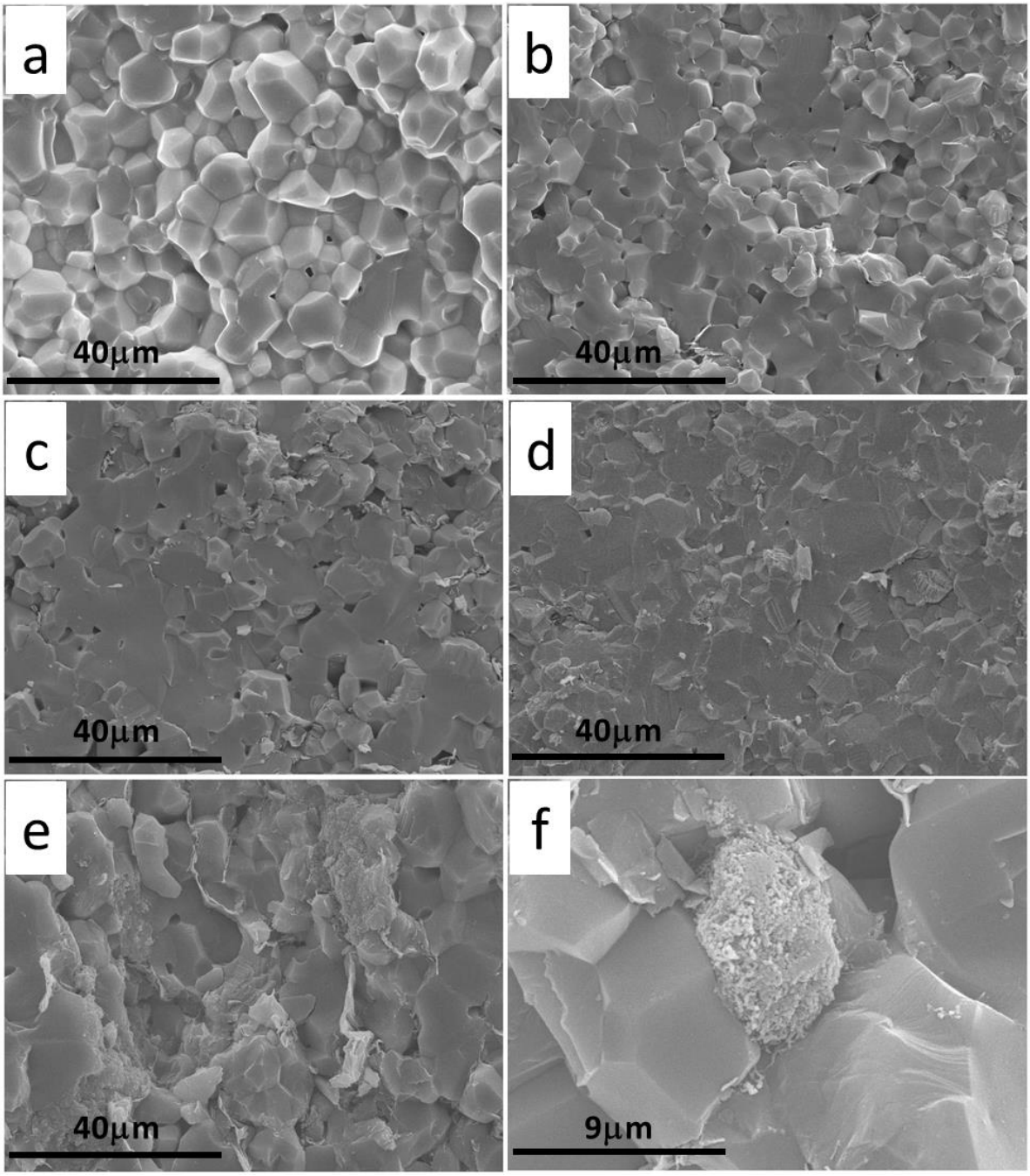

Fig. 4.6 SEM images of fractured surfaces: (a) Monolithic Al_2O_3 exhibiting an inter-granular fracture mode, (b-d) $S_{0.5\text{-}0}$, $S_{0.5\text{-}0.5}$ and $S_{0.5\text{-}1}$, respectively, showing a trans-granular fracture mode, (e) and (f) showing the GNT agglomerates in $S_{1\text{-}1}$.

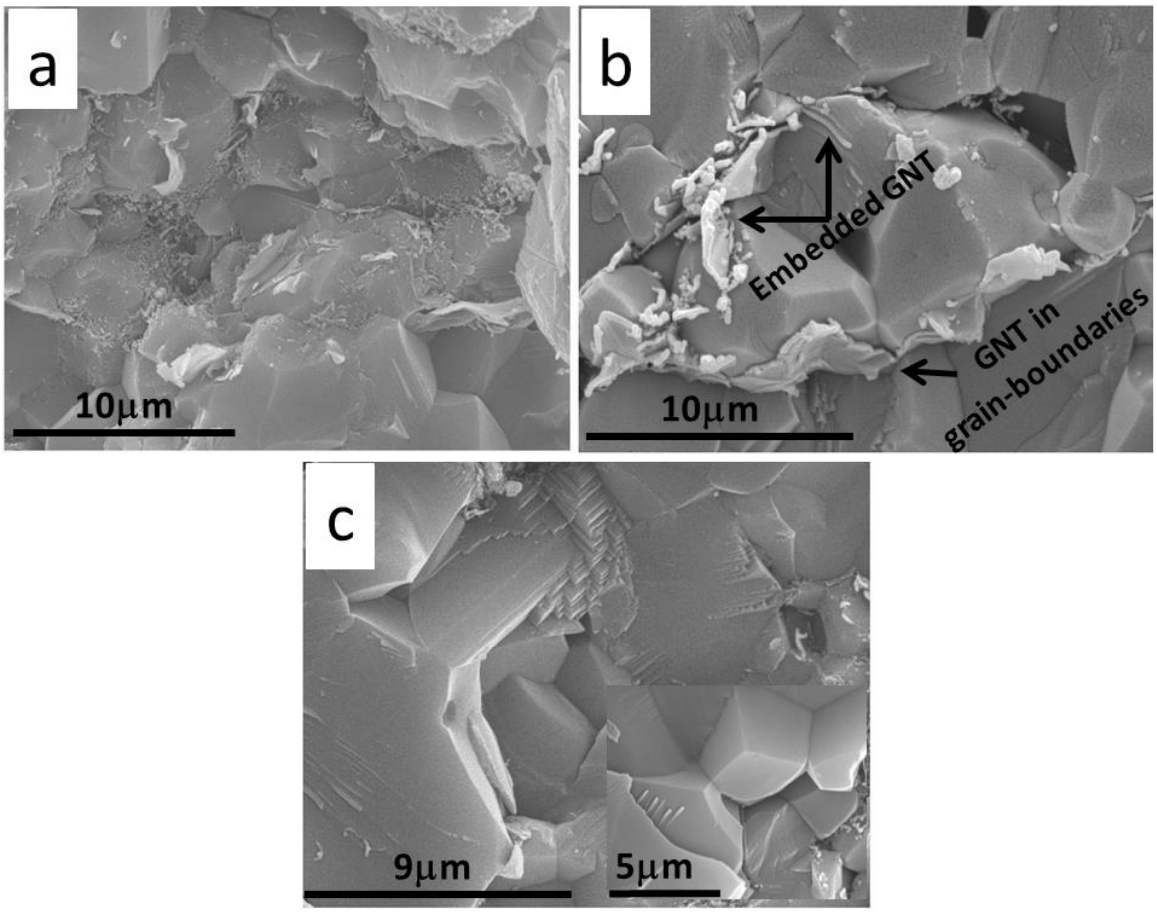

Fig. 4.7 SEM images of fractured surfaces of Al_2O_3-GNT nanocompsites ($S_{0.5-1}$) showing: (a) a good dispersion of GNT in the Al_2O_3 matrix, (b) GNTs embedded inside the grains and in the grain boundaries, and (c) the laminated structure in Al_2O_3 matrix.

Meanwhile, the dispersion of GNTs within the fractured area appears to be uniform (Fig. 4.7a), which is in consistent with the high relative density obtained for the Al_2O_3-GNT nanocomposites (Table 4.1). The GNTs were mostly accumulated around grain boundaries (Fig. 4.7b), however some were trapped inside the grains. Another interesting effect of GNT addition on the microstructure is the laminate microstructure in the Al_2O_3-GNT composite, as shown in Fig. 4.6d, which is thought to be related to the effect of GNTs on the grain refinment, as reported by Inam et. al.[188]. These laminated materials composed of layers of differently sized grains that were co-sintered together, illustrating the influence of GNTs on the microstructure.

Grain size

The structural features of thermally etched surfaces of the monolithic Al_2O_3 and $S_{0.5\text{-}1}$ are shown in Fig. 4.8a and b, which reveals the grain refining effects of GNTs on the composites. As shown in Fig. 4.7b, the GNTs accumulating in the grain boundaries prevented the grain growth during sintering, and resulted in the grain refinement in Al_2O_3-GNT nanocomposites.

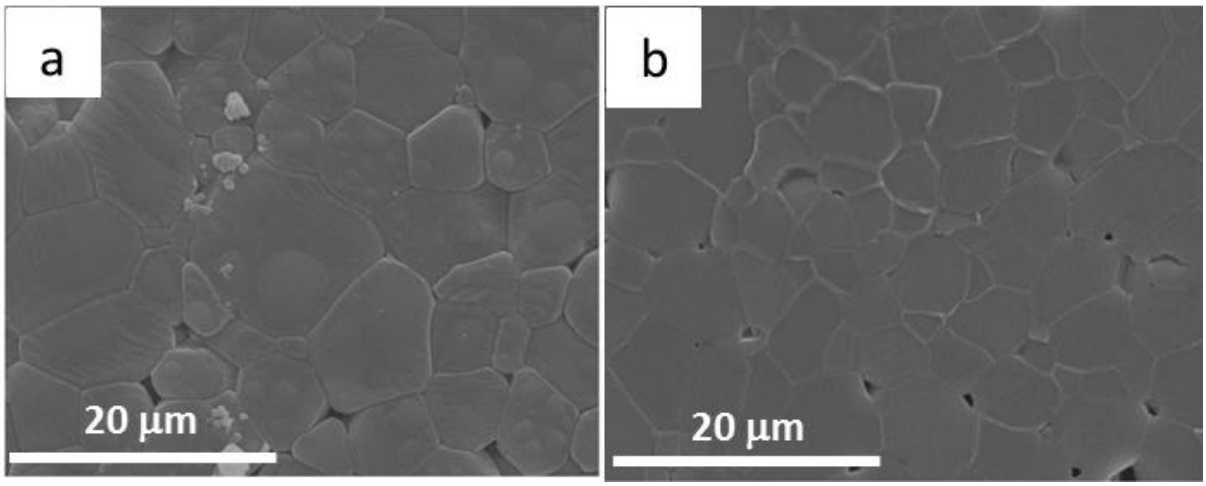

Fig. 4.8 SEM images of the thermally etched surface of: (a) Al_2O_3, and (b) $S_{0.5\text{-}1}$.

The grain refinment effect in Al_2O_3-GNT nanocomposites was evidenced by the laminated structures observed in the fracture surfaces of $S_{0.5\text{-}1}$ (Fig. 4.7c). It is well-documented that the finer grains can lead to improved hardness and strength of the composites, due to the grain boundary pining effect which impeded the dislocation movements[189]. However, the grain refinment is obviously not the only effect observed in this context for the GNT addition in the nanocomposites. In Fig. 4.6a-f, the fracture was found to change from inter-granular mode to trans-granular mode, and this is an indication of grain boundary strengthing[57].

4.3.2 SPS processing

SPS involves the simultaneous application of pressure and heat to a powder system, similar to the HP, with the primary difference lying in the way the sample being heated. In the SPS, an electrical current flows through the graphite punches and die, so that the pressing tool acts as the heating element by the Joule effect. Therefore, the heating rate can reach up to 1000 °C/min, against 20 °C/min for HP, which is the main difference between HP and SPS.

4.3.2.1 SPS Sintering Profile

Fig. 4.9 shows the profiles of the shrinkage rate (blue line), sintering temperature (red line), applied pressure (black line) and the average relative piston travel (green line) for pure Al_2O_3, during one SPS run. Similar to the sintering profile of HPed pure Al_2O_3, two shrinkage rate peaks were observed, the blue line. Akin to the HP, the peak at ~1100 ^oC in the green line is from the gamma to alpha phase transformation. The second peak at ~1300 ^oC corresponds to the densification of the Al_2O_3. However, the intensity of the peaks for the HPed pure Al_2O_3 are lower than those for SPS processing (Fig 4.3), demonstrating a slower shrinkage speed during the phase transformation stage and the densification stage for HP processing, due to its slower heating rate than SPS. The height of the first peak in the shrinkage rate profile is about twice of that of the second peak, whilst its width is slightly narrower. The height difference shows that the shrinkage speed at the phase transformation stage is much faster than that at the densification stage, for SPS.

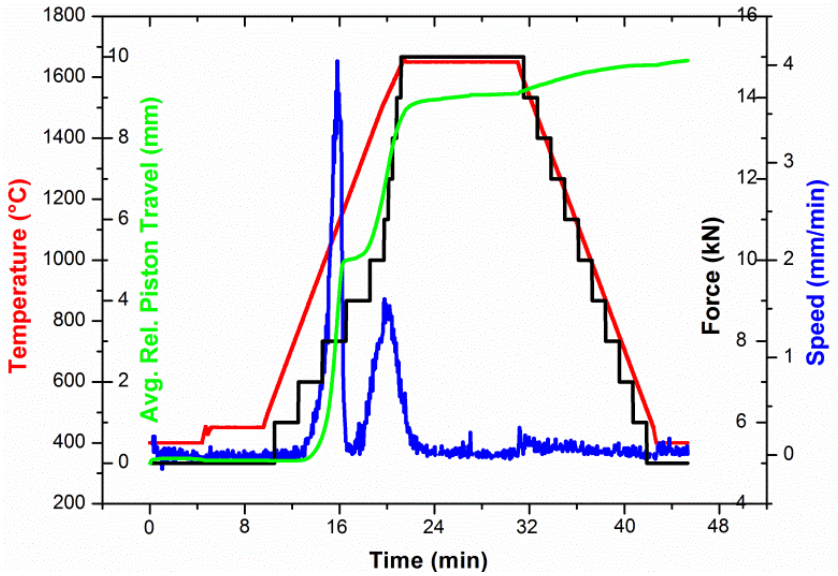

Fig. 4.9 The SPS profiles for pure Al_2O_3: the volume shrinkage rate (blue line), temperature profile (red line), pressure profile (black line), and the average relative piston travel (green line).

4.3.2.2 The effect of sintering temperature and GNT contents on density

The relative densities of the pure Al_2O_3 samples produced by SPS increased with increasing the sintering temperatures, and remained almost constant at 1650 °C, similar to our previous HP results[138]. Thus, 1650 °C was used in all later experiments since it produced the highest relative density. The grain size was larger in the pure Al_2O_3 and Al_2O_3-GNT nanocomposites prepared by SPS, compared with samples sintered by HP. The effect of sintering method on grain size will be studied in detail in section 4.3.2.3.

Table 4.2 The sintering conditions and relative densities of various nanocomposites.

Sintering method	Sample ID	GNP (wt%)	CNT (wt%)	Temperature (°C)	Pressure (MPa)	Dwelling time (min)	Heating rate (°C/min)	Relative density (%)
Spark plasma sintering	$S_{0\text{-}0}$	0	0	1400	40	15	100	95.5
	$S_{0\text{-}0}$	0	0	1500	40	10	100	96
	$S_{0\text{-}0}$	0	0	1650	40	10	100	98
	$S_{0.5\text{-}0.5}$	0.5	0.5	1650	40	10	100	99
	$S_{0.5\text{-}1}$	0.5	1	1650	40	10	100	99
	$S_{0.3\text{-}1}$	0.3	1	1650	40	10	100	99
	$S_{1\text{-}1}$	1	1	1650	40	10	100	98
	$S_{0.5\text{-}2}$	0.5	2	1650	40	10	100	97

4.3.2.3 Structural features

The XRD data of SPSed Al_2O_3-GNT nanocomposites all show the typical peaks of α-Al_2O_3, without any detectable carbide phases neither, indicating no significant reactions between the GNTs and Al_2O_3 during sintering. With increased GNP/CNT ratios, an additional peak is observed at 26.3° which corresponds to the crystalline graphite. The composite containing 1 wt% GNPs ($S_{1\text{-}1}$) has a peak at 26.3°, whilst there is almost no significant graphitic peak in samples with less than 0.5 wt% GNPs, a phenomenon similar to the HPed samples.

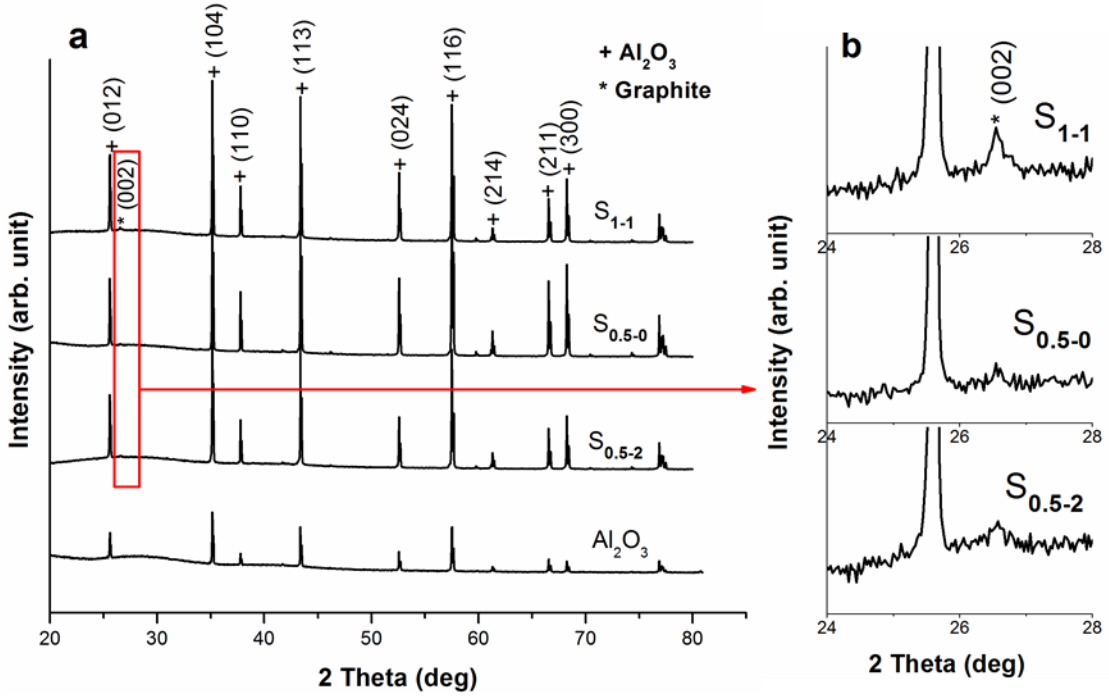

Fig. 4 10 (a) XRD profiles of the monolithic Al_2O_3 and Al_2O_3-GNT nanocomposites with different GNP/CNT contents sintered with SPS, and (b) the zoomed sections of samples $S_{1\text{-}1}$, $S_{0.5\text{-}0}$ and $S_{0.5\text{-}2}$.

The effect of sintering method on the microstructure of Al_2O_3-GNT nanocomposites

Fig. 4.11 shows the SEM images of fractured surfaces of the monolithic Al_2O_3 and Al_2O_3-GNT nanocomposites prepared using HP (left) and SPS (right). For the pure Al_2O_3 surfaces (Fig. 4.11a and b), the HP sample exhibits a fully inter-granular fracture mode; whilst the SPS sample shows a mixture of inter- and trans-granular fracture mode.

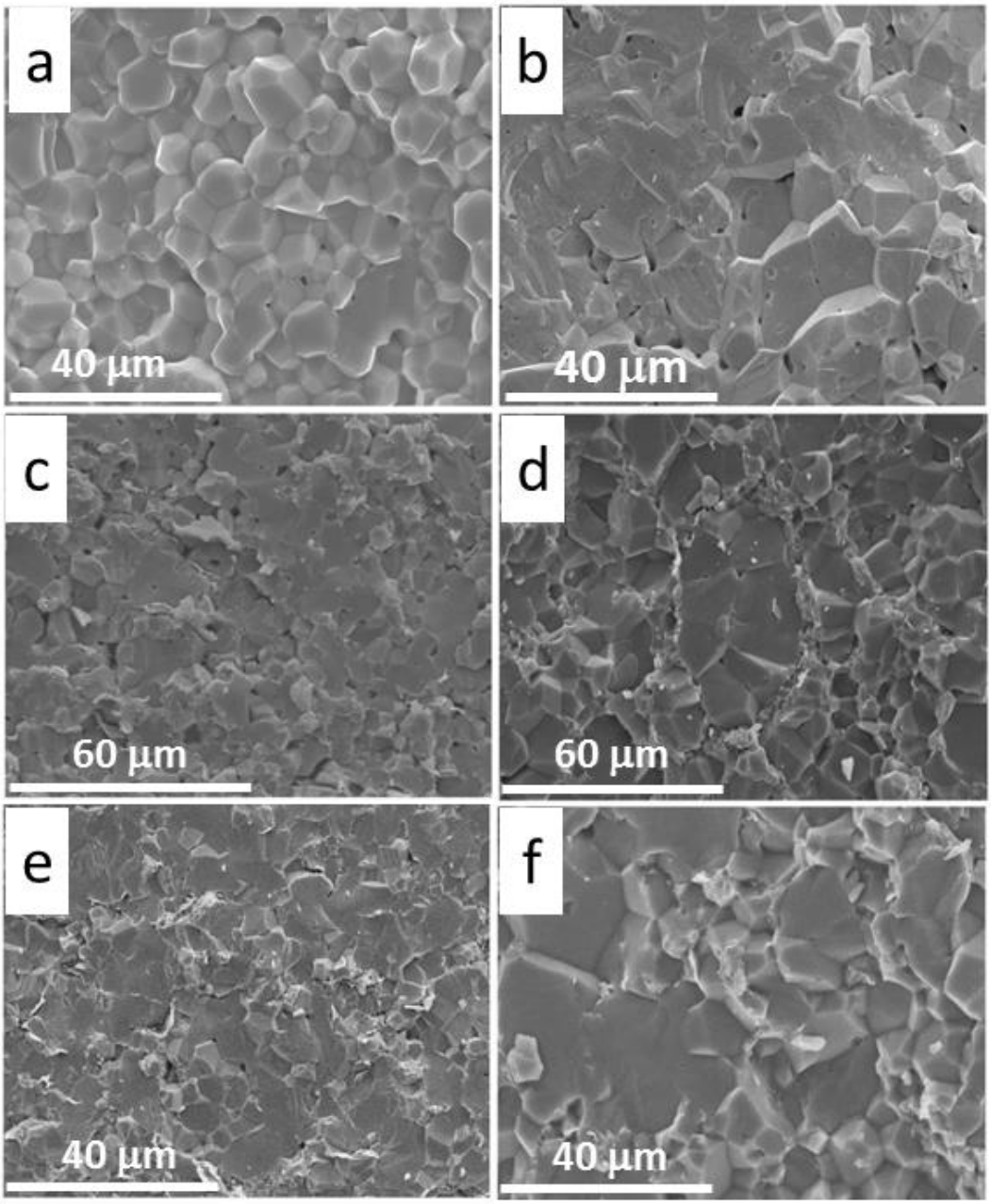

Fig. 4.11 SEM images of fractured surfaces of different materials. Monolithic Al_2O_3 prepared using HP (a) and SPS (b); $S_{0.5-0.5}$ by HP (c) and SPS (d); and $S_{0.5-1}$ from HP (e) and SPS (f).

The Al_2O_3-GNT samples prepared by SPS exhibited some inhomogeneous microstructures (Fig. 4.11d and f), with exaggerate growth grains surrounded by smaller grains; whereas a finer and more homogeneous grain distribution was visible for the HP samples, with a dominately high percentage of trans-granular fracture mode, as shown in Fig. 4.11c and e.

Fig. 4.12 shows SEM images of the thermally etched samples. Fig. 4.12a and b show the surfaces of pure Al_2O_3 sintered using HP and SPS, respectively. For identical

starting materials sintered at the same temperatures, the SPSed Al_2O_3 sample have larger grains than the HP samples, and a similar trend also occurred for the Al_2O_3-GNT nanocomposites. As shown in Fig. 4.12c and d, the grain size of SPS $S_{0.5\text{-}1}$ is much larger than that of the HP $S_{0.5\text{-}1}$.

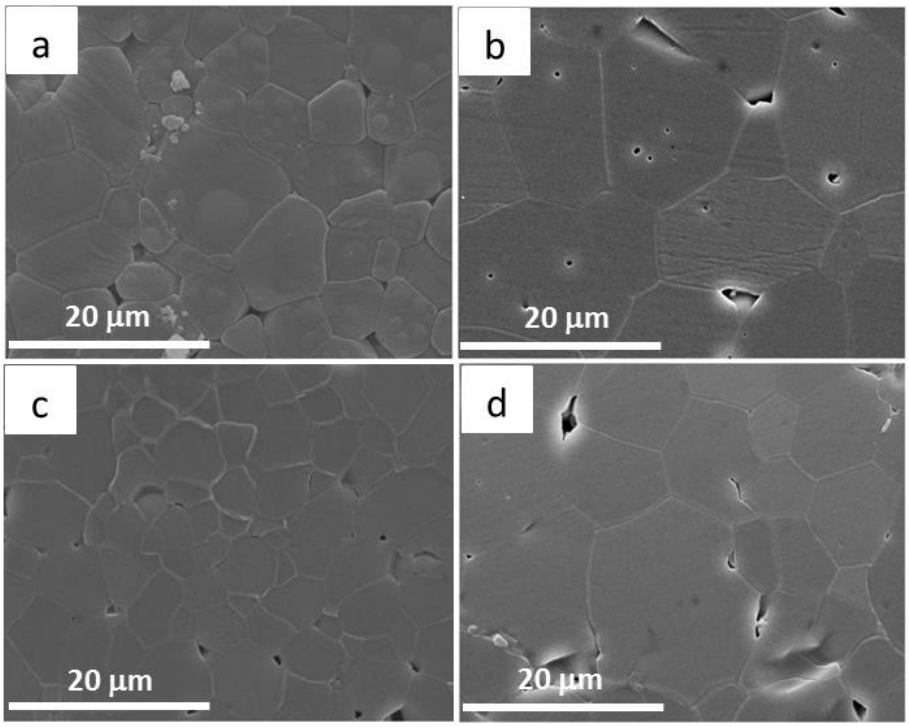

Fig. 4.12 SEM images of thermally etched surfaces revealing the grain sizes. Pure Al_2O_3 synthesized by (a) HP, and (b) SPS; $S_{0.5\text{-}1}$ synthesized by (a) HP and (d) SPS.

To understand the reasons behind the current differences in samples, it is necessary to understand how the SPS and HP worked during the sintering processes. As discussed earlier, the primary difference lies in how the thermal energy is transferred to the powder pellet. In SPS, the electrical current flows through the graphite punches and die to reach a rapid heating rate, and in contrast, the HP is through a slow radiation/convection, i.e. ~1000 °C/min *vs* 20 °C/min. Fast heating saves time and importantly energy[108], however it may yield low density and inhomogeneous microstructures, sometimes resulting in large grain sizes[109,110]. In our case, before the sintering shrinkage peak there was a phase transformation peak at 1100 °C (Fig. 4.9). As for HP, such a phase transformation peak would not appear if the starting powder was alpha Al_2O_3, as reported by Porwal et al.[84]. Meanwhile, the very rapid heating rate leaves little time for the powders to achieve a uniform temperature distribution, therefore resulting in a non-uniform and large localised temperature gradient. The non-

uniform temperature could exert regional overheating, thus resulting in rapid grain growth and larger grain sizes.

It has been reported in many studies that at high sintering temperatures, significant grain growth occurred regardless of the heating rates in SPS densified ceramics[106,190]. Under the same sintering temperature of 1650 °C, the observed grain size differences seem to suggest that the grain growth kinetics was affected by the heating rate, as this is the main difference between the HP and SPS processes here. High defect concentration during rapid heating has been reported as one of the main reasons behind fast grain growth, and can result in larger grains[105,191]. Another possibility might be the accuracy of the temperatures measured during the SPS procedure. Due to the rapid heating rate, the microscopic temperature differences between the centre and the edge of the graphite die could reach as much as 150 °C at 1300 °C[190], and practically some regions of the sample could be over-heated during the SPS process. Such inhomogeneous heat distribution can cause inhomogeneous sintering and microstructures, as observed in Fig. 4.11d and f. Uneven heat distribution is more dominant in the sintering of electrically insulating materials like Al_2O_3 than in conductive materials such as SiC using SPS, as the heat is transferred from the electrically conductive discs. Additionally, adding electrically conductive carbon nanostructures to the Al_2O_3-GNT composites could modify the local conductivity in regions, hence changed the heat distribution and therefore microstructures during SPS. As shown in Fig. 4.13a, the microstructure is uneven with large Al_2O_3 grains in $S_{0.5\text{-}0}$, whereas for $S_{0.5\text{-}0.5}$ smaller grains appeared in some localized areas (Fig. 4.13b). For $S_{0.3\text{-}1}$ and $S_{0.5\text{-}1}$ with more CNT contents, a significantly improved microstructural homogeneity and smaller grains are resulted, due to the better dispersion of carbon materials in the matrix at these contents, Fig. 4.13c and d. Therefore, it seems that the microstructures of SPS is more sensitive to the GNT distribution than that of HP, and unevenly distributed GNTs could lead to localised overheating and inhomogeneous grain growth.

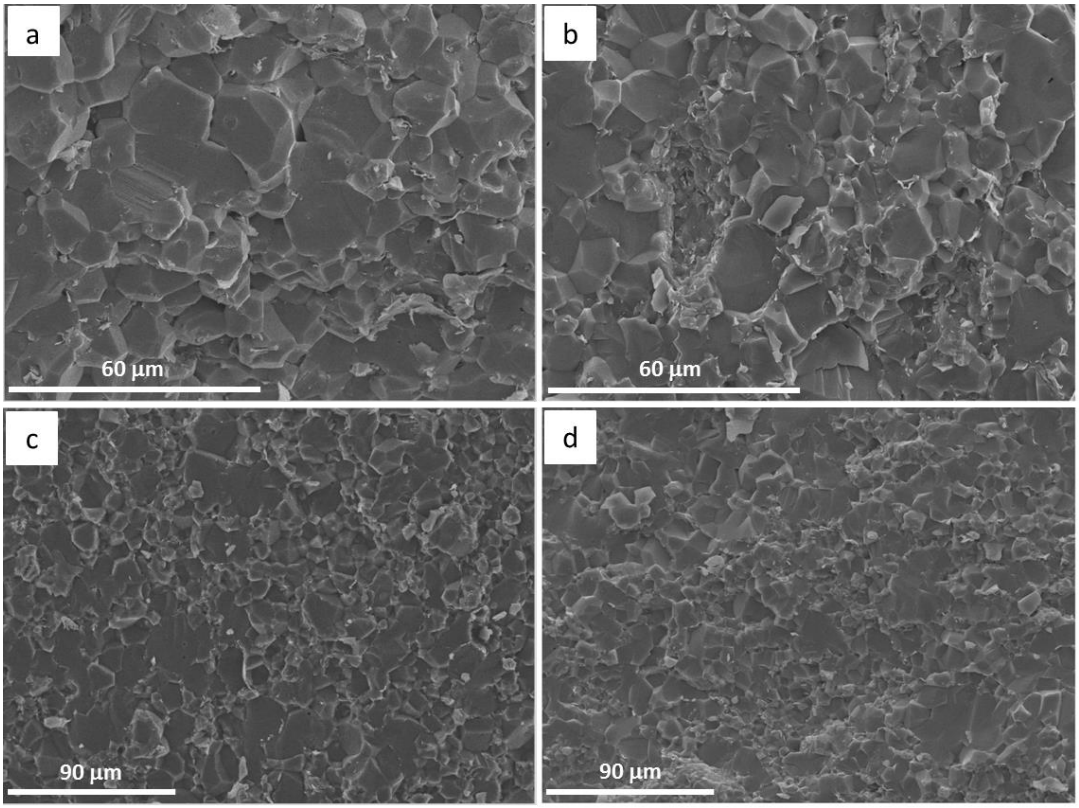

Fig. 4.13 SEM images of fractured surfaces of Al_2O_3-GNT composites prepared by SPS with various GNT contents. (a): $S_{0.5\text{-}0}$, (b): $S_{0.5\text{-}0.5}$, (c) $S_{0.3\text{-}1}$ and (d): $S_{0.5\text{-}1}$.

Proper selection/optimisation of key SPS parameters, including the heating rate, sintering temperature and dwell time, can control the final density and grain size of Al_2O_3. Particularly at lower sintering temperatures (T <1200 °C), densification is favoured by low heating rates and longer dwell times with no exaggerated grain growth; whereas at high sintering temperatures (T >1300 °C), a significant grain growth occurs with decreasing the heating rate and increasing the dwell time [190,192].

4.3.2.4 Interface study

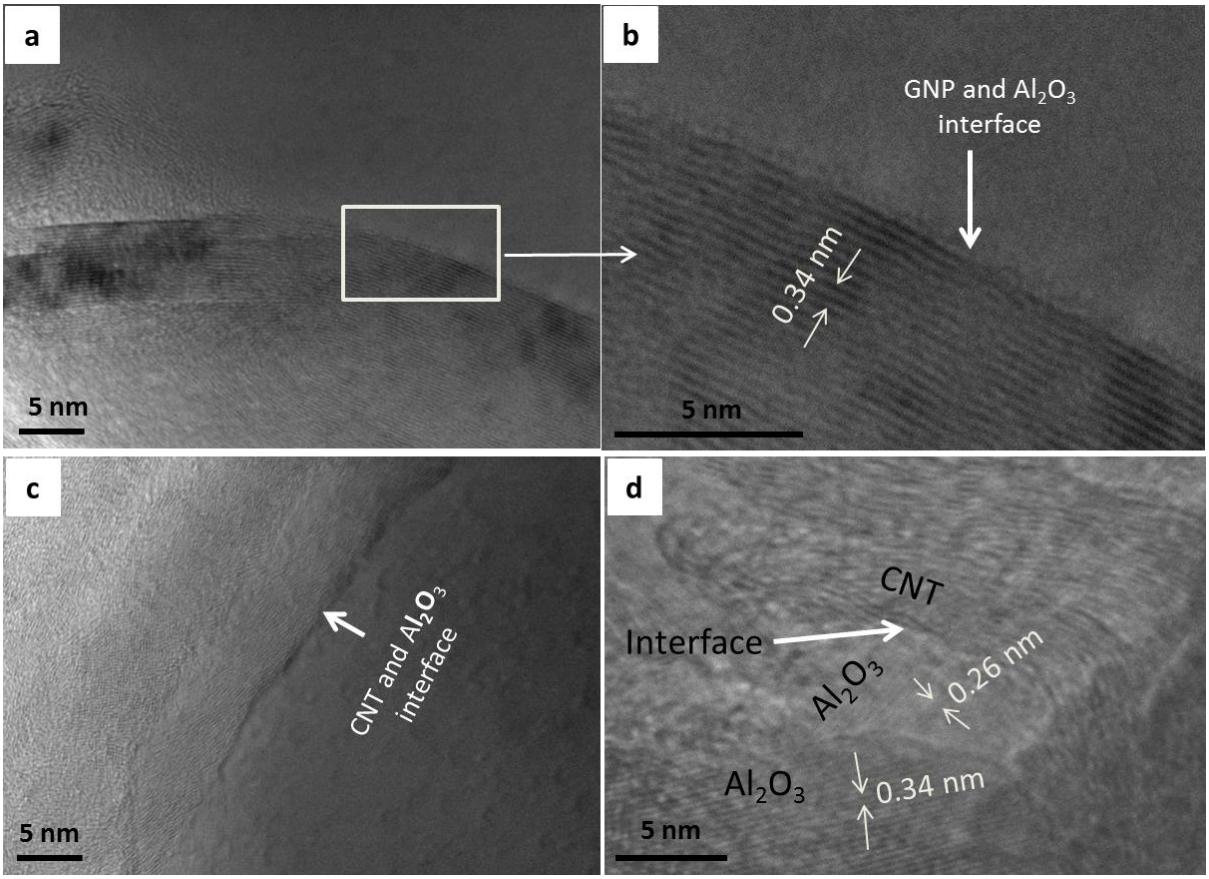

Fig. 4.14 (a) High-resolution TEM image from Al_2O_3-GNP nanocomposite showing; (b) Al_2O_3-GNP interface, (c) Al_2O_3-CNT interface and (d) Al_2O_3 interfaces with both GNP and CNT.

A strong interfacial connection of the reinforcement with the matrix is one of the important factors for achieving high mechanical properties for composites. In this thesis, we used the high-resolution TEM to visualise the interface structures. Fig. 4.14a shows high-resolution TEM images from the Al_2O_3-GNP nanocomposites. The large white arrows in Fig. 4.14b shows a GNP firmly attached to the matrix, and the clear interface without any intermediate phase between them can be seen. Fig. 4.14c displays a firm attachment of CNT into the Al_2O_3 matrix, and Fig. 4.14d depicts three distinct areas surrounding the interface region. The Al_2O_3 matrix can be identified by its fringe spacing of 0.26 nm and 0.34 nm, corresponding to the (104) and (012) planes, respectively. Based on the curvature and bending features, the CNT can also be identified, with a typical 0.34 nm fringe separation which corresponds to the (002) plane.

With such strong interfacial connections, the matrix holds the GNTs firmly and the intrinsically high elastic properties of GNTs become functional, leading to increased toughness for the composites and the loads can be transferred effectively from the matrix to GNT and vice versa. The improved mechanical properties obtained for Al_2O_3-GNP nanocomposite with optimized GNP/CNT ratio will be discussed later in chapter 5 and confirms the interface studies discussed in this section.

4.4 Conclusion:

Al_2O_3 ceramics reinforced by hybrid GNT nanoreinforcements were prepared *via* a combination of wet dispersion and probe sonication technique. By using SDS as the surfactant and by optimizing the sonication time, highly dispersed GNT suspensions were obtained during the mixing processes and high densities Al_2O_3 nanocomposites were synthesized by both SPS and HP, without any damage to the GNT reinforcements according to Raman studies. The CNTs attached to the GNP surfaces and edges during the mixing process helped their de-agglomeration and homogenous dispersion within the matrix. The fracture mode changed from inter-granular in the monolithic Al_2O_3 to a blurry and glaze-like trans-granular mode in the Al_2O_3-GNT composites at low GNT contents. Higher addition of GNTs at $S_{1\text{-}1}$ led to severer GNP and CNT agglomerations, with inhomogeneous microstructure due to difficulties in dispersion.

The HP and SPS processing techniques for the preparation of Al_2O_3-GNT nanocomposites with identical GNT contents under the same nominal sintering conditions were further compared. The grain sizes of the nanocomposites prepared using SPS were larger than for the nanocomposites prepared using HP and the microstructure is inhomogeneous in the SPSed samples compared to HPed composites. High defect concentrations originating from the phase transition during the rapid sintering or possibly overheating during the SPS processing are possible reasons for the regional grain size enlargements and microstructural inhomogeneity in the SPSed Al_2O_3-GNT nanocomposites. However only preliminary studies have been conducted for the SPS, and further conclusive research is needed in the future to optimize the SPS sintering condition. The combined GNTs effectively hindered the grain growth in both cases, and at low GNT contents, highly dense Al_2O_3-GNT nanocomposites were sintered, independent of the sintering techniques.

Chapter 5 Mechanical properties of Al_2O_3-GNT nanocomposites

5.1 Introduction

The concept of GNP/CNT hybrid reinforcement has recently been pioneered in polymer-based composites, which has resulted in the toughest and strongest man-made polymer nanocomposite ropes[37-41]. It is expected that the 2D structures of GNPs will uniquely provide much higher interfacial interactions between the filler and matrix, which cannot be achieved by using any 0-D nanoparticles or 1-D CNTs as the filler independently. In this chapter, the effects of various GNP/CNT (namely GNT) additions on the mechanical properties, in particular the fracture toughness, will be presented and discussed in section 5.2. The fracture toughness (K_{IC}) was evaluated using the SENB method which is considered as the most reliable technique for CMCs. The effects of HP and SPS processing on the mechanical behaviour of the GNT-reinforced Al_2O_3 nanocomposites will be comprehensively studied in section 5.3. The main aim is to understand the effects of the hybrid reinforcement on the CMCs and to assess whether or not the Al_2O_3-GNT nanocomposites are promising candidates for advanced applications.

5.2 Mechanical properties of Al_2O_3-GNT nanocomposites prepared by HP

5.2.1 Hardness

Fig. 5.1 displays the hardness values *vs* the GNT contents of the composites. Compared with the plain Al_2O_3 with a hardness value of 16 GPa, the nanocomposites exhibited a marginal increase by 6% and peaked at low GNT content in $S_{0.5\text{-}1}$ up to 17 GPa. From $S_{0.5\text{-}1}$ to $S_{0.5\text{-}2}$ which contains 1 wt% more CNTs, the hardness sharply decreased by 28%, down to 12 GPa, and further reduction occurred with increased the amounts of GNP of more than 0.5 wt%.

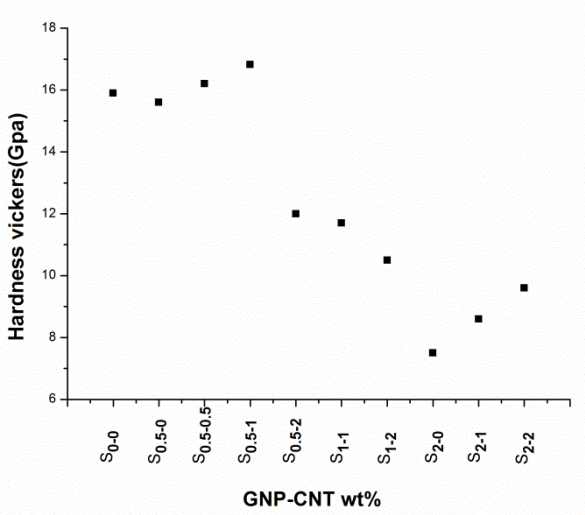

Fig. 5.1 Vickers hardness values of the Al_2O_3–GNT nanocomposites at different GNP-CNT ratios.

In order to find out the exact influence of GNPs and CNTs on hardness, we redrew the hardness results in Fig. 5.1 and obtained Fig. 5.2. By comparing Fig. 5.2a and b, it is shown that samples containing a fixed 2 wt% GNPs exhibited lower values at all CNT contents than those containing a fixed 2 wt% CNTs. Therefore, the increase of GNPs seems to have a stronger negative effect on the hardness than that of CNTs in the nanocomposites.

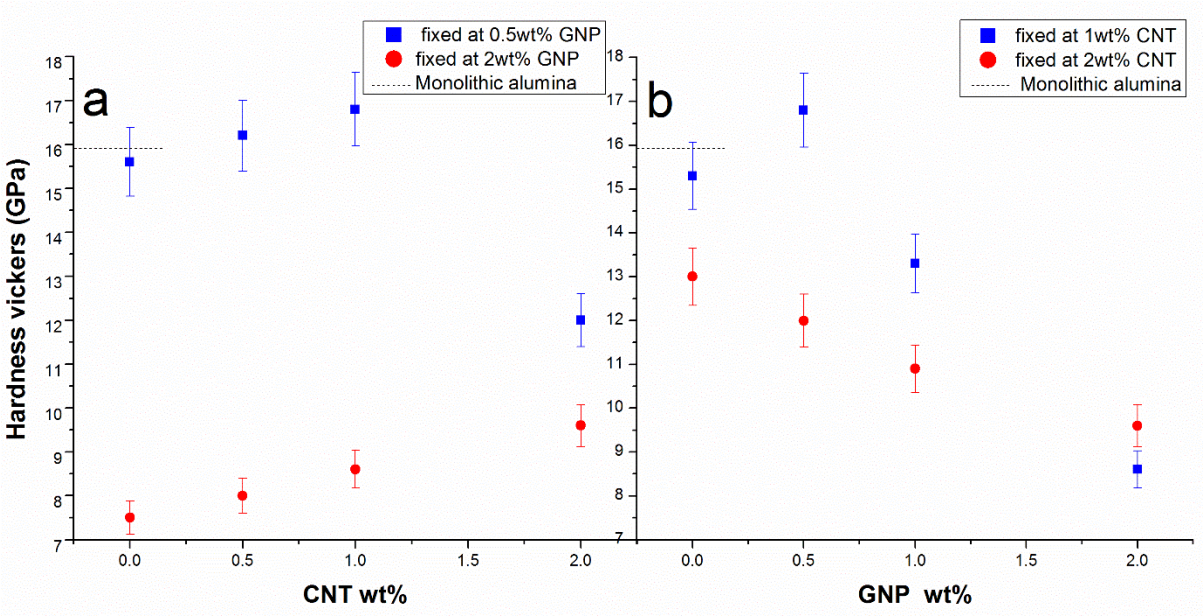

Fig. 5.2 Hardness as a function of reinforcement contents. (a) Fixed GNP wt%, and (b) Fixed CNT wt%.

5.2.2 Fracture toughness and flexural strength of Al_2O_3–GNT nanocomposites

Fig. 5.3 shows the fracture toughness and flexural strength of the Al_2O_3–GNT nanocomposites at various GNP/CNT ratios. A 63% and 12% increase in the fracture toughness and flexural strength has been achieved in sample $S_{0.5\text{-}1}$, compared with the monolithic Al_2O_3, reaching 5.7 MPa·$m^{1/2}$ and 424 MPa respectively. Fig. 5.3 also shows that at different GNP and CNT combinations, samples $S_{0.5\text{-}1}$ with the optimally combined additions of 0.5 wt% GNPs and 1 wt% CNTs, produced the highest fracture toughness and flexural strength. For samples $S_{0.5\text{-}1}$ to $S_{1\text{-}1}$, only a 0.5 wt% increase in the GNP contents, the fracture toughness and flexural strength decreased by 38% and 35% respectively, which are much larger than their respective reductions from $S_{0.5\text{-}1}$ to $S_{0.5\text{-}2}$. With 1 wt% increase in CNTs in samples $S_{0.5\text{-}2}$, only a 26% and 6% reduction was recorded in these properties. Thereby, similar to the influence on the hardness, the GNPs seem to have much complicated effects than the CNTs in the fracture toughness and flexural strength of nanocomposites. This will be further discussed in section 5.2.3.

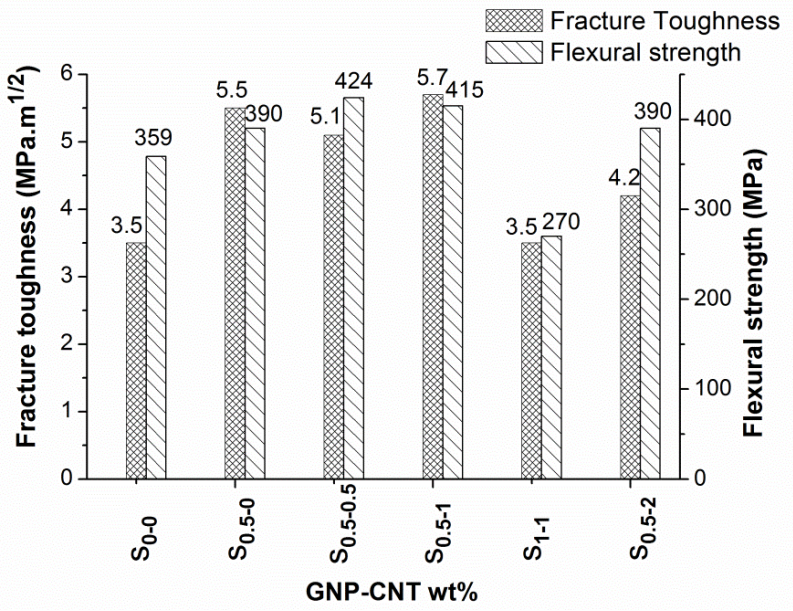

Fig. 5.3 Fracture toughness and flexural strength of the GNT-Al_2O_3 nanocomposites at different GNP/CNT ratios.

The previously reported Al_2O_3-CNT nanocomposites prepared by Ahmad et al. have reached a 94% improvement in the fracture toughness over the monolithic Al_2O_3[57]. Compared with our optimized sample ($S_{0.5\text{-}1}$), the difference in fracture toughness could be due to the different notch dimensions that were applied in samples for the SEND specimens, as small variations in notch dimension can lead to considerable changes in the fracture toughness[193]. However, in terms of flexural strength, Fig. 5.3 also shows that a relatively large improvement has been obtained in this context, a 15% improvement over monolithic Al_2O_3 in sample $S_{0.5\text{-}0.5}$, against a 6.4% improvement reported earlier in the CNT-reinforced composites[57].

Indeed, the higher fracture toughness values obtained in this study are believed to be due to the improved dispersion of GNTs with the matrix and the increased contact areas between GNT and the Al_2O_3 matrix, which were achieved by adopting combined strategies during the mixing process. Firstly, allocating two weeks incubation time to the CNT suspension allowed the surfactant to be thoroughly adsorbed on the CNT surfaces, which led to a better dispersion in the Al_2O_3 matrix, as described in the previous work[57]. Secondly, using both CNTs and GNPs as hybrid agents led to a better dispersion owning to their synergistic effect[37]. Ultrasonic treatment during the mixing process was another factor to improve the GNTs and Al_2O_3 nanoparticles dispersion during the mixing. This allowed for more Al_2O_3 nanoparticles available to sandwiching with the GNTs in the suspension, thereby more GNTs could be incorporated within the ceramic powder without severe re-agglomeration.

After examining different GNP-CNT combinations, we have also found out that the GNP contents exhibited a much severe influence than that of CNTs on the hardness, flexural strength and fracture toughness. This is possibly due to the agglomeration of GNPs in samples. At >0.5 wt%, GNPs may be over-lapped to form larger platelets of >200 nm thick, which could easily slide against each other and debound under stresses, as evident in Fig. 5.4. Therefore, sliding thick GNP layers against each other is one of the possible reasons for the aggressive negative effects in hardness and other mechanical properties for samples having more GNP contents than our optimized sample ($S_{0.5\text{-}1}$), as discussed in Figs. 5.1 and 5.3. In contrast, CNTs are much smaller and have less contact areas with the grains compared with large GNP agglomerates, therefore, as evident in Fig. 5.3, $S_{0.5\text{-}2}$ with 1 wt% additional CNT

content compared with $S_{0.5\text{-}1}$ exhibiting less negative effect in the fracture toughness and flexural strength than $S_{1\text{-}1}$ with only 0.5 wt% extra GNP content against $S_{0.5\text{-}1}$. However, in Fig. 5.4, the crack ended up with smaller sheets of GNP (white arrow), opposite to the larger GNP flakes, which is an interesting feature observed for GNPs to prevent the crack propagation.

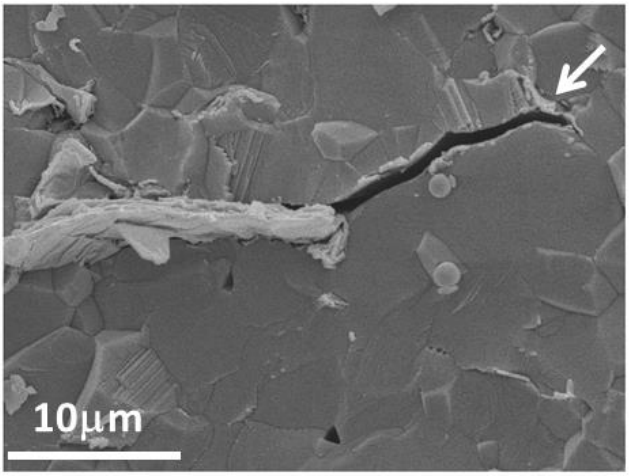

Fig. 5.4 SEM image showing the deboning of over-lapped GNPs around grain boundaries.

5.2.3 Toughening mechanisms for Al_2O_3-GNT nanocomposites prepared by HP

To investigate the reasons behind the mechanical property improvements, further studies were carried out using SEM to examine the microstructures of fractured surfaces. The CNT and GNP dispersion characteristics after sintering were also studied. Fig. 5.5 shows the SEM images of the freshly fractured surfaces of samples $S_{0.5\text{-}0}$, $S_{0.5\text{-}0.5}$ and $S_{0.5\text{-}1}$, respectively. It is found that conventional toughening mechanisms derived for fiber-reinforced composites are also applicable to our Al_2O_3-GNT nanocomposites. CNTs and GNPs pull-out and bridging phenomena are visible in Fig. 5.5a and d, which are believed to have contributed to the effective improvement in the fracture toughness. In Fig. 5.5b, some CNTs are embedded on the GNP flake surfaces, which is another evidence for the strong synergetic effect between the GNPs and CNTs. The black arrow in the bottom of Fig. 5.5c shows that the large GNPs tend to roll around the grain boundaries. Entangled GNT network is also observable in Fig. 5.5d. This might be the reason behind the grain refinement effect in the nanocomposites as evidenced in Fig. 4.7. GNTs existing around the grain boundaries can effectively prevent the grain growth during sintering by reducing the atomic

diffusion coefficient, hence constraining the grain growth. Additionally, CNTs can act as pinning points to stop the grain boundary movements under stresses. As shown by the black arrow in the top of Fig. 5.5c and d, CNTs embedded inside the grain indeed pinned the Al_2O_3 grains together and must have strengthened the grain boundaries. As a result, these CNT-strengthened grain boundaries led to the changed fracture mode, from the inter-granular in pure Al_2O_3 to trans-granular in the nanocomposites, as shown earlier in Fig. 4.5a and b. Primarily, the GNPs are more influencial to the former grain refinement, and the CNTs are more responsible for the interfacial strengthening.

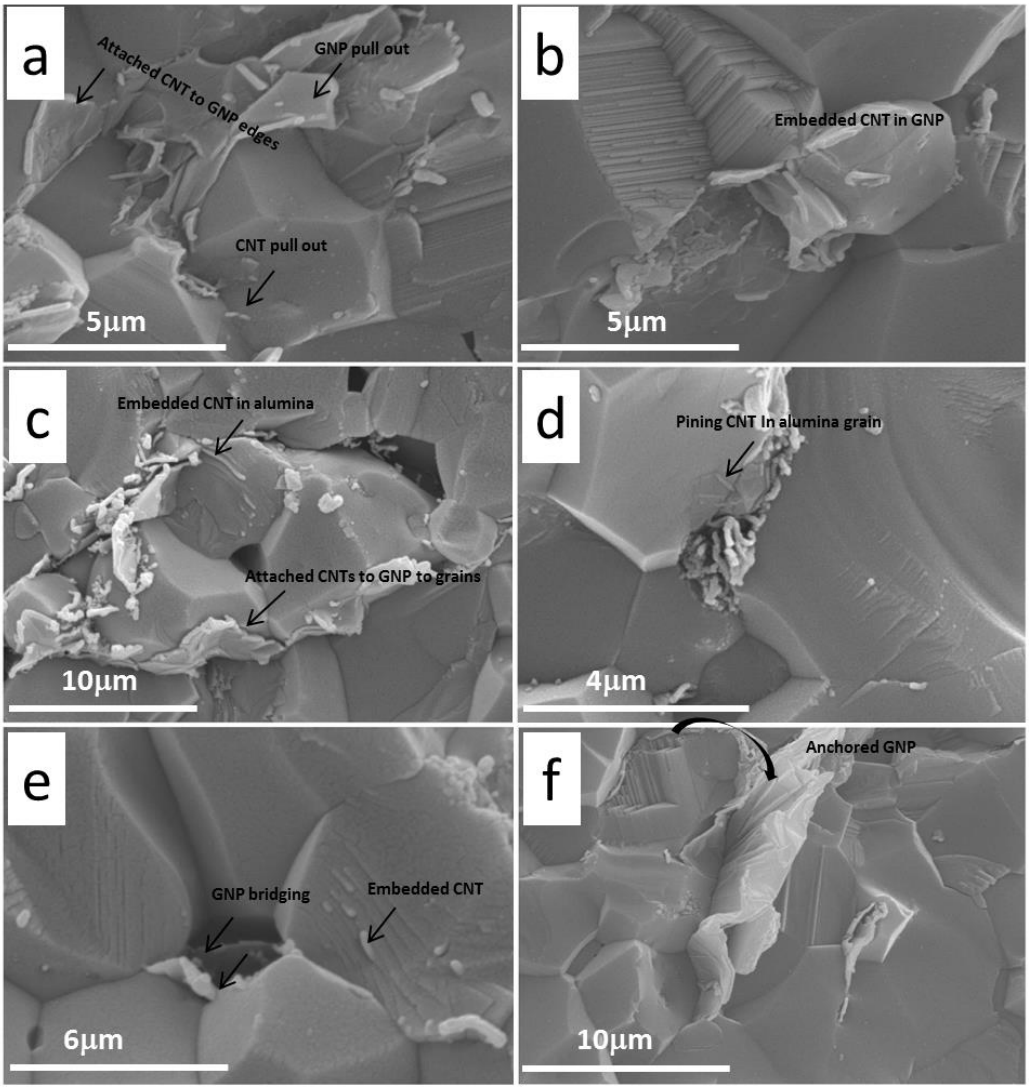

Fig. 5.5 SEM images of fractured surfaces of the Al_2O_3-GNT nanocomposites for samples: (a-b) $S_{0.5\text{-}1}$, (c-e) $S_{0.5\text{-}0.5}$, and (f) $S_{0.5\text{-}0}$.

Fig. 5.5f shows a large GNP securely rolled along the Al_2O_3 grains, due to its flexibility, forming a large area of anchoring interface with the matrix. Such anchoring can lead to increased interfacial frictions between the GNPs and the matrix during movement under stresses, and the required energy to pull-out such GNPs is expected to be higher than that for CNTs. Therefore, the fracture occurred through the Al_2O_3 grains rather than along the grain boundaries, as shown in Fig. 5.5f. This is an example of GNP anchoring reinforcement effect, a typical mechanism observed for large and flexible 2D GNPs[64].

These results mean that the CNTs and GNPs have played different roles in improving the fracture toughness, due to their different microstructures: GNPs increasing the required pull-out energy during fracture by anchoring around the Al_2O_3 grains and producing higher contact areas with grains; whilst CNTs bridging the grains due to their higher aspect ratio. The smaller diameter of CNTs allows them to be embedded within the grains during grain growth, and their elongated shape enables them to link various grains together to form bridges. It is believed that CNTs can be stretched much longer than GNPs before collapsing during crack propagation, thereby contributing more to the bridging effect. In fact, the elongated feature of CNTs under tension has been experimentally confirmed under in-situ TEM observation[194]. The sliding of their concentric cylinders allows them to extend significantly longer than their original length, without breaking. These roles of the GNPs and CNTs are complementary with each other at appropriate concentrations, i.e. ideally dispersed, allowing for absorbing more energy during crack propagations.

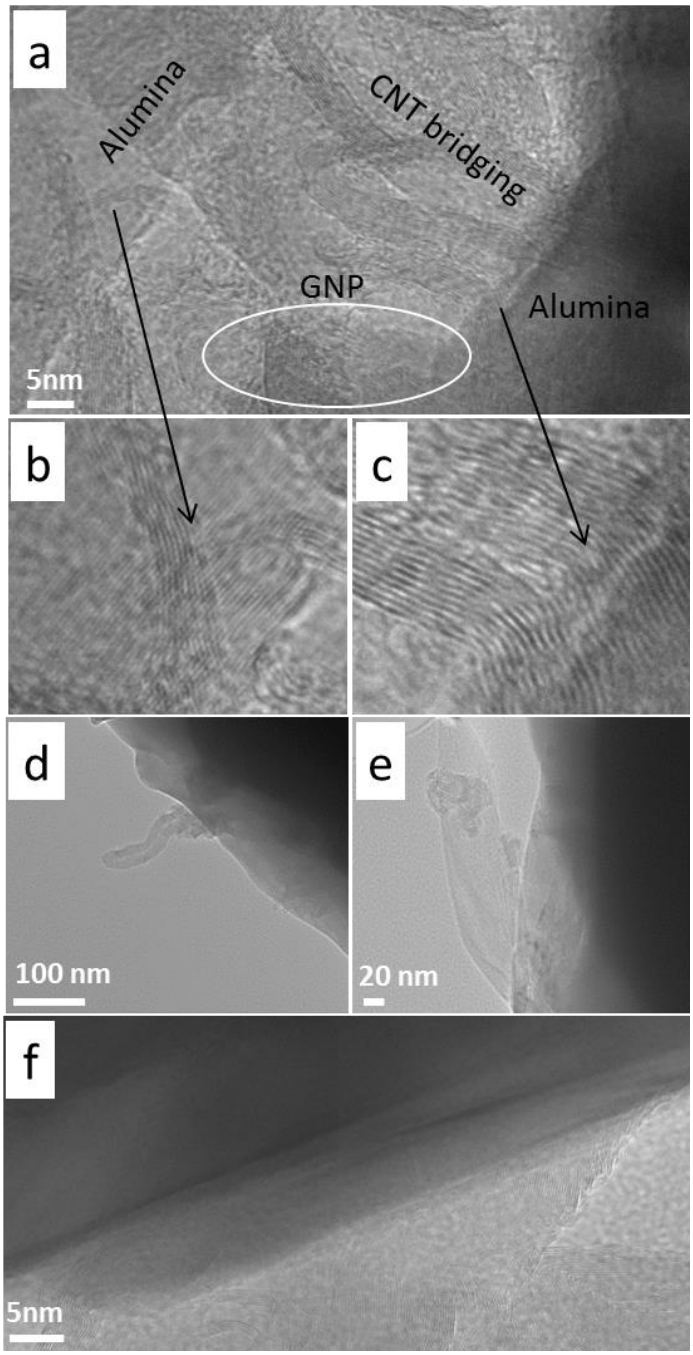

Fig. 5.6 TEM images of the Al_2O_3-GNT nanocomposite showing locations of the CNPs and CNTs (a); enlarged images from selected areas of Fig. 5.6a (b and c); the CNT and GNP pulled-out from the Al_2O_3 matrix (d and e); and the Al_2O_3-GNP interface (f). The darker area is the Al_2O_3 side and lighter area is the CNT side in (f).

Our TEM study (Fig. 5.6a-f) also confirmed the bridging and pull-out reinforcing mechanisms. Fig. 5.6a shows a CNT bridging across two Al_2O_3 grains, and Fig. 5.6d and e displays a CNT and a GNP being pulled-out from the Al_2O_3 grains, respectively. High resolution images from the selected area in Fig. 5.6a exhibits the existence of embedded CNTs on the GNP surfaces, in consistence with the SEM results shown in

Fig. 5.5b. This also demonstrates the excellent affinity between CNTs and GNPs as a hybrid reinforcement. In Fig. 5.6f, firmly attached CNTs and GNPs to the matrix are shown, indicating their strong interfacial connection with the matrix, thereby leading to increased toughness in the composites.

5.3 Comparing mechanical properties of samples prepared by HP and SPS

Fig. 5.7a-c shows a direct comparison of the Vickers hardness, fracture toughness and flexural strength of the pure Al_2O_3 and Al_2O_3-GNT nanocomposites prepared by the two processing routes, respectively. The hardness values and flexural strength of the Al_2O_3-GNT nanocomposites prepared by SPS were reduced compared with the HP-sintered samples. However, the fracture toughness of $S_{0.5\text{-}0.5}$ sintered using SPS reached 5.9 $MPa{\cdot}m^{1/2}$, showing a 15% increment compared with the HPed $S_{0.5\text{-}0.5}$ sample with a fracture toughness value of 5.1 $MPa{\cdot}m^{1/2}$. Similar to the fracture toughness, the better values of hardness and flexural strength for SPS samples have also shifted to lower GNT contents, and the maximum values occurred at $S_{0.5\text{-}0.5}$, when compared with the HP samples in which the highest mechanical properties appeared at $S_{0.5\text{-}1}$. This result is in the same line with microstructural comparisons between SPSed and HPed samples as disscussed in section 4.3.2.3. The microstructures of SPSed samples are more sensitive to the GNT distribution than that of HP because unevenly distributed GNTs could lead to localised overheating and inhomogeneous grain growth in SPSed nanocomposites. Therefore, as shown in Fig. 5.7, the improved mechanical properties in SPSed Al_2O_3-GNT nanocomposites were obtained in samples with lower GNT content compared with those HPed samples. However, the overall mechanical properties of the composites obtained from the two techniques are in line with each other for a given hybrid content, within the normal ±5% error range.

The overall variation in hardness, fracture toughness and flexural strength in the SPS densified nanocomposites compared with the HPed samples, according to Fig. 5a-c, is consistent with their different grain sizes (Fig. 4.11). The SPS processed materials showed an abnormal grain growth, and the large irregular grains deteriorated their mechanical properties slightly. According to Fig. 4.10c-f, the fracture mode in the SPSed nanocomposites was a mixture of inter-granular and trans-granular; whilst the

HP samples showed a fully trans-granular fracture mode. This is probably an indication of weaker grain boundaries in the SPSed composites than in the HPed samples.

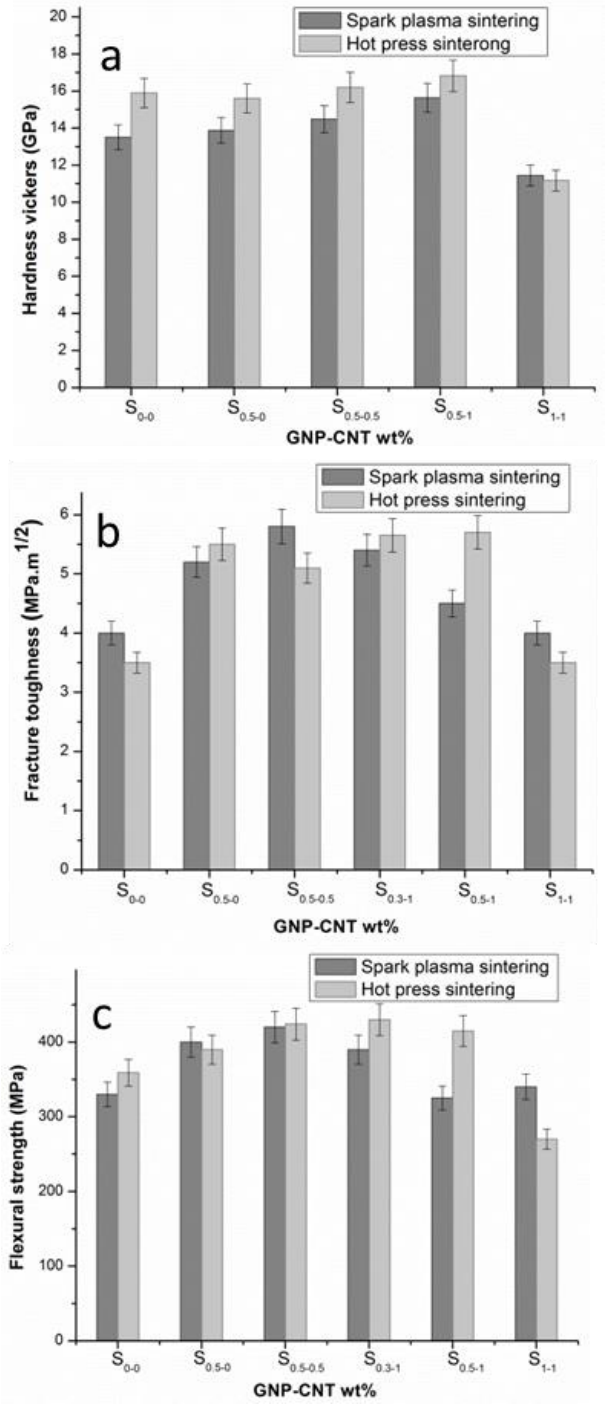

Fig. 5.7 (a) Vickers hardness, (b) fracture toughness, and (c) flexural strengh of pure Al_2O_3 and Al_2O_3-GNT nanocomposites with varous GNT contents prepared by HP and SPS.

Moreover, the highest mechanical properties in the SPS composites have been shifted to lower GNT contents (Fig. 5.7a-c), compared with the equivalent GNT contents for the HP samples. This is most likely related to that the reinforcement phases were

forced into the large grain boundaries owing to the fast grain growth during the SPS process, again due to the high heating rate and lack of sufficient time for better packing. Such inhomogeneous microstructure does not seem to appear in the HP samples, see Fig. 4.10 for comparison. However, the differences in the microstructures between the two types of composite samples did not produce any major differences in mechanical properties. Further detailed studies could provide a much clear idea about their exact effects on the microstructures and properties.

5.3.1 Toughening mechanisms of Al_2O_3-GNT nanocomposites prepared by SPS

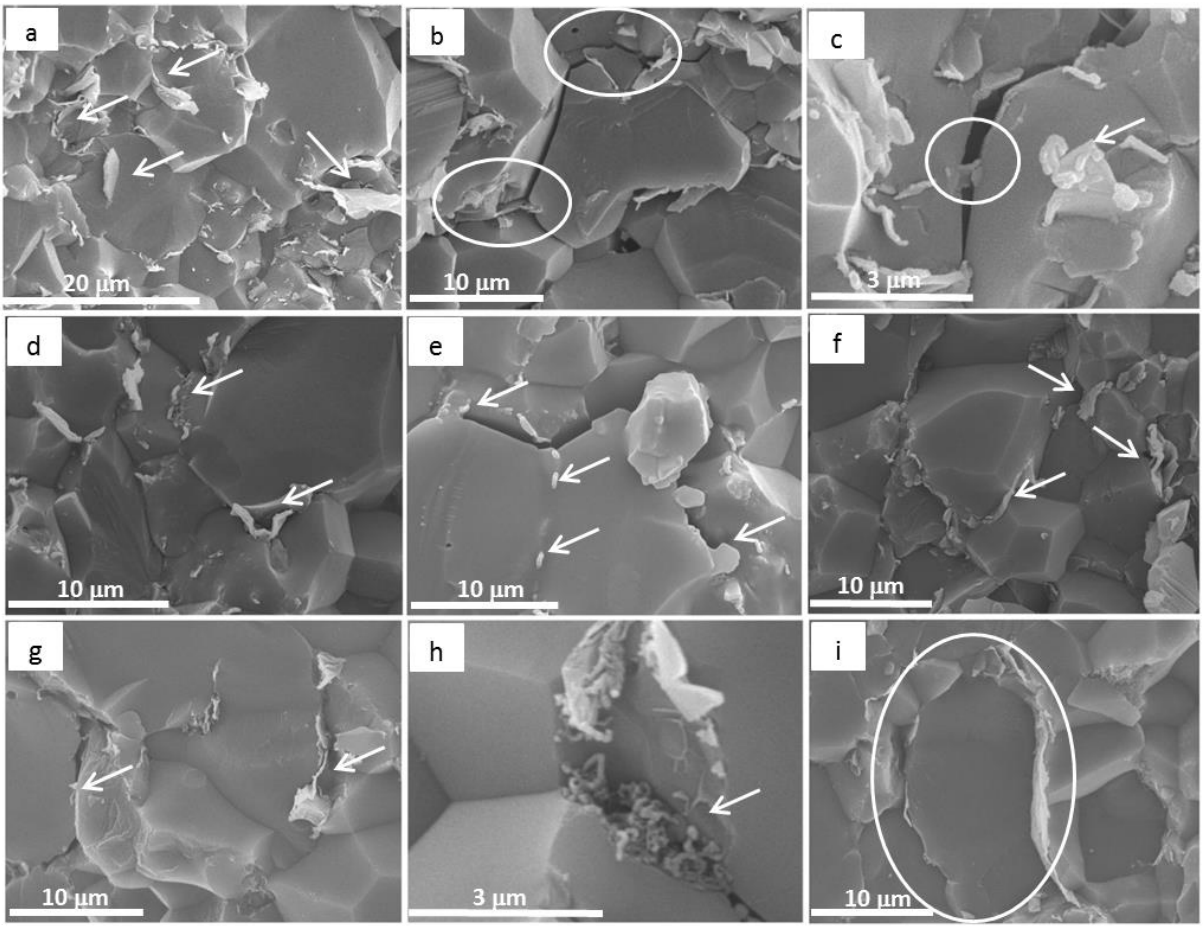

Fig. 5.8 SEM images of fractured surfaces of the SPS Al_2O_3-GNT nanocomposite samples: (a-c) $S_{0.5\text{-}0}$, (d-f) $S_{0.5\text{-}0.5}$, and (g-i) $S_{0.5\text{-}1}$.

Fig. 5.8 shows the fracture surfaces of $S_{0.5\text{-}0}$ (first row), $S_{0.5\text{-}0.5}$ (second row) and $S_{0.5\text{-}1}$ (third row) nanocomposites sintered using SPS. It is clear that both GNPs and CNTs remained undamaged during the HP and SPS consolidation processes.

GNPs play an important role in toughening by anchoring around the grains and by increasing the interfacial friction between the GNP and matrix. Such a mechanism increases the required energy for GNP pull-out, which leads to the trans-granular fracture mode in $S_{0.5\text{-}0}$ and $S_{0.5\text{-}1}$ (Figs. 5.8a and 5.8i). GNPs also stopped the crack from propagating (Fig. 5.8b and c, circled) by a bridging mechanism. Trapped GNPs inside the grains improved the toughness via the pull-out mechanism during fracture (Figs. 5.8a and c, arrowed). Embedded CNTs in Fig. 5.8d and e strengthened the grain boundaries and caused trans-granular fracture. However in $S_{0.5\text{-}0.5}$, the GNP bridge suppressed the crack propagation by both its ends (Fig. 5.8e, arrowed). Small CNT bundles between the grains (Fig. 5.8h) can also form a bridge between grains during crack propagation, on top of hindering the grain growth in the Al_2O_3-GNT nanocomposites. These features are similar to the HPed samples.

TEM images from the SPS sample of $S_{0.5\text{-}0.5}$ show the GNP pull-out and embeded CNT and GNP bridging (Fig. 5.9a-c), respectivly, which is in consistent with the phenomina that have been observed for the fractured sufaces during SEM study (Fig. 5.8). Firmly attached CNTs and GNPs to the Al_2O_3 grain in Figs. 5.9e and f indicate their strong interfacial connection with the matrix, thereby leading to an increased toughness in the composites.

The above results show that GNPs and CNTs also played different roles in toughening the nanocomposites in the SPSed samples, similar to those previously observed for HPed samples, therefore the hybrid reinforcements are independent of the sintering methods.

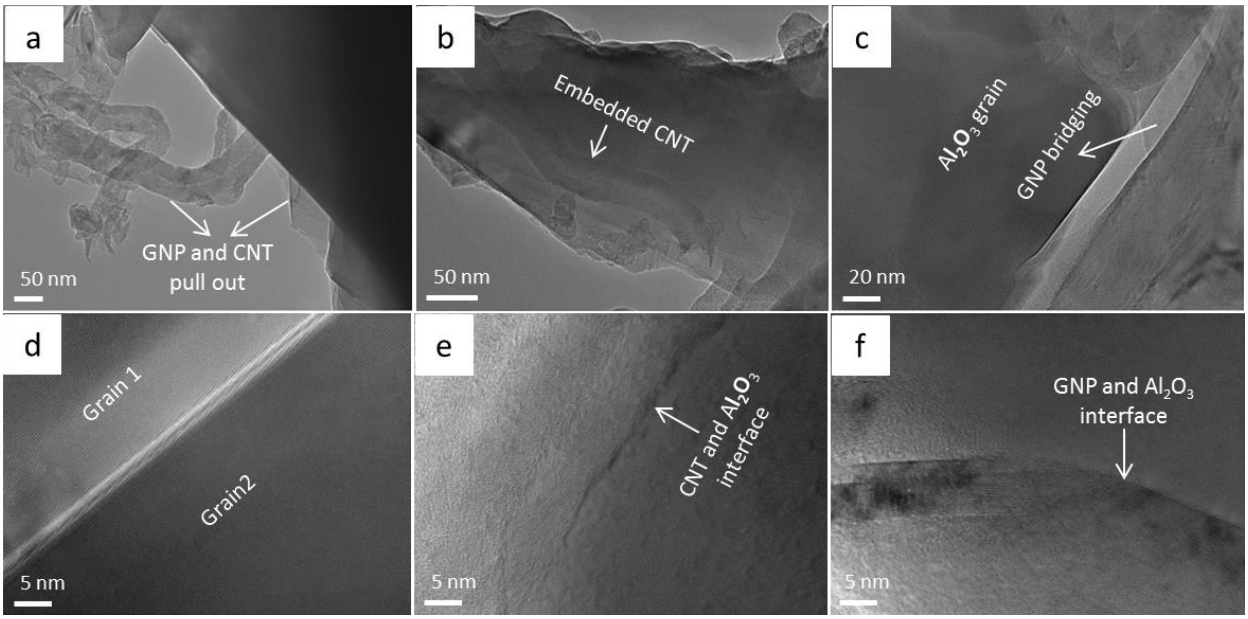

Fig. 5.9 TEM images from $S_{0.5\text{-}0.5}$ prepared by SPS

5.4 Conclusion

The mechanical properties of as-prepared Al_2O_3 ceramics reinforced by the hybrid GNT reinforcements were investigated. Various GNP/CNT ratios have been assessed to obtain optimum condition in terms of hardness, fracture toughness and flexural strength. At lower GNT additions ($S_{0.5\text{-}1}$), high performance HPed Al_2O_3 nanocomposites with 6%, 63% and 12% improvement in hardness, fracture toughness and flexural strength were obtained respectively, against pure Al_2O_3. Based on SEM and TEM observations, the GNT reinforcements remained undamaged in nanocomposites after HP. At higher additions, GNPs exhibited much severer negative effect than the CNTs on the mechanical properties. Microstructural investigations showed that GNPs contributed more to the grain refinements and the CNTs contributed more to improve the interfacial strengths. Meanwhile, the GNPs were primarily increased the pull-out energy by anchoring around the grains due to their 2D flexible microstructural feature; whilst CNTs were found to bridging the grains and pinning the grain boundary movements, thereby complementarily improved the fracture toughness and flexural strength of the composites, reaching 5.7 $MPa \cdot m^{1/2}$ and 424 MPa respectively.

We have investigated the influences of both the HP sintering and SPS processing techniques, under the same nominal sintering conditions, on the Al_2O_3-GNT nanocomposites with identical GNT contents. Although there were differences in the microstructures of Al_2O_3-GNT nanocomposites prepared by SPS compared with HP in terms of grain size, fracture mode and microstructural homogeneity (section 4.3.2.3), the overall mechanical properties of the samples sintered by the two techniques do not show any major differences. Only the peak mechanical properties for SPS prepared nanocomposites shifted to lower GNT content samples ($S_{0.5\text{-}0.5}$), possibly due to that the SPSed nanocomposites are more sensitive to GNT content and dispersion, whereas the HP samples they peaked at $S_{0.5\text{-}1}$. However, the combined GNTs effectively hindered the grain growth in both cases, and reinforced the Al_2O_3 via various mechanisms, independent of the sintering techniques.

Chapter 6 Tribological properties of Al_2O_3-GNT nanocomposites

6.1 Introduction

The friction and wear behaviour of CMCs is of great importance for contact-mechanical (*e.g.* bearing, valves, nozzles, armour, and prostheses) and protective coating applications. The recently discovered graphene has shown exceptionally high mechanical (Young's modulus of 1.0 TPa), electrical and thermal properties, which make it one of the most promising reinforcements for CMCs[34,36,95,195]. This 2D sheet of carbon has high surface areas than graphite, carbon black and CNTs, thus a small loading (less than 1.0 vol%) in a matrix may lead to large property improvements in the composites, whereas CNTs generally requires more (1-10 vol%) for toughening and strengthening of ceramics[17,25]. Therefore, it is intrigue to find out if this is the case for the tribological performance of the composites. Further, it is interesting to assess if the hybrid GNT reinforcement can outperform a singular reinforcement phase.

Following the successful generation and general mechanical property investigation of the Al_2O_3-GNT composites that are described in Chapters 4 and 5, we will continue to investigate the wear resistant performance of the nanocomposites. Focus will be laid on comprehensive performance assessments for the HPed composites with various GNT contents, under different sliding loads. Wear experiments were performed in The University of Nottingham on a wear testing machine using a ball-on-disc configuration in linear reciprocating mode. The test detail is described in Chapter 3, Section 3.5. We have achieved an excellent low wear rate, and analysed the wear mechanism based on SEM and Raman studies. We believe that this novel hybrid reinforcement could turn Al_2O_3 into a very useful wear resistant engineering material.

6.3 Mechanical properties and strucrural features of Al_2O_3-GNT composites

As a general tendency, the wear property of materials is closely attributed to their physical structures and mechanical properties, therefore we summarise the chemical composition, relative densities and their corresponding mechanical properties of different HP sintered Al_2O_3-GNT nanocomposites in Table 6.1, against pure Al_2O_3 samples.

Furthermore, the brittleness index (BI), defined as the H/K_{IC} ratio of a material which reflects the combined responses of the material to different loads, is a better parameter for the quantification of wear resistance than taking either the H or the K_{IC} alone separately[184]. A lower BI means that a lower hardness combined with higher fracture toughness will make the material more tolerant to damage during wear. On the contrary, a high BI is an indication of poor tolerance against wear. Thus, the BI values of various samples are also presented in Table 6.1.

Table 6.1 A summary of the relative densities, mechanical properties and brittleness index of the hot-pressed pure Al_2O_3 and nanocomposite samples.

Material	Sample ID	Relative density (%)	Hardness Vickers (GPa)	Flexural strength (MPa)	SENB Fracture toughness ($MPa.m^{1/2}$)	Brittleness Index (BI)
Pure Al_2O_3	$S_{0\text{-}0}$	98	15.9	369	3.5	4.5
Al_2O_3-0.5 wt% GNP	$S_{0.5\text{-}0}$	99.2	15.6	390	5.5	2.83
Al_2O_3-2 wt% GNP	$S_{2\text{-}0}$	98	7.5	296	3.9	1.92
Al_2O_3-5 wt% GNP	$S_{5\text{-}0}$	97	4.2	120	2.7	1.5
Al_2O_3-1 wt% GNP+ 1 wt% CNT	$S_{1\text{-}1}$	99	11.2	270	3.5	3.14
Al_2O_3-0.3 wt% GNP+ 1 wt% CNT	$S_{0.3\text{-}1}$	99	16	430	5.8	2.7

6.3 Coefficient of friction and weight loss of Al_2O_3-GNT nanocomposites

Fig. 6.1a represents the variation of coefficient of friction (COF) as a function of the GNP contents, at different loading conditions. It is clear that the COF trend is different at lower applied loads (5 N and 15 N) from that at higher applied loads (25 N and 35 N). Under lower applied loads (5 N and 15 N), there is a minimum point in the COF value for sample $S_{0.5\text{-}0}$ reached 0.4, with a 23% reduction using 15 N compared with the pure Al_2O_3 with the COF value of 0.58. When the load was increased to 25 N and 35 N, the COF continues to decrease with the GNP content increases. The different responses to varied applied loads during wear is related to the machanical properties

of the samples, which will be discussed later after the wear track analysis in section 6.4.

The weight loss varations as a function of GNP contents is shown in Fig. 6.1b. In all samples, the weight loss increased with increasing the sliding load. The lowest value for weight loss was observed for $S_{0.5\text{-}0}$, with a 60%, 70% and 80% reduction compared with $S_{0\text{-}0}$, under the sliding loads of 15 N, 25 N and 35 N, respectively. These results shows that, under low GNP contents up to 2 wt%, the composites outperformed the pure Al_2O_3; whilst at high GNP contents of 5 wt%, the wear performance of the composite deteriorated.

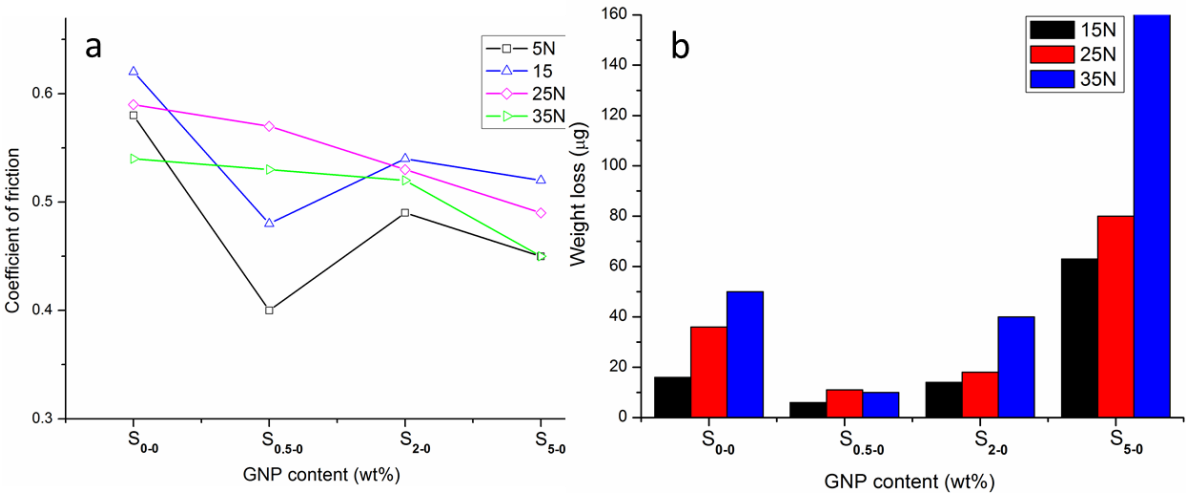

Fig. 6.1 Effect of GNP contents on: (a) coefficient of friction, and (b) weight loss of Al_2O_3-GNP composites tested at different loads.

The relationship between COF (using 15N sliding load), weight loss (using 15N sliding load) and fracture toughness is presented in Fig. 6.2. Under low GNP contents up to 2 wt%, there is a direct relationship between COF and weight loss. However from $S_{2\text{-}0}$, there is a sharp increase in weight loss from 14 µg in $S_{2\text{-}0}$ to 63 µg in $S_{5\text{-}0}$ while the COF reduced from 0.54 in $S_{2\text{-}0}$ to 0.52 in $S_{5\text{-}0}$. The high GNP content in sample $S_{5\text{-}0}$ caused less friction between the ball and the $S_{5\text{-}0}$ surface therefore reduced the COF. Meanwhile, the weight loss increment from $S_{2\text{-}0}$ to $S_{5\text{-}0}$ is in line with the fracture toughness reduction, from 3.9 MPa.m$^{1/2}$ in $S_{2\text{-}0}$ to 2.7 MPa.m$^{1/2}$ in $S_{5\text{-}0}$. Therefore, the increased weight loss in $S_{5\text{-}0}$ is associated with its mechanical properties. It is believed that the low fracture toughness in $S_{5\text{-}0}$ resulted in weak inter-granular strengths;

therefore more materials have been removed during the wear test, even though they have relatively low COF. Therefore, as shown in Fig. 6.2, all samples are corresponding to an opposite relationship between weight loss and fracture toughness.

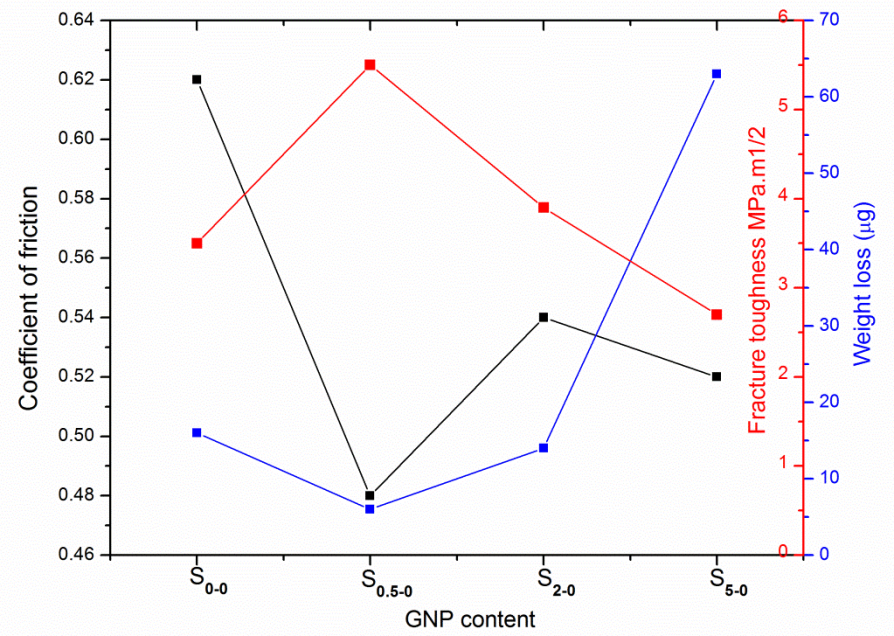

Fig. 6.2 The relationship between COF, weight loss, fracture toughness and GNP content.

6.4 Wear surface analyses

Fig. 6.3 shows the SEM images of the wear tracks of pure Al_2O_3 under four different sliding loads.The textures of the worn surfaces clearly depict the load-dependant wear behaviour in pure Al_2O_3 samples. As the sliding load increased, the wear track became wider. Moreover, the lower sliding loads (5 N and 15 N) produced relatively smoother wear track surfaces, with hardly any grains being pulled-out. However, the 25 N sliding load caused a larger area of grain pull-out (Fig. 6.3c), and the 35 N load led to even severe damage to the wear surfaces, with traces of wear groves and large residue debris on the surface, as shown in Fig. 6.3d. Such Al_2O_3 grain pull-outs under 25 N and 35 N sliding loads produced a large amount of wear debris which in turn resulted in abrasive sliding wear.

The SEM images of wear tracks of $S_{0.5\text{-}0}$ under four different sliding loads are shown in Fig. 6.4, which are entirely dissimilar to the wear tracks of pure Al_2O_3, as shown in Fig. 6.3. Under 25 N sliding load (Fig. 6.4c), there is no grains being pulled-out for $S_{0.5\text{-}0}$, whilst such a sliding load caused severe damage to the worn surfaces of the pure Al_2O_3 (Fig. 6.3c). For better understanding the wear track behavior of $S_{0\text{-}0}$ and $S_{0.5\text{-}0}$, a combination of test results including COF, fracture toughness and BI for $S_{0\text{-}0}$ and $S_{0.5\text{-}0}$ is presented in Fig. 6.5. Based on these pictorial worn surfaces detials, it seems that the higher fracture toughness of $S_{0.5\text{-}0}$ compared with pure Al_2O_3, as presented in Fig. 6.5, strengthened the grain boundaries and stopped the grains being pulled out at low sliding stresses and strains. In other words, the combination of lower BI and higher fracture toughness in $S_{0.5\text{-}0}$ compared with pure Al_2O_3 (Fig. 6.5) coresponds to the imroved wear properties in $S_{0.5\text{-}0}$ against pure Al_2O_3 in all sliding loads, as evident in wear tracks (Figs. 6.3 and 6.4). Even under 35 N load for $S_{0.5\text{-}0}$ (Fig. 6.4d), the grain pull-out damage was minimal, compared with the pure Al_2O_3 under the same sliding load (Fig. 6.3d). However, the grove traces in Fig. 6.4c and d indicate a deformation controlled wear behaviour under 25 N and 35 N sliding loads. This wear behaviour change probably weakened the lubricating merit of the GNPs in the composites under coarse wear, hence the reduction in COF for $S_{0.5\text{-}0}$ under higher sliding loads is not so obvious, as shown in Fig. 6.5. In this context, the 15 N sliding load was kept constant for comparing the wear performance of various Al_2O_3-GNT composites.

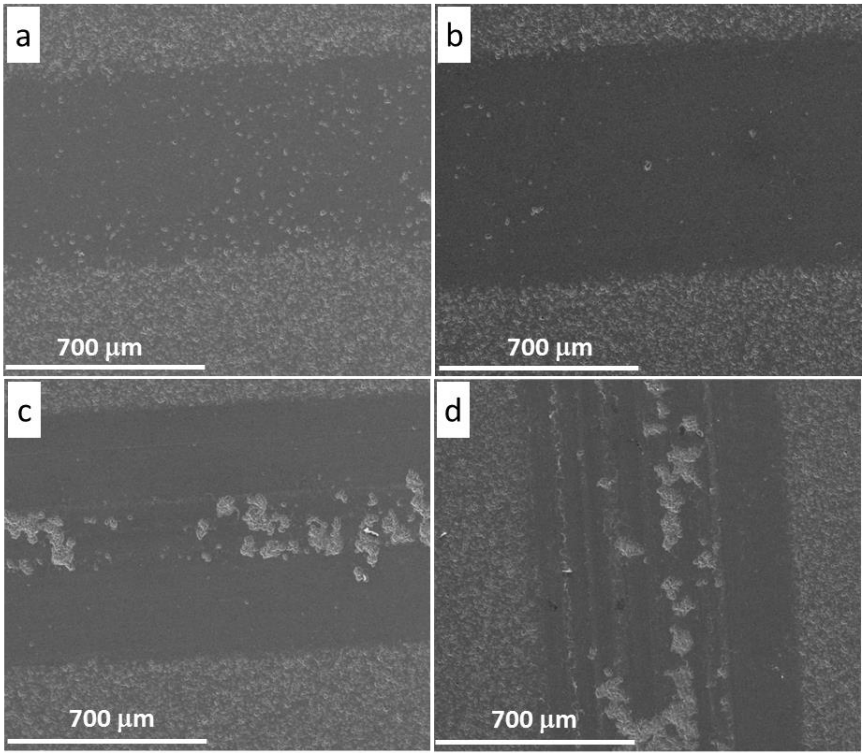

Fig. 6.3 SEM images of the wear track of pure Al_2O_3 ($S_{0\text{-}0}$) under various sliding loads. (a) 5 N, (b) 15 N, (C) 25 N, and (d) 35 N.

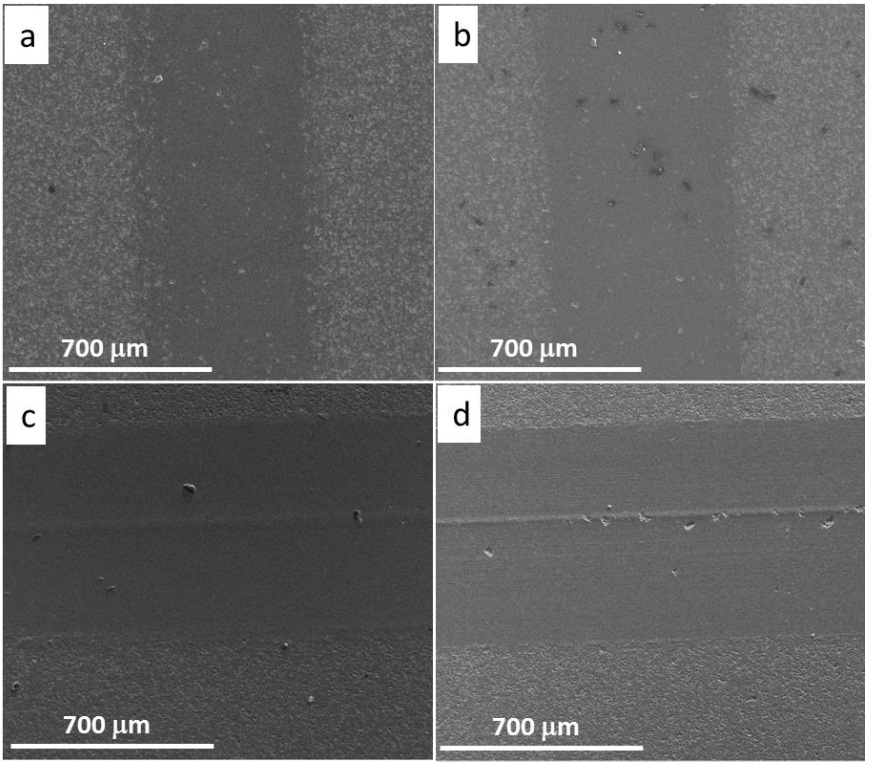

Fig. 6.4 SEM images of the wear track of sample $S_{0.5\text{-}0}$, under various sliding loads. (a) 5 N, (b) 15 N, (C) 25 N, and (d) 35 N.

The wear track profiles of pure Al_2O_3 and Al_2O_3-GNP composites are shown in Fig. 6.6a, and the wear rates were calculated usng equation 3.9 and plotted in Fig. 6.6b. According to the wear track profile (Fig. 6.6a), the GNP contents played a critical role in the tribological properties. The worn volume decreased with increasing GNP contents, up to 2 wt%, however adding 5 wt% GNPs deteriorated the wear resistant property and drastically increased the worn volume (Fig. 6.6a) and the wear rate (Fig. 6.6b). It is clear that adding 0.5 wt% GNPs into the Al_2O_3 matrix led to the biggest improvement in the wear resistance, resulting in over 70% reduction in the wear rate, benchmarked against the pure Al_2O_3 (Fig. 6.6b). Such a huge wear resistant improvement in the $S_{0.5\text{-}0}$ also matched well with the previously confirmed lowest COF of $S_{0.5\text{-}0}$ amongst other GNP single phase reinforced composites (Fig. 6.2a), and the lowest wight loss (Fig. 6.2b).

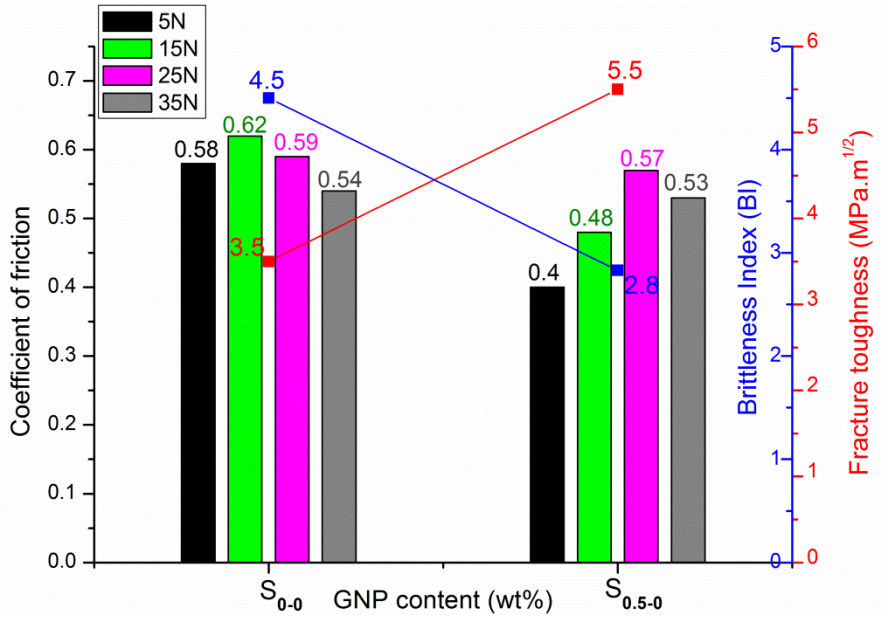

Fig. 6.5 The combination graph showing the relationship between COF, fracture toughness and BI for $S_{0\text{-}0}$ and $S_{0.5\text{-}0}$.

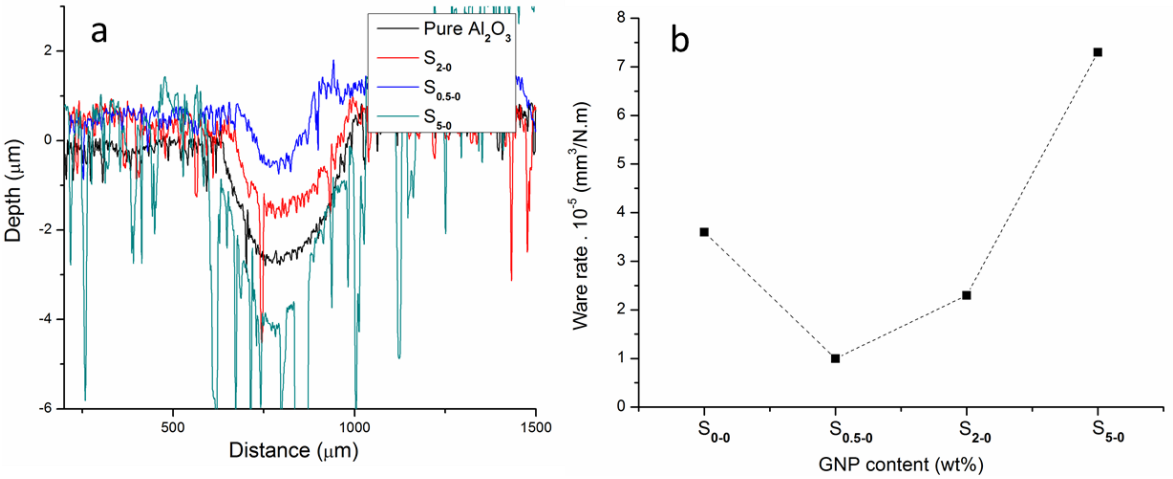

Fig. 6.6 Wear track profiles (a) and wear rates (b) of the pure Al_2O_3 and Al_2O_3-GNP composites.

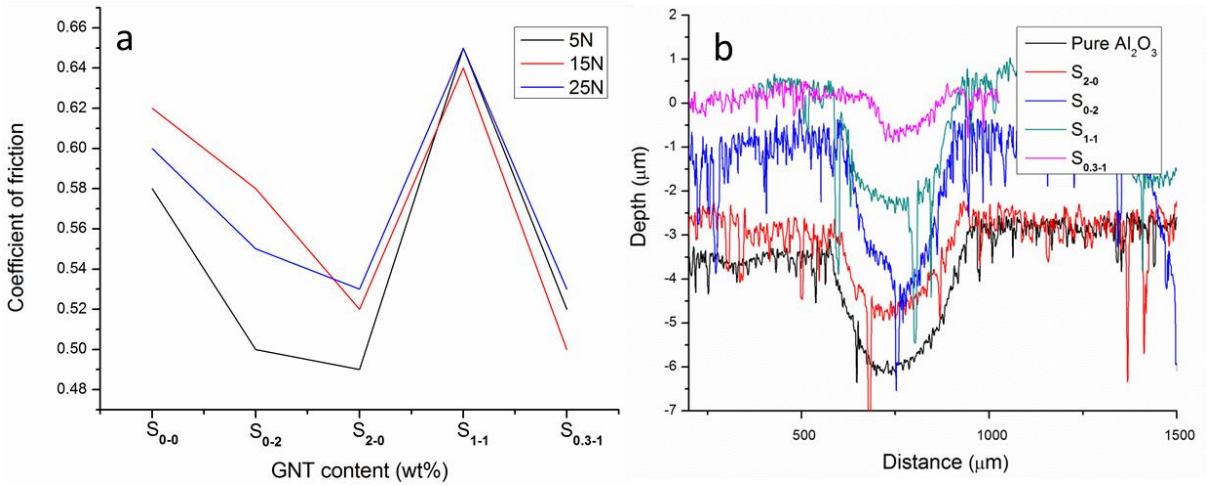

Fig. 6.7 A comparison of the coefficient of friction (a), and the wear track profiles (b) of the pure Al_2O_3 and Al_2O_3-GNT composite samples.

After adding the hybrid GNT reinforcement into the Al_2O_3 matrix, their COF and wear track profiles of the Al_2O_3-GNT composites are exhibited in Fig. 6.7a and b respectively, against the pure Al_2O_3. Sample $S_{0.3\text{-}1}$ showed a 20% reduction in the COF (Fig. 6.7a) and a 74% reduction in the worn volume, compared with the pure Al_2O_3, under the 15 N sliding load (Fig. 6.7b). The large improvements in the wear resistant properties are in line with the excellent mechanical properties for both $S_{0.5\text{-}0}$ and $S_{0.3\text{-}1}$ (Table 6.1). Conversely, the mechanically weak nanocomposites, $S_{5\text{-}0}$, exhibited poor wear resistance (Fig. 6.6).

Having compared the wear tracks of $S_{0.5\text{-}0}$ and $S_{0.3\text{-}1}$, we realise that $S_{0.3\text{-}1}$ outperformed $S_{0.5\text{-}0}$ marginally, with a slightly smaller worn volume and lower wear rate (Fig. 6.8a and b).

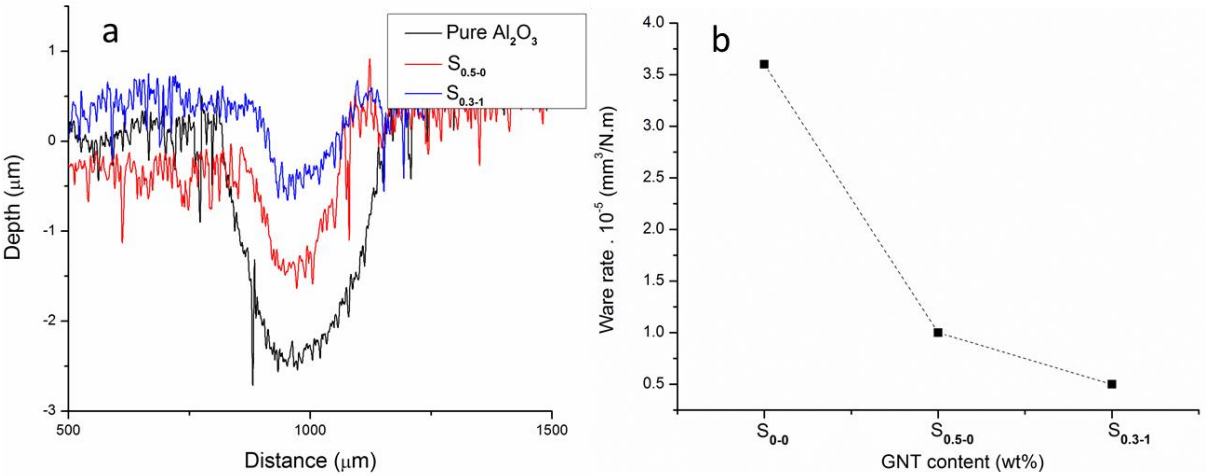

Fig. 6.8 A performance comparison of the $S_{0.5\text{-}0}$ and $S_{0.3\text{-}1}$ against pure Al_2O_3. (a) Wear track profiles, and (b) wear rates.

Its wear rates dropped by 70% (from 3.6 $mm^3/N{\cdot}m$ in $S_{0\text{-}0}$ to 1 $mm^3/N{\cdot}m$ in $S_{0.5\text{-}0}$) and by 86% for $S_{0.3\text{-}1}$ (from 3.6 $mm^3/N{\cdot}m$ in $S_{0\text{-}0}$ to 0.5 $mm^3/N{\cdot}m$ in $S_{0.3\text{-}1}$) against Al_2O_3. The hybrid reinforcement shows huge potentials in tailoring the wear properties of the composites.

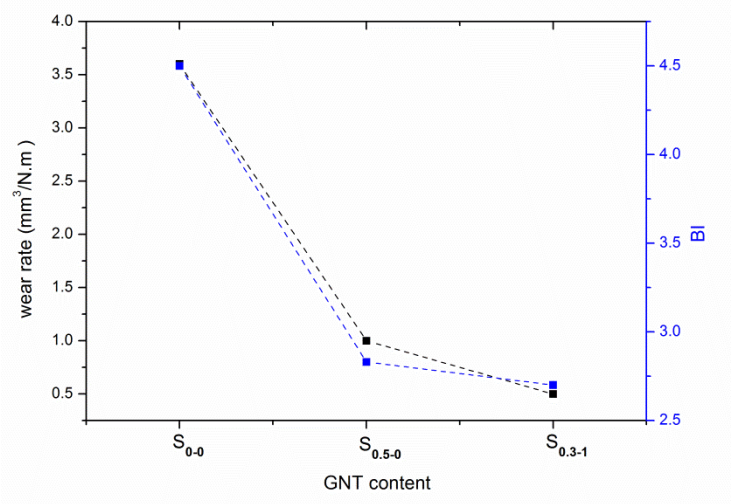

Fig. 6.9 Wear rate and BI values against GNT content.

Further, in Fig. 6.9, we compared the above excellent tribological results of the composites with their BI values. Lower BI values means lower hardness with higher fracture toughness which is an indirect indication of improved wear resistance properties and also better machinability. Lower wear rate is also a direct indication of improved wear properties. Therefore, direct relationship between BI and wear rate values in Fig. 6.9 confirms the reliability of our data. As shown in Fig. 6.9, the BI value slightly reduced from 2.83 in $S_{0.5\text{-}0}$ to 2.7 in $S_{0.3\text{-}1}$, which is in line with the wear rate trend. This means that the former has better wear and machinary properties than $S_{0.5\text{-}0}$. This further confirms the advantages of applying hybrid reinforcement in ceramic composites.

6.5 Wear mechanism discussion

To understand the role of GNTs in the wear mechanism, 5 different samples with various GNT contents were chosen and their wear tracks were further investigated by using SEM, compared with wear tracks of the pure Al_2O_3, and the results are shown in Figs. 6.10 and 6.11. All the selected wear tracks were subject to the same sliding loads, for the purpose of comparison.

As described earlier, the surface of pure Al_2O_3 is unsmooth, with large islands of pull-out grains (Fig. 6.10a). Within the grains, a large amount of debris was visible at higher resolution images. Fig. 6.11a shows the coarse wear behaviour discussed above. Adding 0.5 wt% of GNP alone into the Al_2O_3 made the wear track narrower (Fig. 6.10b) than that of the pure Al_2O_3, and a smooth lubricating film (tribofilm) appeared on the worn surface due to existence of GNPs, as shown in Fig. 6.11b. This smooth tribofilm decreased the wear friction between the sample and the counterpart ball, thus improved the wear resistance, as shown in Fig. 6.6. Further GNP addition up to 2 wt% led to a decreased area of the smooth tribofilm (Fig. 6.10c), and micro chipping with grain pull-outs also became visible on the worn surface (Fig. 6.11c), compared with $S_{0.5\text{-}0}$. The deteroiated wear resistance for $S_{5\text{-}0}$ (Fig. 6.10d) corresponded to large areas of inter-granular grain pull-out, as shown in Figs. 6.10d and 6.11d, due to its poor mechaninal properties as listed in Table 6.1. The wear track became narrowest, even narrower in $S_{0.3\text{-}1}$ than $S_{0.5\text{-}0}$ (Fig. 6.10e), corresponding to the highest amount of

coherent tribofilm (Fig. 6.11e). These study confirmed the key relationship between the GNT content and the formation of a tribofilm during wear, and helped to explain why the $S_{0.3\text{-}1}$ exhibited even better wear resistant behavior than the $S_{0.5\text{-}0}$ as presented in Fig. 6.8.

Further, the fracture toughness of $S_{0.3\text{-}1}$ is slightly higher than that of $S_{0.5\text{-}0}$, due to different roles of GNPs and CNTs in toughening the composites, as discussed previously for $S_{0.5\text{-}1}$[195]. Easier CNT de-boundling in the presence of GNPs is another advantage of the hybrid reinforcement agent in $S_{0.3\text{-}1}$, which helped the well-dispersed CNTs to better exhibit their merits in the composites, than them working alone.

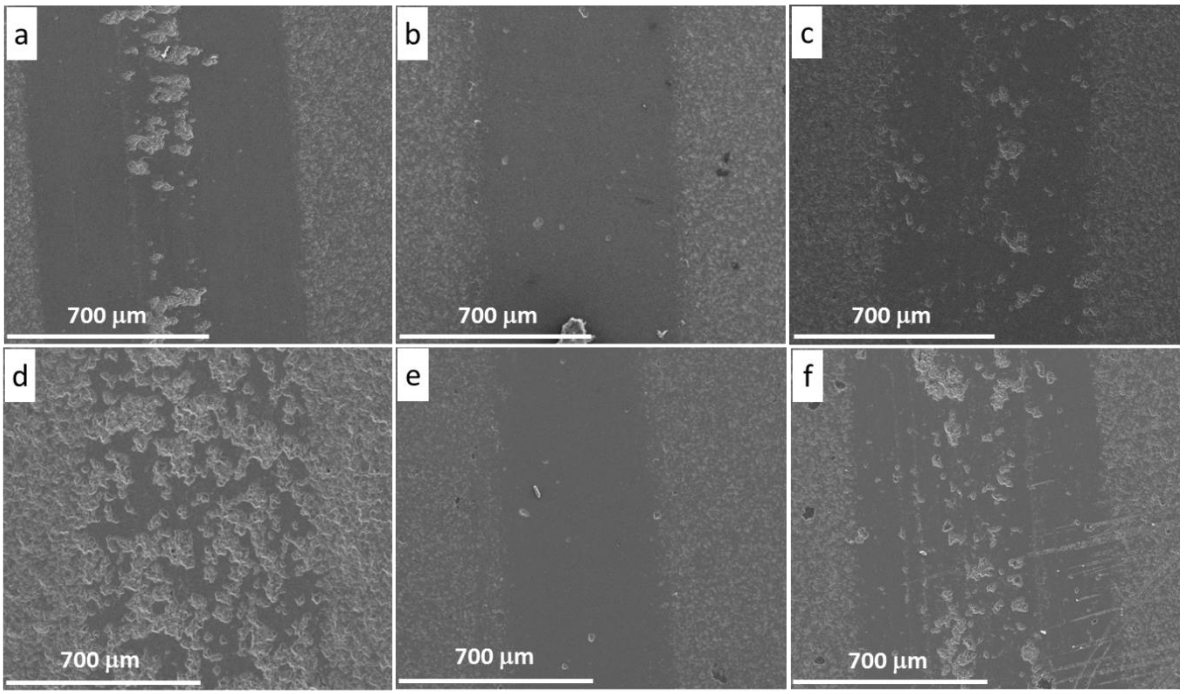

Fig. 6.10 SEM images of wear tracks. (a) Pure Al_2O_3, (b) $S_{0.5\text{-}0}$, (C) $S_{2\text{-}0}$, (d) $S_{5\text{-}0}$, (e) $S_{0.3\text{-}1}$ and (f) $S_{1\text{-}1}$.

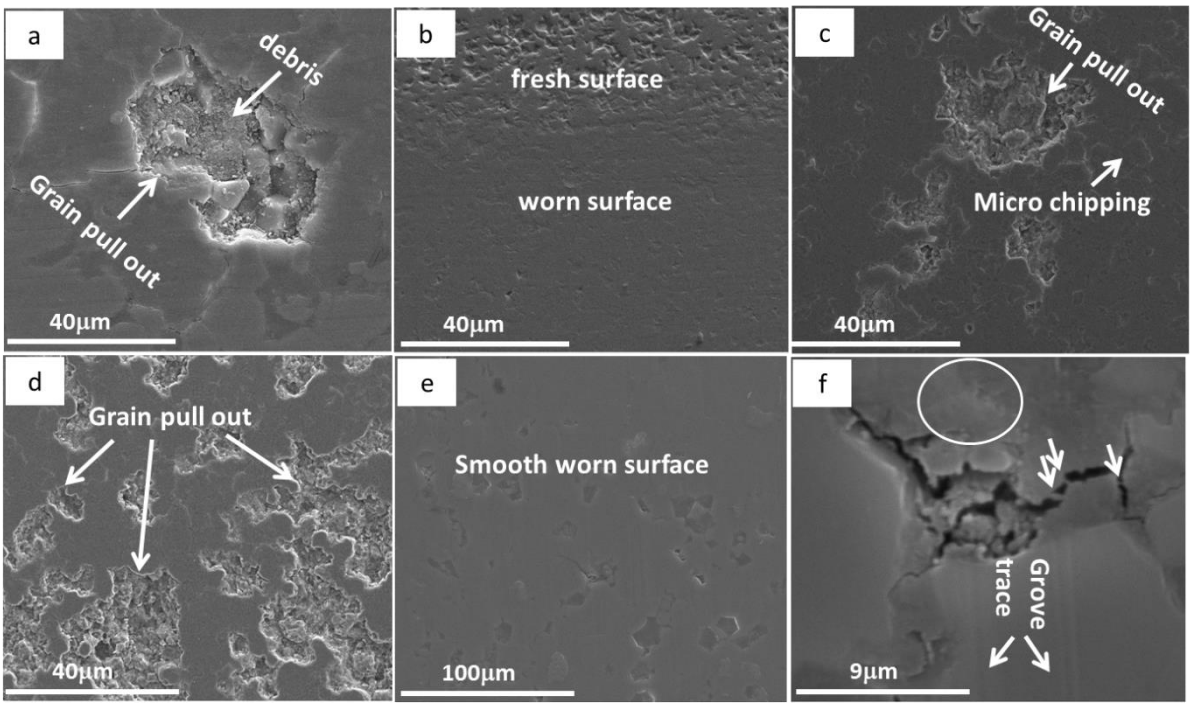

Fig. 6.11 SEM images. (a) Pure Al_2O_3, (b) $S_{0.5\text{-}0}$, (C) $S_{2\text{-}0}$, (d) $S_{5\text{-}0}$, (e) $S_{0.3\text{-}1}$, and (f) higher resolution image of (e).

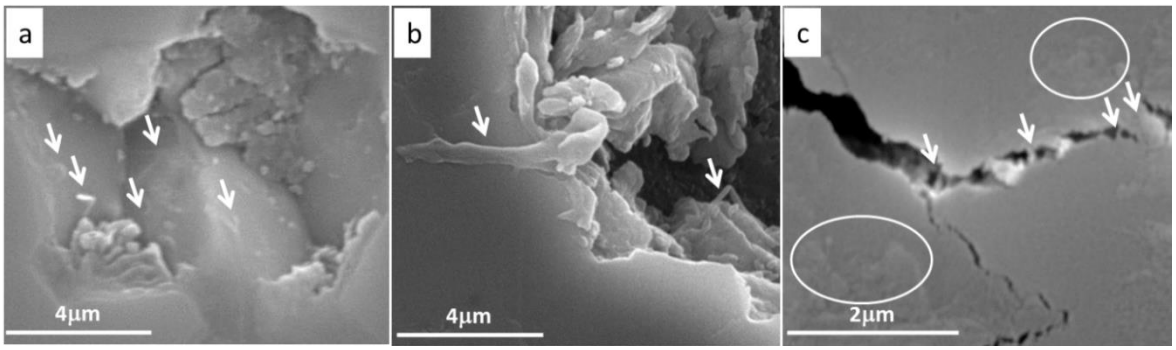

Fig. 6.12 High resolution SEM images from $S_{0.3\text{-}1}$ showing: (a) embedded CNTs, (b) embedded GNPs on the top of a worn surface, (c) CNT bridging cracked grains (arrowed) and GNP lying on the worn surface (circled).

The reduced grain pull-outs might be owing to less tangential frictional forces between the ball and the composite surface, due to the formation of a protective tribofilm by the GNT exfoliation on the wear surface. Fig. 6.12a-c provides evidence for the direct role of GNTs in the formation of the protective tribofilm during the wear test. The embedded GNTs from unpolished (ground only) surface will be exposed and spread on the wear track during the reciprocating movements, to form the tribofilm (Fig. 6.12a and b). The flattened GNTs on the worn surface are clearly visible in Figs. 6.11f and 6.12c (circled), which could be the feeding stock for the tribofilm. GNPs are likely to contribute more

effectively to the tribofilm than that of CNTs, due to their 2D layered and their easy to be exfoliated structures; whilst CNT's rolling effect[196], along with such tribofilms, cannot be ignored in the reduction of COF and wear rates. Further, the existence of CNTs indirectly contributed more to bridge the grains against crack propagations (due their higher aspect ratio) in case of micro-chipping and grain pull-outs, by improving the mechanical properties of the composites (arrows in Figs. 6.11f and 6.12c). In fact, samples without CNTs but with higher GNP contents ($S_{2\text{-}0}$ and $S_{5\text{-}0}$) drastically degraded the wear resistant property (Fig. 6.6), because of the poor mechanical properties (Table 6.1) which ended up with severer grain pull-outs (Fig. 6.10c and d). Therefore, both the lubricating film and the improved mechanical properties together improved the wear resistant properties of the composites.

Furthermore, although sufficient amounts of flattened CNTs on the wear track could indeed lubricate the surface, as reported for the Al_2O_3-5 wt% CNT composites[196], the fact that very low GNP contents ($S_{0.5\text{-}0}$ and $S_{0.3\text{-}1}$) in the composites could lead to the formation of tribofilms suggests the dominant role of GNPs in the improved tribological performance in this context. The existence of the fragmented GNPs during tribology testing is confirmed by our Raman studies, as shown in Fig. 6.13.

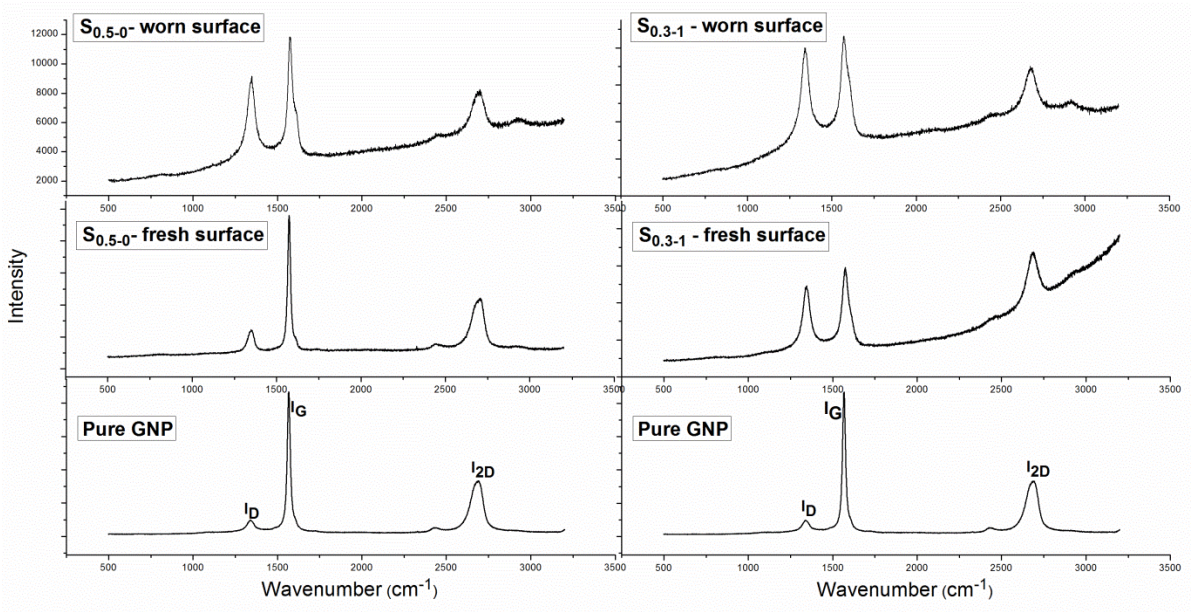

Fig. 6.13 The comparison of Raman scans of pure GNP and Al_2O_3-GNT composites obtained from surfaces with and without wear.

Two types of area on $S_{0.5\text{-}0}$ and $S_{0.3\text{-}1}$ were chosen during our Raman scanning: 1) surfaces away from wear damaged areas (*i.e.* no influence of the wear); and 2) surfaces inside the wear tracks which were subject to the entire wear process. Compared with the pure GNP Raman spectra, three typical peaks were observed at ~1350 cm^{-1} (D band), ~1585 cm^{-1} (G band) and ~2700 cm^{-1} (2D band) in the fresh surfaces for $S_{0.5\text{-}0}$ and $S_{0.3\text{-}1}$[197], confirming that there is no damage to GNPs during our sintering process. Inside the wear track of $S_{0.5\text{-}0}$, the scans revealed an increase in the D peak intensity. The increased D peak intensity is directly related to the number of edges, corresponding to more GNP flakes in this context, given the uniform GNP dispersion in the as-synthesised composites. Thus, the increased I_D/I_G ratios inside the wear track of $S_{0.5\text{-}0}$ indeed confirmed the formation of extra fragmented GNP flakes during the tribology testing. Further, the exfoliation and fragmented flakes are believed to be the source for the tribofilm formation. Similar behaviour has also been observed by other authors for silicon nitride-GNP composites[198,199]. The increases in the I_D/I_G ratios in worn surfaces of $S_{0.3\text{-}1}$ are also obvious, indicating the exfoliation and tribofilm formation, even at very low GNP content. Another interesting point about the Al_2O_3-GNT composites is that such tribofilms could be maintained during the entire wear process, as damaged tribofilms on the surface can continuously be replaced or regenerated by the embedded GNTs inside the Al_2O_3 matrix.

6.6 Conclusion

The tribological properties of the hybrid GNT reinforced-Al_2O_3 composites were investigated using a ball-on-disc technique. Samples designated as $S_{0.5\text{-}0}$ and $S_{0.3\text{-}1}$ showed a remarkable 70% and 86% reduction in the wear rate and 23% and 20% reduction in COF values, respectively, against the pure Al_2O_3, under 15 N sliding load. It was identified that the superior mechanical traits of the $S_{0.5\text{-}0}$ and $S_{0.3\text{-}1}$ samples, in terms of fracture toughness against pure Al_2O_3, and the formation of a protective tribofilm on the wear track are the effective wear mechanisms for converting Al_2O_3-GNT composites into wear resistant materials. The CNTs played a vital indirect role in the former by improving the mechanical properties, whilst GNPs contributed directly to the latter tribofilm formation which is more dominant for the reduced COF. These newly developed novel hybrid composites, possessing promising toughness and

tribological performance, could extend their application to many new fields as advanced structural materials, protective coatings for micro-mechanical systems and contact-damage-resistant components.

Chapter 7 Al_2O_3-GONT composites: fabrication, structural features and mechanical properties.

7.1 Introduction

In this Chapter, two new strategies will be applied to fabricate Al_2O_3 CMCs, and the results will be compared with previously prepared Al_2O_3-GNP nanocomposites. Firstly, the GONT hybrid reinforcement (a blend of GO and CNT) was applied instead of GNT (a blend of GNP and CNT) into the Al_2O_3, and the influence on the microstructure and mechanical properties of the resulting Al_2O_3-GONT nanocomposites will be investigated. Secondly, the Al_2O_3-GONT nanocomposites will be prepared from two different types of starting materials, the AlOOH (boehmite) and γ-Al_2O_3, via a sol-gel and a powder mixing process, respectively. Finally, the Al_2O_3 phase transformation path changes during the HP sintering process and their effects on the microstructures and mechanical properties of the nanocomposites will be investigated.

7.2 Powder mixing process *vs* sol-gel process

GO, with hydrophilic oxidation groups, can be easily dispersed into water to form a stable colloidal suspension. Recent studies have proved that it is possible to disperse multi-walled and single-walled CNTs in an aqueous solution via non-covalent interactions, without any surfactants and dispersants. By changing the weight ratios between the GO and CNTs, a hydrogel of GO/CNTs can form, owing to the strong π-π interactions. In this regard, we have also tried to prepare well-dispersed hybrid suspensions of GO and MWCNTs in Al_2O_3, to fabricate Al_2O_3-GONT nanocomposites, in an effort to achieve improved mechanical properties.

In the sol-gel method, AlOOH was used as the starting material for the mixing process by preparing a sol. On contrast, in the conventional powder processing, γ-Al_2O_3 powder was used as the starting material. Therefore, the main difference lies in the initial Al_2O_3 phase, which may cause the Al_2O_3 to undergo different paths of phase transformation during the sintering process. Various GO/CNT contents were used, and details of samples are listed in Table 7.1. In the sample ID section in the table, SP represents the standard powder processing, and SS for the sol-gel method. Each

sample has a X-Y index, where X represents the GO wt.% and Y for the CNT wt.%. All samples were HP-sintered at 1650 °C, under Ar atmosphere with 1 h dwelling time.

Table 7.1 Material specifications for the preparation of Al_2O_3-GONT nanocomposites

Sample ID	Matrix	GO (wt.%)	CNT (wt.%)	Synthesis procedure	Density (%)
SP_{0-0}	γ-Al_2O_3	0	0	HP 1650°C, Ar, 1 h	98
$SP_{0.5-0}$	γ-Al_2O_3	0.5	0	HP 1650°C, Ar, 1 h	99.3
$SP_{0.5-0.5}$	γ-Al_2O_3	0.5	0.5	HP 1650°C, Ar, 1 h	99.6
SS_{0-0}	AlOOH	0	0	HP 1650°C, Ar, 1 h	99
SP_{1-1}	γ-Al_2O_3	1	1	HP 1650°C, Ar, 1 h	99.8
SS_{1-1}	AlOOH	1	1	HP 1650°C, Ar, 1 h	99.9
SS_{1-2}	AlOOH	1	2	HP 1650°C, Ar, 1h	99.7
SS_{2-4}	AlOOH	2	4	HP 1650°C, Ar, 1h	99.4
SS_{2-0}	AlOOH	2	0	HP 1650°C, Ar, 1h	99.3

7.2.1 Dispersion behaviour of AlOOH and γ-Al_2O_3 in water

As our mixing process is based on wet mixing technique, it is crucial to study the dispersion behaviour of AlOOH and γ-Al_2O_3 in water. In this regard, 10 g of each powder were dispersed in water using probe-sonication and incubated for 1 h (Fig. 7.1a and b). Fig. 7.1b shows that the AlOOH aqueous suspension is very stable after 1 h, without any sedimentation, while the aqueous γ-Al_2O_3 suspension formed thick sediment at the bottom of the beaker after 1 h (circled in Fig. 7.1b). This is due to the existence of OH groups in the AlOOH which make it strongly hydrophilic to attach to water molecules and form a sol, whilst Al_2O_3 is chemically stable, and it is unable to make any interactions with water molecules (Fig. 7.2).

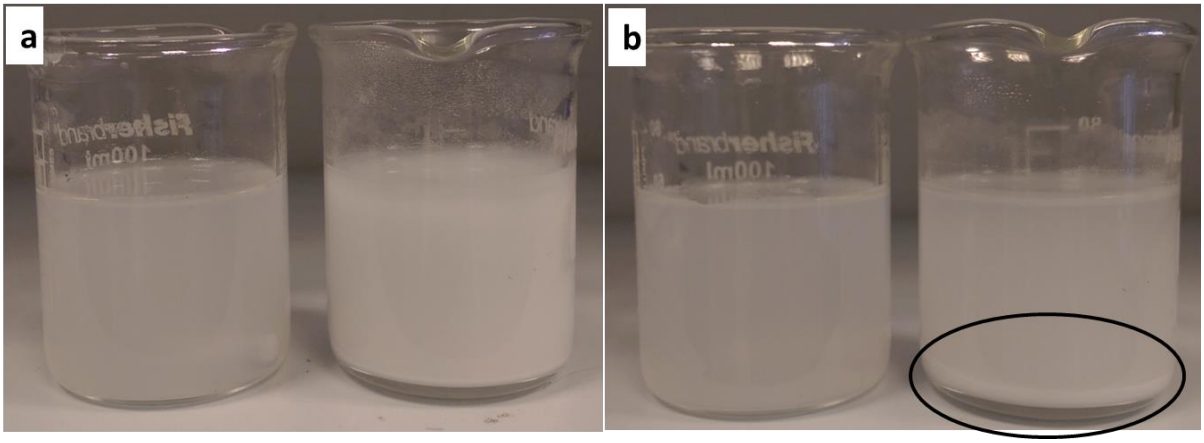

Fig. 7.1 a) The aqueous suspensions of AlOOH (left beaker) and γ-Al_2O_3 (right beaker), photo taken immediately after the probe-sonication. (b) The aqueous suspensions of AlOOH (left beaker) and γ-Al_2O_3 (right beaker), photo taken after 1 h of sonication.

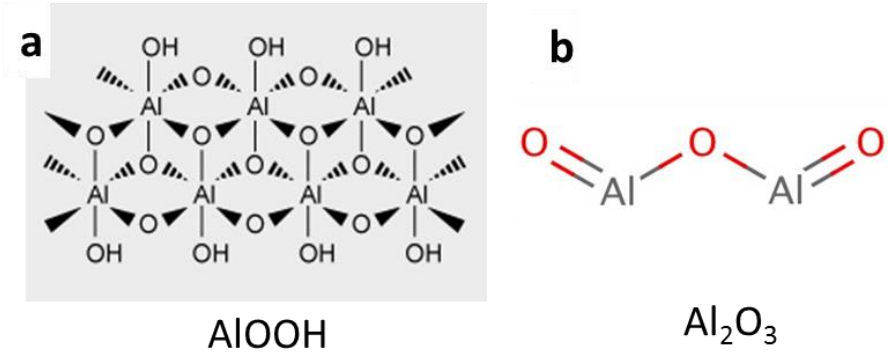

Fig. 7.2 Chemical formula of (a) AlOOH, and (b) Al_2O_3.

7.2.2 Raman

Fig. 7.3 shows the Raman spectra of Al_2O_3-2wt%GO ($SS_{2\text{-}0}$) powder and $SS_{2\text{-}0}$ nanocomposite after HP which shows the structural changes of the GO during the sintering process. Typically, two main bands appeared in the spectra of graphite and graphene-based materials are observed here i.e. the G band assigned to the scattering of the E_{2g} phonon from sp^2 carbon (graphite lattice), and the D band resulting from the structural imperfections.

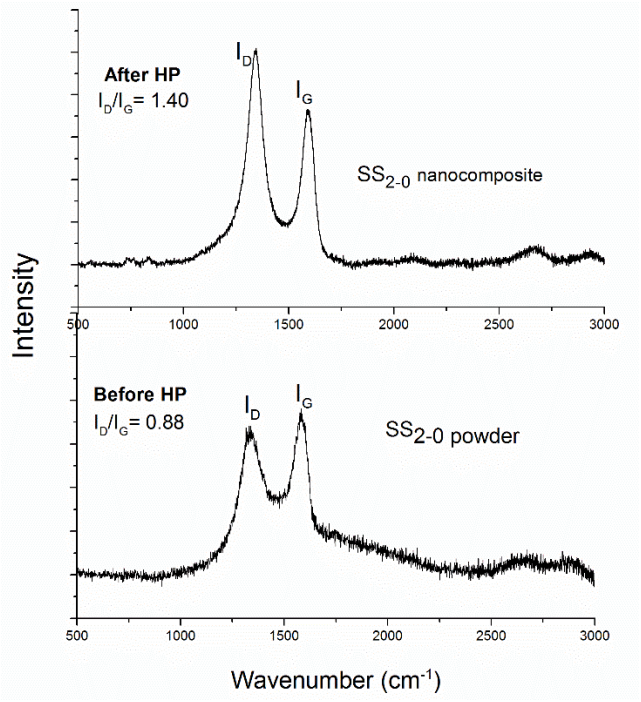

Fig. 7.3 Raman spectra of SS_{2-0} powder and SS_{2-0} nanocomposite.

The intensity ratio of D to G peak I_D/I_G is 0.88 and 1.4 in SS_{2-0} powder and SS_{2-0} nanocomposite respectively. The increase of I_D/I_G ratio after reduction is commonly found in GO chemical reduction studies[200-202]. It indicates that the GO in SS_{2-0} powder was reduced during the HP process and transferred to reduced GO (rGo) in the SS_{2-0} nanocomposite under our sintering condition. The increment in I_D/I_G ratio after the reduction can be attributed to the decrease in the average size of the sp^2 domains upon reduction of the GO, in which new graphitic domains were created that have smaller sizes than the ones present in GO before the reduction, but are larger in quantities. Therefore, although there are more defect-free sp^2 species after the reduction form smaller domains than those in the GO, which leads to large quantities of structural defects[203]. Another possible reason is the increased fraction of graphene edges, which could also contribute to the increase in the I_D/I_G ratio[204]. Accordingly, the spontaneous SS_{2-0} sintering and GO reduction will saves energy and time.

7.3 Effect of the GONT contents on the microstructure of Al_2O_3-rGONT nanocomposites prepared by powder processing

The thermally etched surfaces of the Al_2O_3-rGONT nanocomposites with various GO/CNT ratios prepared by powder processing are shown in Fig. 7.4a-d. By comparing the hybrid reinforced composites ($SP_{0.5\text{-}0.5}$ and $SP_{1\text{-}1}$) with the single phase reinforced composite ($SP_{0.5\text{-}0}$), we find that the CNTs are more effective on the grain size retardation in $SP_{0.5\text{-}0.5}$ and $SP_{1\text{-}1}$ than that of GO in $SP_{0.5\text{-}0}$. Accordingly, the grain size was reduced in $SP_{0.5\text{-}0.5}$ and $SP_{1\text{-}1}$ by up to 35.5% and 38% compared with $SP_{0\text{-}0}$ respectively, as evident in Fig. 7.5. However, there is no grain reduction effect in $SP_{0.5\text{-}0}$ compared with $SP_{0\text{-}0}$, whilst a slight increment in grain size was observed (Fig. 7.5). As all the samples were produced by powder processing, we believe that the different grain sizes are attributed to a different grain-growth retardation mechanism, originating from the dimensionalities of the GO itself and the hybrid rGONTs reinforcements. To investigate this mechanism, fractured surfaces of Al_2O_3-rGONT nanocomposites prepared by powder processing are presented in Fig. 7.6.

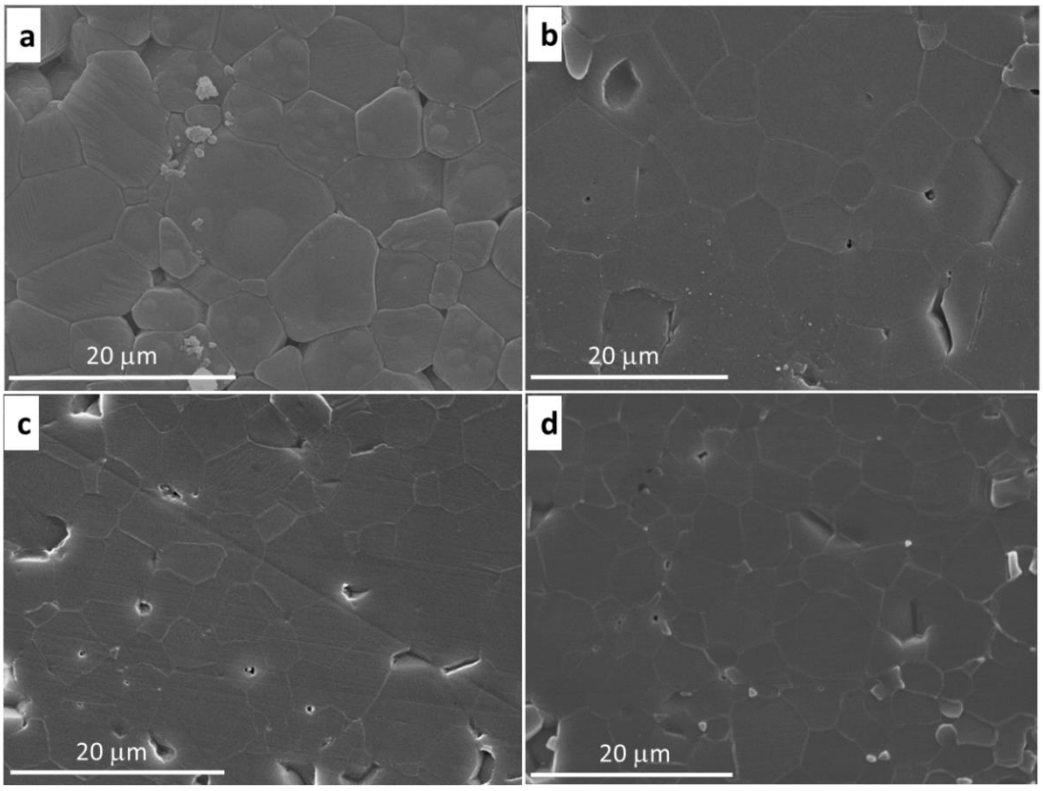

Fig. 7.4 SEM images from thermally etched surfaces of (a) $SP_{0\text{-}0}$, (b) $SP_{0.5\text{-}0}$, (c) $SP_{0.5\text{-}0.5}$ and (d) $SP_{1\text{-}1}$.

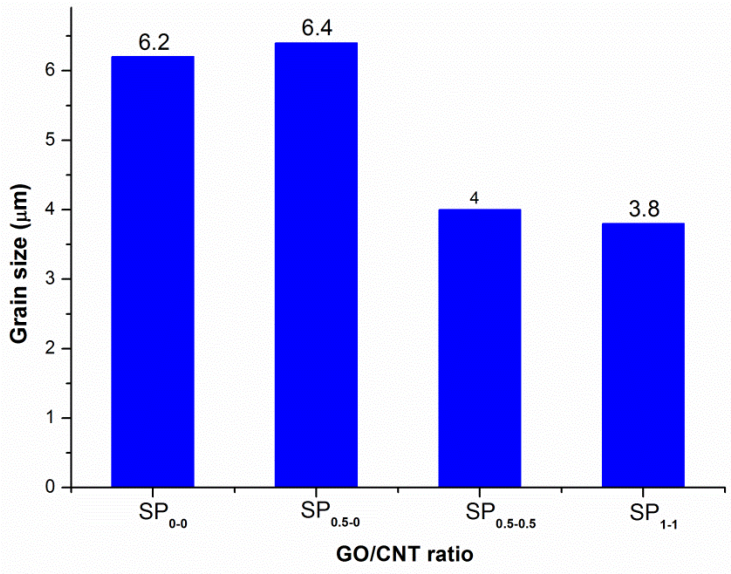

Fig. 7.5 Grain size measurements of (a) $SP_{0\text{-}0}$, (b) $SP_{0.5\text{-}0}$, (c) $SP_{0.5\text{-}0.5}$ and (d) $SP_{1\text{-}1}$.

As can be seen from the fractured surface of $SP_{0.5\text{-}0}$ (Fig, 7.6b), some individual GO flakes are found embedded inside the grains, but on the fractured surface of $SP_{0.5\text{-}0.5}$ (Fig. 7.6c), some CNT bundles are located within the grain boundaries and form a strong entangled network around the grains, which pinned the grains and reduced atomic diffusion coefficient, hence constrained the grain growth. Moreover, due to the synergetic effect and π-π interactions between GO and CNT, GO flakes contributed to the grain refinement via the CNTs, by preventing the agglomeration of CNT bundles, so that individual CNTs may end up with rolling around the grain boundaries during growth (Fig. 7.6c). Therefore, the grain refinement being more effective in $SP_{0.5\text{-}0.5}$ and $SP_{1\text{-}1}$ compared with $SP_{0.5\text{-}0}$, confirms the success for the hybrid GONT strategy.

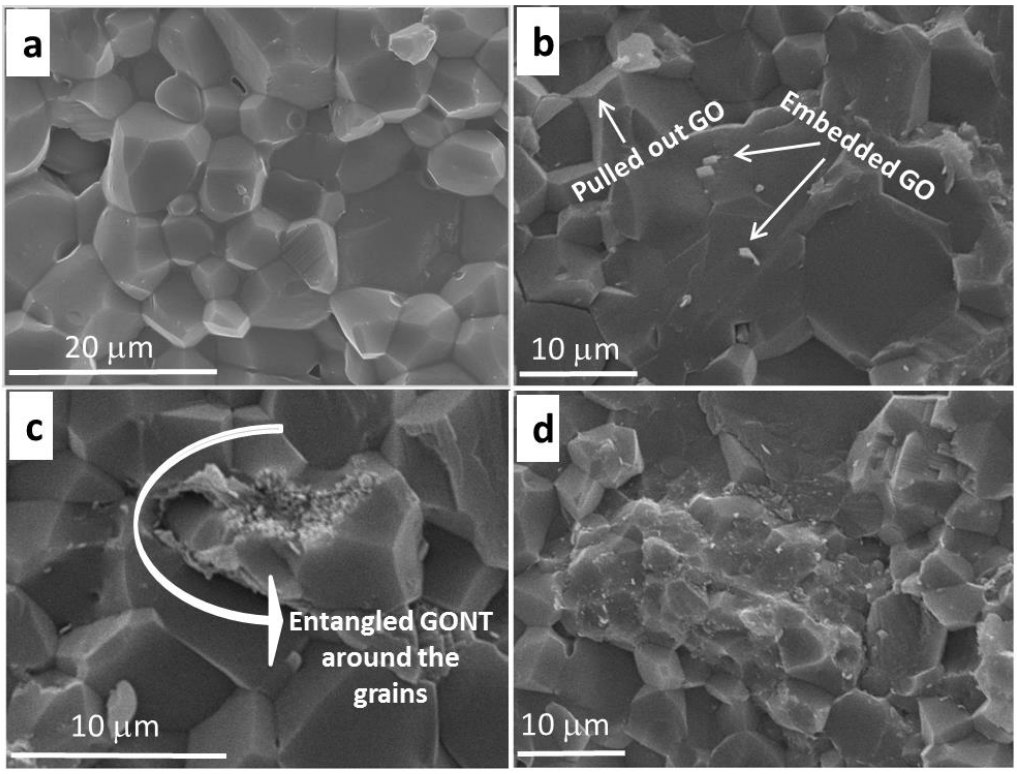

Fig. 7.6 SEM images of fractured surfaces of (a) pure Al_2O_3, (b) $SP_{0.5\text{-}0}$, (c) $SP_{0.5\text{-}0.5}$ and (d) $SP_{1\text{-}1}$.

7.4 Effect of processing method on microstructure of Al_2O_3-rGONT composites

To investigate effects of the initial Al_2O_3 phase during mixing on the microstructure of Al_2O_3-rGONT composites, samples containing 1 wt% GO and 1 wt% CNTs were prepared using γ-Al_2O_3 and AlOOH via powder and sol-gel process, named as $SP_{1\text{-}1}$ and $SS_{1\text{-}1}$, respectively. The thermally etched surfaces are presented in Fig. 7.7, and the grain size values of the same samples are presented in Fig. 7.8.

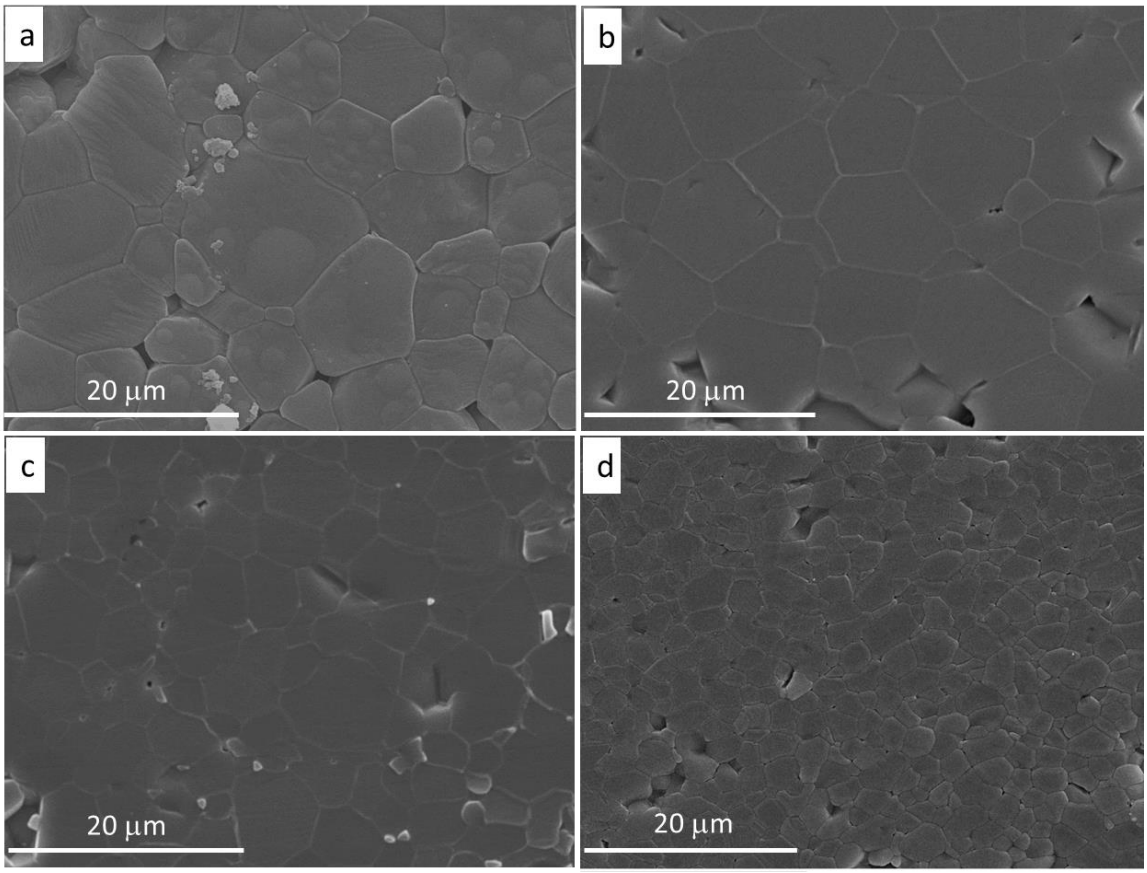

Fig. 7.7 SEM images of thermally etched surfaces of (a) $SP_{0\text{-}0}$, (b) $SS_{0\text{-}0}$, (c) $SP_{1\text{-}1}$, and (d) $SS_{1\text{-}1}$.

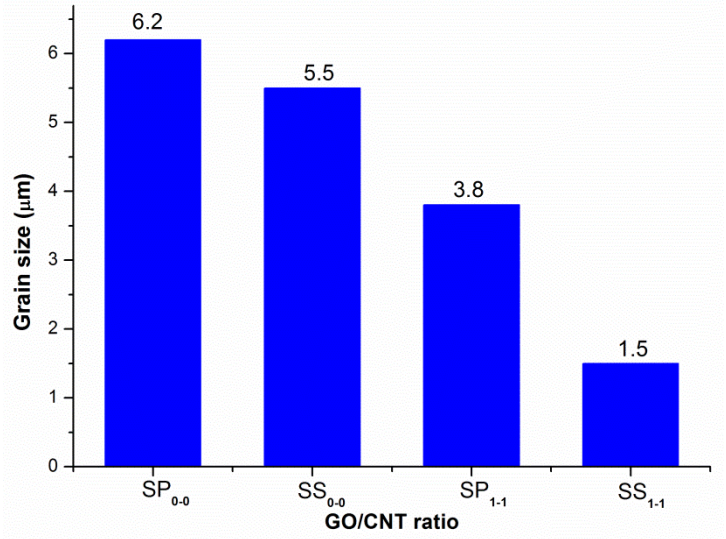

Fig. 7.8 Grain size values for different samples: $SP_{0\text{-}0}$, $SS_{0\text{-}0}$, $SP_{1\text{-}1}$ and $SS_{1\text{-}1}$.

As shown in the thermally etched surfaces of $SP_{1\text{-}1}$ and $SS_{1\text{-}1}$ in Fig. 7.7, there is a very large difference between the grain size of $SP_{1\text{-}1}$ and $SS_{1\text{-}1}$ with the same GONT content. Accordingly, sample $SS_{1\text{-}1}$ showed a 62% grain size reduction compared with

sample $SP_{1\text{-}1}$ (Fig. 7.8), and a 74% reduction against sample $SS_{0\text{-}0}$. As the GONT contents are identical in both samples, such grain refinement is due to the effect of sol-gel process in $SS_{1\text{-}1}$, which led to better GONT dispersion in the AlOOH matrix than that of sample $SP_{1\text{-}1}$ which was prepared by powder processing, and the better dispersed nanomaterials stopped the grain growth. However such grain retardation may not be solely due to the pining effect of GONTs in the final microstructures of $SS_{1\text{-}1}$. The existence of GONTs in the AlOOH matrix may have probably affected the kinetics of the phase transformation behaviour from AlOOH to Al_2O_3, as well as its sintering behaviour. To understand such remarkable grain size retardation in $SS_{1\text{-}1}$, the phase transformation behaviour of Al_2O_3 and the sintering profiles of $SP_{1\text{-}1}$ and $SS_{1\text{-}1}$ will be further investigated below.

7.4.1 Phase transformation in Al_2O_3 powder and sintering profiles of $SP_{1\text{-}1}$ and $SS_{1\text{-}1}$

It is well-known that pure $Al(OH)_3$ dry gel undergoes the following phase transformations during heating[205].

$Al(OH)_3 \rightarrow AlOOH \rightarrow \gamma\text{-}Al_2O_3 \rightarrow \delta\text{-}Al_2O_3 \rightarrow \theta\text{-}Al_2O_3 \rightarrow \alpha\text{-}Al_2O_3$

Upon heating, $\gamma\text{-}Al_2O_3$ undergoes a series of polymorphic change before reaching the stable corundum structured $\alpha\text{-}Al_2O_3$ form. The $\gamma \rightarrow \delta$ and $\delta \rightarrow \theta$ transformations are displacive with relatively low activation energies. From $\gamma\text{-}Al_2O_3$ to $\theta\text{-}Al_2O_3$ the change is called transition Al_2O_3 phase. The $\theta \rightarrow \alpha$ transformation is reconstructive and proceeds through a nucleation and growth process. In this regard, $\alpha\text{-}Al_2O_3$ nuclei form within the ultrafine $\theta\text{-}Al_2O_3$ matrix, but rapidly grow to produce $\alpha\text{-}Al_2O_3$ so elevated temperatures are needed to nucleate $\alpha\text{-}Al_2O_3$. Normally, the $\theta\text{-}Al_2O_3$ to $\alpha\text{-}Al_2O_3$ transformation temperature is as high as 1300 °C.

As it can be seen in the XRD profiles shown in Fig. 7.9, calcining AlOOH at 800 °C resulted in the formation of $\gamma\text{-}Al_2O_3$. However, by calcination at 1200 °C for 5 h, AlOOH was completely transformed to $\alpha\text{-}Al_2O_3$ which was the final phase that can be formed.

A high transformation temperature always results in the coarsening of particles and formation of large agglomerates in the powder. Thus, a reduction in the $\theta\text{-}Al_2O_3$ to $\alpha\text{-}Al_2O_3$ transformation temperature is crucial for the processing of ultrafine $\alpha\text{-}Al_2O_3$

microstructure. Therefore, monitoring the sintering profile of $SP_{1\text{-}1}$ and $SS_{1\text{-}1}$ during the HP process can offer useful information about the Al_2O_3 phase transformation temperatures which probably affect the final microstructures.

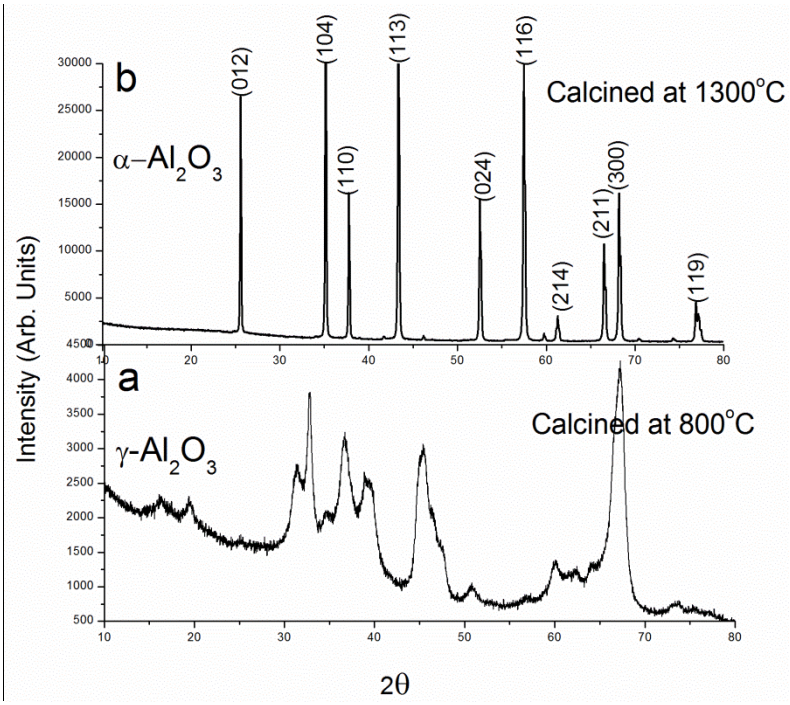

Fig. 7.9 XRD patterns of calcined AlOOH. (a) 800 °C for 5 h resulted in γ- Al_2O_3, and (b) 1300 °C for 5 h resulted in α-Al_2O_3.

Fig. 7.10 shows the sintering profiles of $SP_{1\text{-}1}$ and $SS_{1\text{-}1}$. The black and blue graphs are related to the speed of piston travel or volume shrinkage rate in $SP_{1\text{-}1}$ and $SS_{1\text{-}1}$ respectively, while the red graph shows the heating regime during the sintering process. The shrinkage rate profiles in both $SP_{1\text{-}1}$ and $SS_{1\text{-}1}$ show two peaks. The first peak is attributed to the phase transformation of Al_2O_3 from θ→α phase. As mentioned earlier, in contrast to other polymorphic changes in Al_2O_3 during heating up, the θ→α transformation is a reconstructive form and it caused changes in volume or piston travel speed. The second peak is related to the sintering process which occurred during dwelling period.

A very interesting phenomenon is that the θ→α transformation in $SS_{1\text{-}1}$ occurred at lower temperature (~1200 °C) compared with $SP_{1\text{-}1}$ (~1420 °C). Therefore, the reduction of around 220 °C in the θ-Al_2O_3 to α-Al_2O_3 transformation temperature should be the reason for the grain refinement in $SS_{1\text{-}1}$ (Fig. 7.7). The lower transformation temperature from θ-Al_2O_3 to α-Al_2O_3 is indicative of a lower activation

energy needed for this phase change, meanwhile it limits the grain growth during the transformation stage.

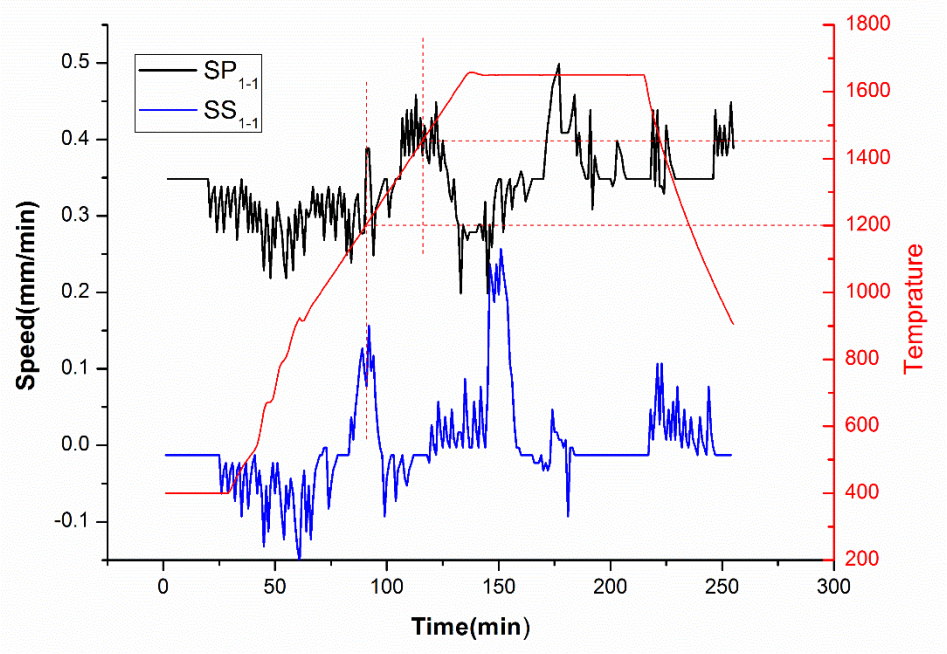

Fig. 7.10 Shrinkage rate profiles of samples SP_{1-1}(black graph) and SS_{1-1} (blue graph). The red graph shows the temperature regime during HP sintering.

As the AlOOH was used in the SS_{1-1}, the existence of highly dispersive GONTs may have acted as heterogeneous nucleation sites, and reduced the activation energy for θ→α phase transformation via lowering the transformation temperature, thus refined the grains. In another word, seeding AlOOH on the GONT reinforcements probably changed the kinetics of the θ-Al_2O_3 to α-Al_2O_3 transformation *via* destroying the normal arrangement of atoms, and producing an highly disordered structure in the lattice of transition Al_2O_3 powders. Such reduction in activation energy was reported previously by using AlOOH gels seeded by α-Al_2O_3 for producing fine grained Al_2O_3[206]. The width of the shrinkage rate peaks is also reduced in SS_{1-1} compared with SP_{1-1}, which indicates a faster θ→α transformation and sintering process in the SS_{1-1}.

7.5 Effect of the GONT content on the grain size and microstructures of Al_2O_3-rGONT composites prepared by sol-gel

As the initial sol-gel process resulted in grain growth retardation and excellent GONT distributions in the SS_{1-1}, further Al_2O_3-rGONT nanocomposites with various GO/CNT

contents were prepared by this technique, to optimize the GONT contents in the matrix. Fig. 7.11a-h shows the thermally etched surfaces (left column) and the fractured surfaces (right column) of the resulting Al_2O_3-rGONT nanocomposites with various GO/CNT ratios. Fig. 7.12 shows the grain size values of the samples shown in Fig. 7.10.

As shown in Figs. 7.11 and 7.12, there is a remarkable reduction in the grain size of $SS_{1\text{-}1}$, reduced to 1.45 μm and equivalating to a 74% reduction than $SS_{0\text{-}0}$, which was discussed in section 7.5, whilst the grain sizes of samples $SS_{1\text{-}2}$ and $SS_{2\text{-}4}$ are very close to $SS_{1\text{-}1}$ with only small increments (Fig. 7.12). On the other hand, the fractured surfaces of $SS_{1\text{-}1}$ and $SS_{1\text{-}2}$ (Fig. 7.11d and f) showed highly dispersed GONTs in the Al_2O_3 matrix, with a mixture of the inter- and trans-granular fracture mode. This result again indicates very good grain boundary strengths in the composites, in contrast with $SS_{0\text{-}0}$ which showed mostly trans-granular fracture mode (Fig. 7.11b). At high rGONT content in $SS_{2\text{-}4}$, severe agglomerations did occur (white circles), due to difficulties in dispersing the rGONTs uniformly, therefore the effective dispersion sites at this high content may not be higher than that of $SS_{1\text{-}1}$, and as a result, slight grain size increments were observed (Fig. 7.12). Based on these results, $SS_{1\text{-}1}$ seems to have the better microstructural characteristics than other hybrid combinations for the Al_2O_3-rGONT nanocomposites. The roles of GONTs in mechanical properties of Al_2O_3-rGONT nanocomposites will be discussed in Section 7.7.

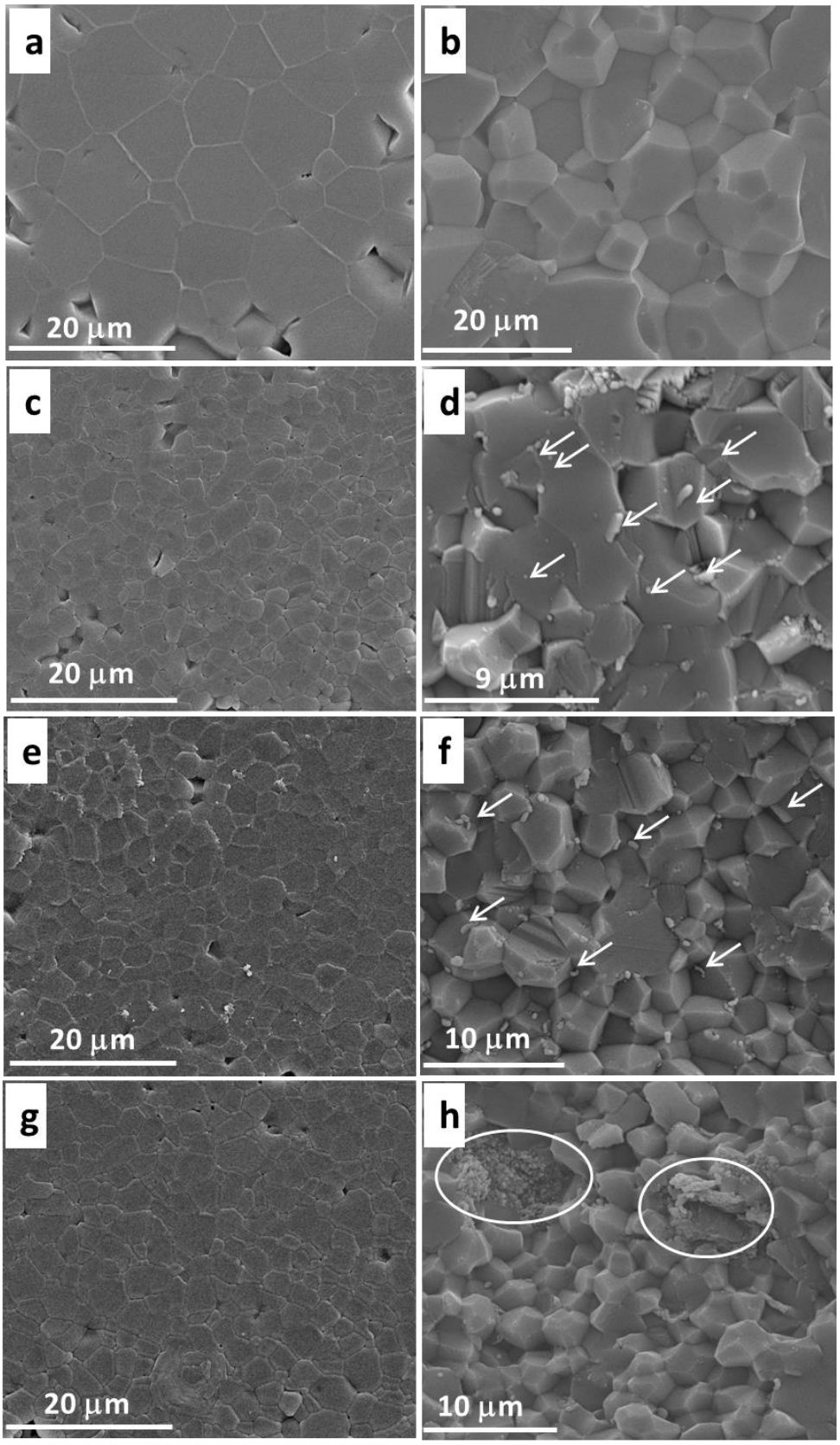

Fig. 7.11 SEM images of thermally etched surfaces (left column) and fractured surfaces (right column) of $SS_{0\text{-}0}$ (a and b), $SS_{1\text{-}1}$ (c and d), $SS_{1\text{-}2}$ (e and f) and $SS_{2\text{-}4}$, (g and h).

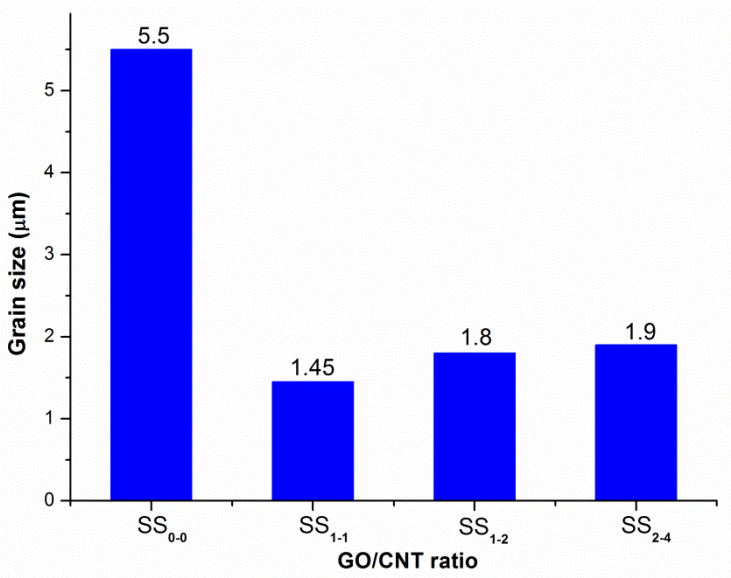

Fig. 7.12 Grain size values of $SS_{0\text{-}0}$, $SS_{1\text{-}1}$, $SS_{1\text{-}2}$ and $SS_{2\text{-}4}$.

7.6 Fabrication of $S_{0.5\text{-}1}$ nanocomposites by sol-gel process

Our previously synthesized $S_{0.5\text{-}1}$ contains 0.5 wt% GNP and 1 wt% CNT. This sample showed the most improved mechanical properties, so it is of great interest to go beyond the GONTs, by applying the sol-gel process back to the GNT samples, to investigate the effect of Al_2O_3 starting phase on microstructure and mechanical properties. Synthesis conditions were chosen according to our previously experiments and the new Al_2O_3–GNT composites prepared from powder possessing and sol-gel are named as $S^P_{0.5\text{-}1}$ and $S^S_{0.5\text{-}1}$, respectively (Table 7.2).

Table 7.2 Material specifications for the preparation of Al_2O_3-GNP composites

Sample ID	Matrix	GNP (wt%)	CNT (wt%)	Synthesis procedure	Density
$S^P_{0.5\text{-}1}$	γ-Al_2O_3	0.5	1	HP	99.9
$S^S_{0.5\text{-}1}$	AlOOH	0.5	1	HP	99.9

The grain size was reduced considerably in $S^S_{0.5\text{-}1}$ compared with $S^P_{0.5\text{-}1}$, as shown from the thermally etched surfaces (Fig. 7.12a and c). The GNT contents are identical in both samples, but only the source of Al_2O_3 as starting materials was changed. Such differences in grain size are thus down to the two different factors arising from the sol-

gel process. One is the reduction in θ-Al_2O_3 to α-Al_2O_3 transformation temperature when using AlOOH which led to grain refinements as discussed in Section 7.4.1. The other is even better dispersion of the GNTs in the $S^S_{0.5\text{-}1}$ matrix than in $S^P_{0.5\text{-}1}$, as exhibited in the fractured surfaces (Fig. 7.13b and d). In the fractured surfaces of $S^P_{0.5\text{-}1}$, the GNP agglomerates are larger than GNPs in $S^S_{0.5\text{-}1}$. Better dispersion of GNTs in finer Al_2O_3 grains (Fig. 7.13.d) leads to more GNPs locating around the grain boundary areas, preventing the grain growth and refining the matrix structures.

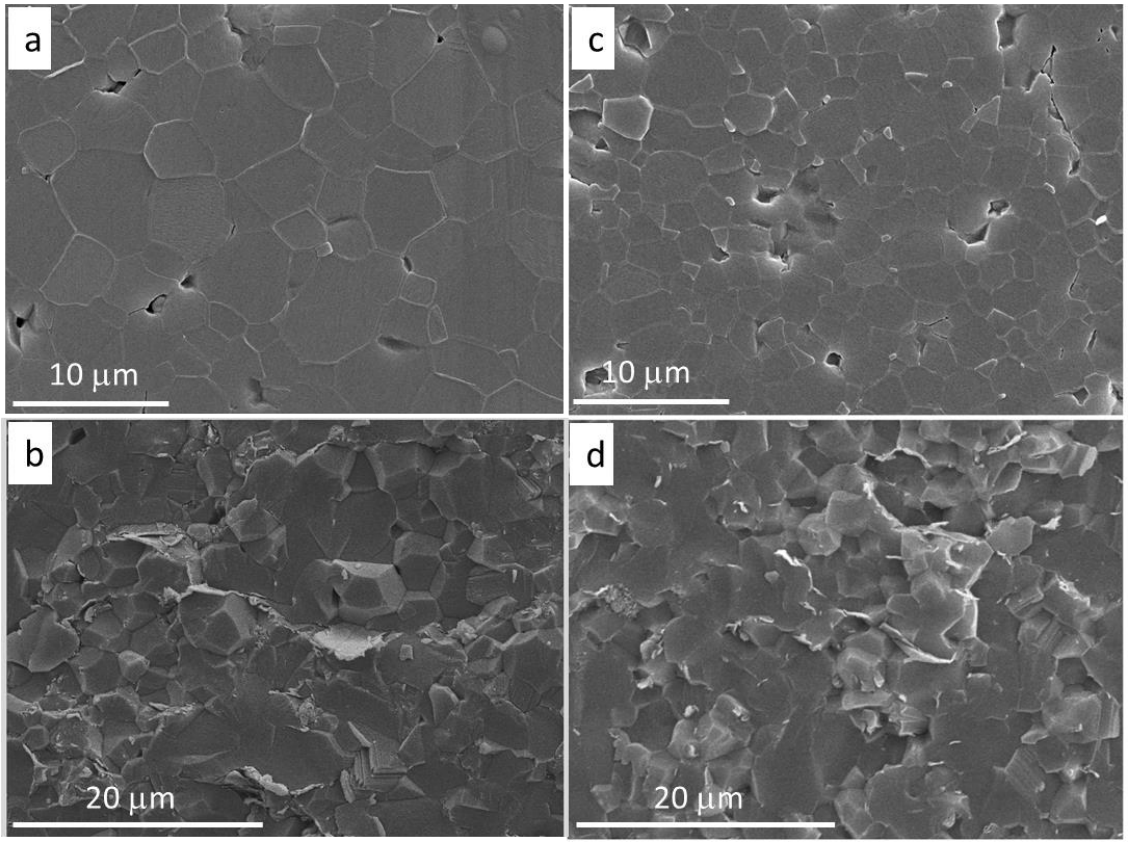

Fig. 7.13 Thermally etched and fractured surfaces of $S^P_{0.5\text{-}1}$ (a and b), and thermally etched and fractured surfaces of $S^S_{0.5\text{-}1}$ (c and d).

7.7 Mechanical properties of Al_2O_3-rGONT nanocomposites

7.7.1 Hardness

Having compared the hardness results with the grain sizes, we realise that there is a direct relationship between the improved hardness and grain size refinements in the Al_2O_3-rGONT nanocomposites. For instance, $SP_{0.5\text{-}0.5}$ and $SP_{1\text{-}1}$ in Fig. 7.14 reveals slight improvements in the hardness against the pure Al_2O_3, which are in consistent with grain refinement results in these nanocomposites, as shown in Fig. 7.5. The hardness improved up to 6% from 16 GPa in $SP_{0\text{-}0}$ to 16.93 GPa in $SP_{1\text{-}1}$, however a further increment to 18.67 GPa in the $SS_{1\text{-}1}$ by 13% was obtained, as shown in Fig. 7.15. These results are in accordant with the stronger grain growth retardation in the sol-gel process for $SS_{1\text{-}1}$ than the standard wet-mixing process for $SP_{1\text{-}1}$ (Fig. 7.8). Therefore, this is a direct evidence for the sol-gel process to improve the dispersion, refine the grain sizes in the microstructures and thus increase the mechanical properties for the Al_2O_3-rGONT nanocomposites.

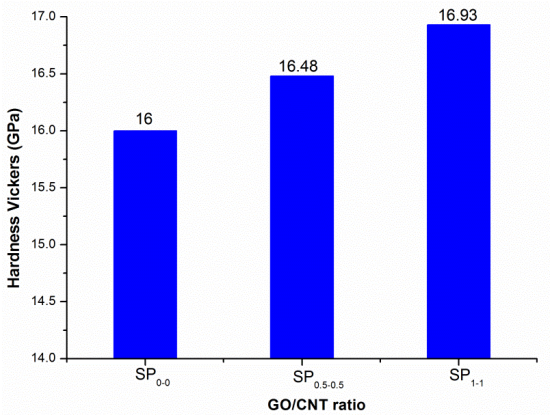

Fig. 7.14 Vickers hardness values for Al_2O_3-rGONT nanocomposites prepared by powder processing at different GO/CNT ratios.

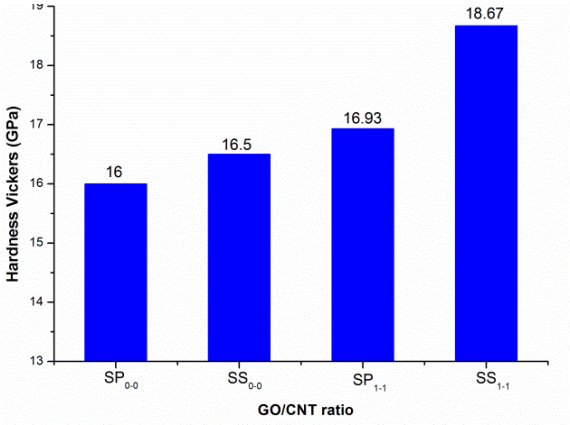

Fig. 7.15 Vickers hardness values for SP_{1-1} and SS_{1-1} nanocomposites prepared by powder processing and sol-gel respectively.

The relationship between hardness and grain size can be accounted for according to the classical grain boundary strengthening theory[189,207]. Grain boundaries act as pinning points impeding dislocation movement across grains. Impeding such dislocation movement hinders the onset of plasticity and makes fine-grained materials stronger and harder. The linear relationship between hardness and inverse of grain-size known as Hall–Petch relation, which has recently been extended to the brittle material regime[208,209].

Regarding ceramic composites, the condition of the reinforcement phase including its hardness, content, orientation and dispersion will affect the hardness of the composite. For example, in the Vickers hardness graphs of the Al_2O_3-GONT nanocomposites with various GONT contents prepared by sol-gel technique (Fig. 7.16), the hardness value showed considerable drops in SS_{1-2} and SS_{2-4} by 6% and 18%, compared with SS_{1-1} respectively. This is due to the soft nature of rGONT reinforcement and their locations in the grain-boundaries. The presence of a relatively soft phase rGONT at the grain boundaries of Al_2O_3 eases the penetration of diamond indenter during indentations. This effect is more dominant in the higher rGONT composites (SS_{1-2} and SS_{2-4}) than in lower content rGONTs, due to more agglomerated reinforcement existed in grain boundaries that nullifies the effect of fine alumina grains and reduces the hardness, compared with SP_{1-1} (Fig. 7.16). However SS_{1-1} showed a maximum hardness value between other Al_2O_3-rGONT nanocomposites with a 14% improvement reaching up to 18.67 GPa.

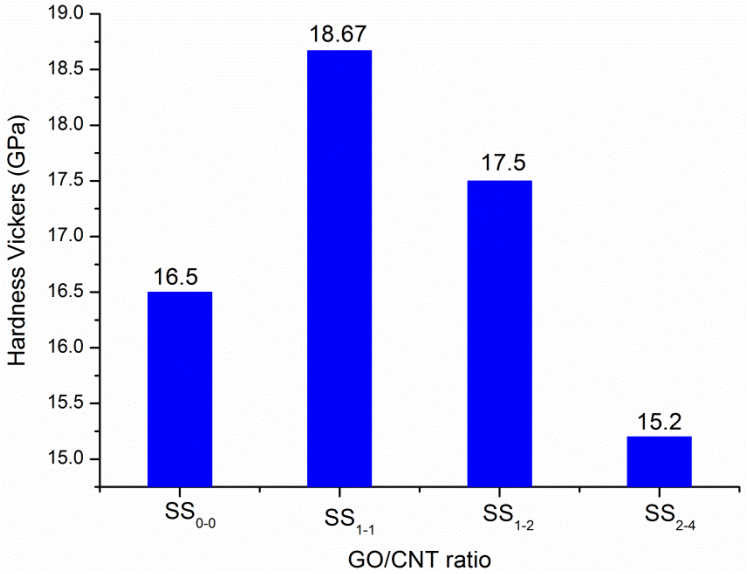

Fig. 7.16 Vickers hardness values for Al_2O_3-rGONT nanocomposites prepared by sol-gel at different GO/CNT ratios.

7.7.2 Fracture toughness and flexural strenght in Al_2O_3-rGONT nanocomposites

Fig. 7.17 shows the fracture toughness and flexural strengths of the Al_2O_3-rGONT nanocomposites prepared by powder processing ($SP_{0.5-0.5}$ and SP_{1-1}). The fracture toughness and flexural strength reached to 5.4±5 $MPa.m^{1/2}$ and 370±5 MPa in SP_{1-1}, demonstrating a 54% and 3% improvement against the pure Al_2O_3 respectively, which is in consistent with the hardness improvement for the composites (Fig. 7.14)

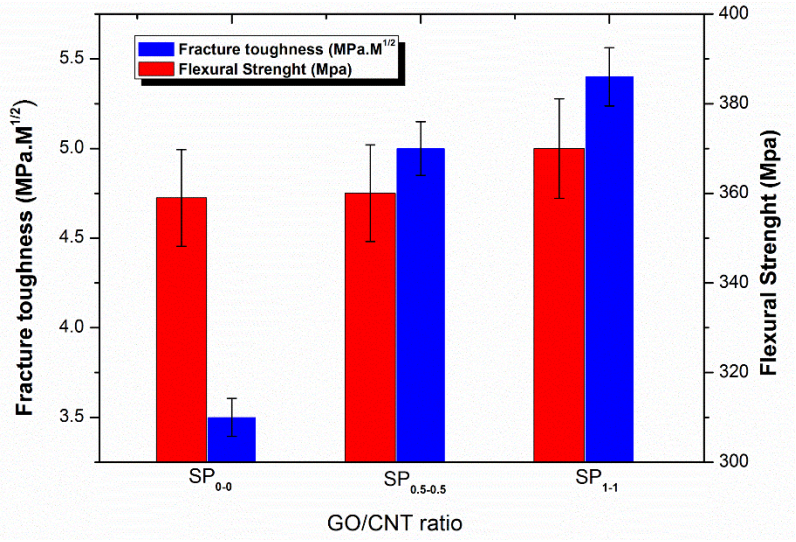

Fig. 7.17 Fracture toughness and flexural strength values of the Al_2O_3-rGONT nanocomposites prepared by powder processing at various GO/CNT ratios.

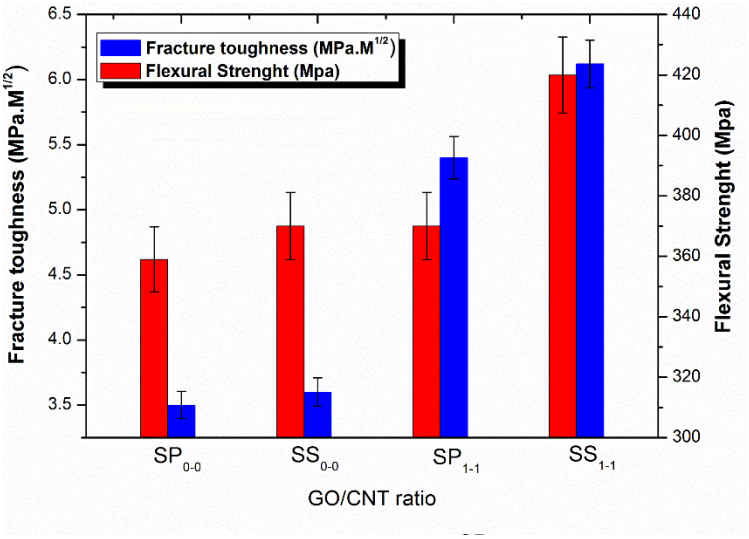

Fig. 7.18 Fracture toughness and flexural strength values for Al_2O_3-rGONT nanocomposites prepared by powder processing and sol-gel respectively.

In Fig. 7.18, the fracture toughness and flexural strength of Al_2O_3-rGONT nanocomposites prepared by powder processing have been compared with the samples prepared by sol-gel processing (SP_{1-1} and SS_{1-1}). With the same amounts of rGONT content, SS_{1-1} showed a significant improvement in the fracture toughness by up to 70%, benchmarked against SS_{0-0}, and up to 14% against SP_{1-1}. The same trend happened in the flexural strength of SS_{1-1}, with 14% and 13% increments against SS_{0-0} and SP_{1-1} respectively. With the remarkable grain size refinement in SS_{1-1} (Figs. 7.7 and 7.8) and hardness improvement of SS_{1-1} (Fig. 7.15), such improvement in fracture toughness and flexural strength was completely expected for SS_{1-1}. The existence of highly dispersed GONTs in the AlOOH gel allowed for heterogonous nucleation sites in the SP_{1-1}, which affected the phase transformation temperature of Al_2O_3, refined the grains in the matrix and led to improvement in the mechanical properties. However, the role of GONT reinforcement and their synergetic effect in all of these should not be neglected even for composites prepared by powder processing. The SP_{1-1} nanocomposite produced with the powder method also showed considerable improvements in the hardness, fracture toughness and flexural strength, than the SP_{0-0} (Figs. 7.14 and 7.17). Therefore, both the hybrid rGONT reinforcement and the sol-gel strategies resulted in largely improved mechanical properties.

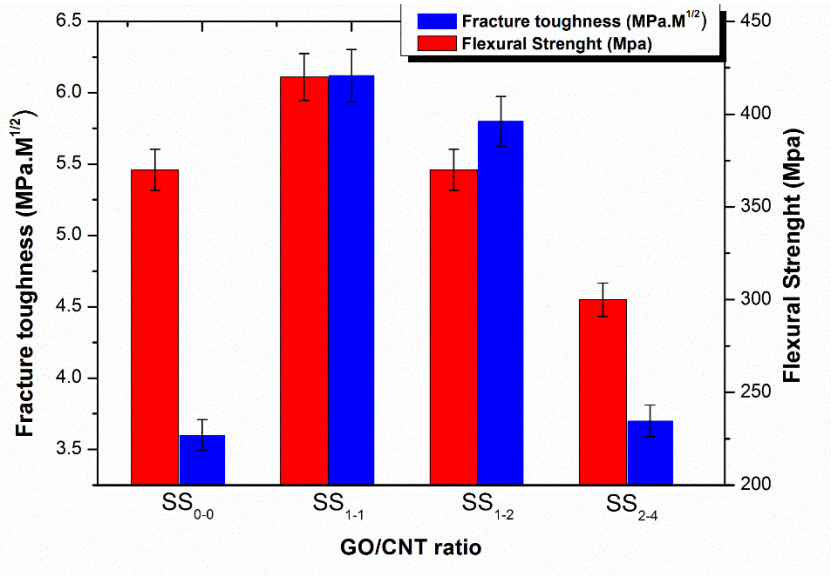

Fig. 7.19 Fracture toughness and flexural strength values for Al_2O_3-rGONT nanocomposites prepared by sol-gel at various GO/CNT ratios.

Fig. 7.19 shows the fracture toughness and flexural strength of Al_2O_3-rGONT nanocomposites prepared by sol-gel with various GO/CNT ratios (SS_{1-1}, SS_{1-2} and SS_{2-4}). Similar to their hardness results in Fig. 7.16, the fracture toughness and flexural strength in SS_{1-2} and SS_{2-4} dropped from SS_{1-1}, due to difficulties in dispersion of high content of rGONT reinforcement (Fig. 7.19). The optimum condition was attributed to SS_{1-1} with the fracture toughness value of 6.12±5 MPa·$M^{1/2}$ against 3.6±5 MPa·$M^{1/2}$ for SS_{0-0}, a 70% improvement.

Comparison of the mechanical property results of Al_2O_3-rGONT nanocomposites with Al_2O_3-GNT nanocomposites is presented in Fig. 7.20. The fracture toughness and flexural strength of SS_{1-1} has 70% and 14% improvements than SS_{0-0} respectively, which even marginally outperformed the previously reported optimised Al_2O_3-GNT nanocomposite ($S_{0.5-1}$) by 8% and 2% respectively (Fig. 7.20). These improvements confirm the successful strategy of applying the cheaper GONT hybrid as reinforcement in the composite fabrication. Due to the synergetic interaction between the GO and CNTs, a better dispersion in the AlOOH matrix leads to enhanced grain refinements, which are the key to achieve improved mechanical properties in CMCs.

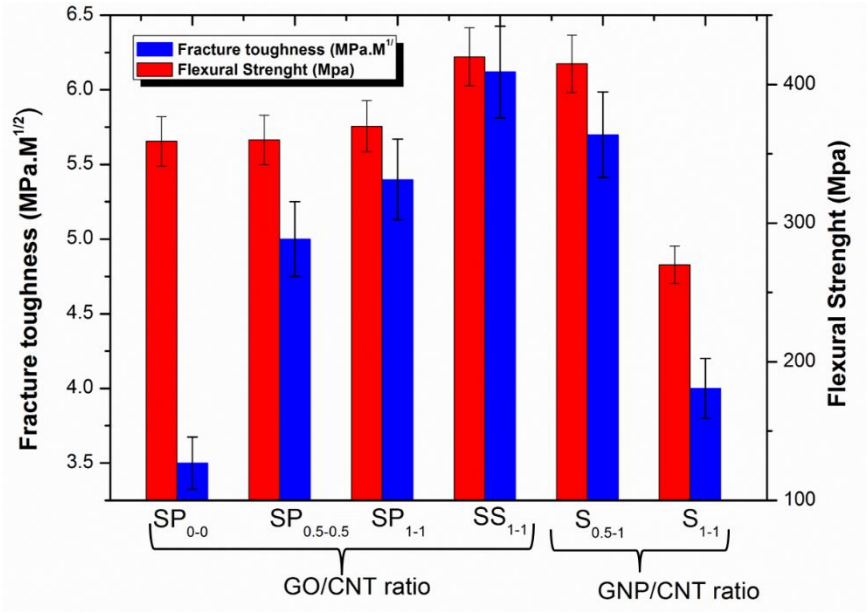

Fig. 7.20 A comparison of the fracture toughness and flexural strength values for Al_2O_3-rGONT with Al_2O_3-GNP nanocomposites.

7.7.3 Toughening mechanisms in Al_2O_3-GONT nanocomposites

The SEM image from a fractured surface of $SS_{1\text{-}1}$ in Fig. 7.21a shows a mixture of inter-granular and trans-granular fracture mode, indicating good strength in grain-boundaries. It is well-known that GO flakes undergoes to partially reduction in Ar atmosphere and produce reduced GO (rGO) according to literature[210]. Higher magnification image from $SS_{1\text{-}1}$ (Fig. 7.21b) shows that the rGONT preferred locations are not only in the grain-boundaries. The rGONTs are highly dispersed and embedded within the Al_2O_3 matrix (white arrows), causing smooth glaze-like trans-granular fractures in areas.

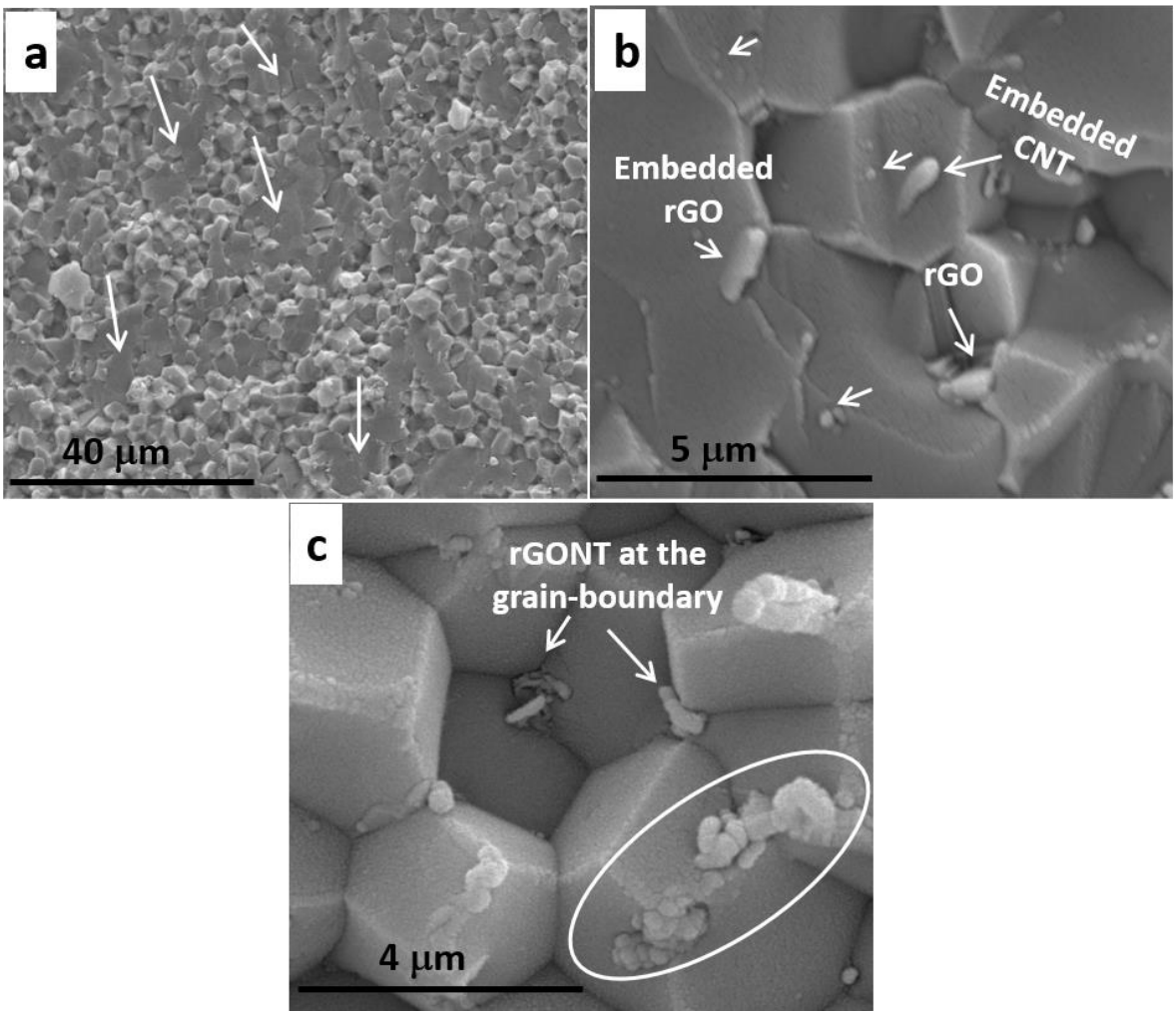

Fig. 7.21 SEM images of fractured surface of $SS_{1\text{-}1}$. (a) Low magnification, (b and c) high magnification.

Embedded CNTs between the grains in Fig. 7.21c indeed pinned the Al_2O_3 grains together and strengthened the grain boundaries, leading to the changed fracture mode from inter-granular to trans-granular in the nanocomposites. Additionally, the existence of rGONTs at the grain-boundaries formed a strong entangled network around the grains, which constrained the grain growth and controlled the microstructure, as shown in Fig. 7.8.

During the crack propagation, large rGO flakes pulled-out form the matrix (Fig. 7.22a and b), which must have absorbed a considerable amount of energy during the fracture process, hence improved the toughness. However the interesting anchoring which is specifically applicable to 2D flexible structure can be seen in Fig. 7.22d. In such anchoring, the rGO could form large areas of interface with the matrix, leading to

increased interfacial frictions during for the reinforcement pulling out. This similar anchoring mechanism was also applied to the Al_2O_3-GNP nanocomposites, as discussed in Chapter 5.

Well-dispersed CNTs played an important role in the toughening by pull-outs (Fig. 7.22d) and via bridging the grains (Fig. 7.22c), due to their higher aspect ratios than rGO. But CNT bundles located within the grain boundaries are more dominant in pining the grains and in the grain size reduction, as discussed in section 7.3 (CNT bundles are circled in Fig. 7.20d and Fig. 7.22c).

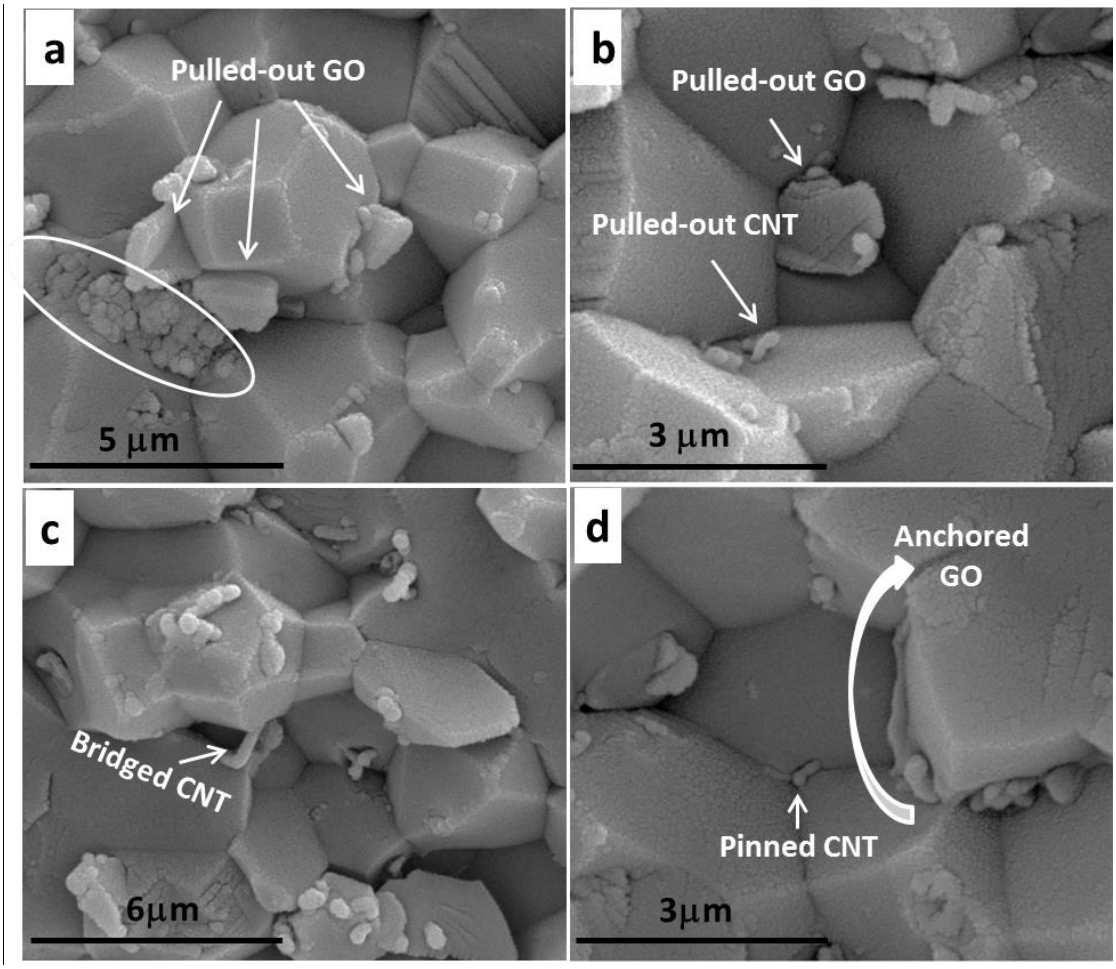

Fig. 7.22 SEM images from fractured surface of $SS_{1\text{-}1}$ in high magnification showing pulled-out rGO and CNT from Al_2O_3 grains (White arrows in a and b), Bridging CNT within Al_2O_3 grains (c) and Anchored rGO (d).

7.8 Conclusion

In this chapter, new Al_2O_3-rGONT nanocomposites were prepared using rGONTs as the hybrid reinforcement (a blend of GO and CNT), via two different mixing techniques (powder processing and sol-gel processing). The microstructural features and mechanical properties of the resulting composites have been compared with each other, benchmarked against the previously prepared Al_2O_3-GNT nanocomposites. SEM studies from thermally etched surfaces have showed that there is a remarkable 62% grain size reduction in the $SS_{1\text{-}1}$ (prepared by sol-gel), compared with $SP_{1\text{-}1}$ (prepared by powder processing). The AlOOH used in the sol-gel process went through phase transformations during sintering to form the final stable α-Al_2O_3 phase in the composites. The rGONT reinforcements are believed to act as heterogeneous nucleation sites to reduce the activation energy of and temperature required for the phase transformations, promoting the grain size refinements of the Al_2O_3. Meanwhile, the hardness, fracture toughness and flexural strength of the Al_2O_3-rGONT nanocomposites prepared by sol-gel ($SS_{1\text{-}1}$) are increased by 13%, 70% and 14% respectively, against the pure Al_2O_3. Additionally, the $SS_{1\text{-}1}$ composite even showed a 8% improvement in the fracture toughness than our previously prepared Al_2O_3-GNT nanocomposites ($S_{0.5\text{-}1}$), which demonstrates the successful development of our fabrication strategy in choosing hybrid rGONT reinforcements combined with the sol-gel process.

Chapter 8 Conclusion

In conclusion, Al_2O_3-GNT (a blend of GNP and CNT) nanocomposites have been fabricated using Hot-Pressing (HP) and Spark Plasma Sintering (SPS) techniques. The effect of carbon content and fabrication method on structural features, mechanical properties, tribology and wear properties of the nanocomposites were thoroughly investigated. Then, GONT hybrid reinforcement (a blend of GO and CNT) was applied instead of GNT into the Al_2O_3, and influence on the microstructure and mechanical properties of the resulting Al_2O_3-GONT was investigated.

Well-dispersed GNT within the Al_2O_3 matrix have been achieved successfully via a combined approach using wet chemical method and probe-sonication. HP and SPS have both been proven to be an effective technique for the fabrication of GNT-reinforced Al_2O_3 nanocomposites, and the GNT reinforcements remained undamaged during sintering process. Highly densified Al_2O_3-GNT nanocomposites with improved mechanical properties have been obtained at low GNT additions.

The effect of the GNP to CNT ratios on microstructural features and mechanical properties were investigated. The additions of GNT in Al_2O_3 matrix altered the fracture mode from inter-granular to trans-granular by strengthening the matrix grain boundaries and increased the relative densities in low GNT additions however, a gradual drop in the relative densities of nanocomposites with raising GNT concentrations was frequently observed, due to the hampering of the densification process by GNTs. At a hybrid addition of 0.5 wt% GNPs and 1 wt% CNTs, i.e. for $S_{0.5\text{-}1}$, the average fracture toughness of the nanocomposites reached up to 5.7 $MPa{\cdot}m^{1/2}$, against 3.5 $MPa{\cdot}m^{1/2}$ of the plain alumina, and the flexural strength improved from 360 MPa to 424 MPa. The fractured surface studies showed that CNTs and GNPs have played different roles in improving the fracture toughness, due to their different microstructures: GNPs increasing the required pull-out energy during fracture by anchoring around the Al_2O_3 grains and producing higher contact area with grains; whist CNTs bridging the grains due to their higher aspect ratio.

Reduced friction coefficients and improved wear resistance for the nanocomposites have been concluded in composites with low GNT contents at various loads. In particular, for low (15N) sliding loads, samples designated as $S_{0.5\text{-}0}$ and $S_{0.3\text{-}1}$ showed a remarkable 70% and 86% reduction in the wear rates and 23% and 20% reduction in COF values, respectively, against the pure Al_2O_3. The tribological properties have been improved by the indirect (change of microstructure and mechanical properties) and direct roles (acting as lubrication material) of the GNTs in the nanocomposites. It was identified that the superior mechanical traits of the $S_{0.5\text{-}0}$ and $S_{0.3\text{-}1}$ samples, in term of fracture toughness, against pure Al_2O_3 and the formation of a protective tribofilm on the wear track are the effective wear mechanisms for converting Al_2O_3-GNT composites into wear resistant materials. The CNTs played a vital indirect role in the former, whilst GNPs contributed directly to the latter tribofilm formation which is more dominant for the reduced COF.

Two new strategies have been applied to obtain further improvements in composites. One is replacing powder processing (Al_2O_3) with sol-gel (AlOOH) and the other is using a hybrid GONT reinforcement [a blend of graphite oxide (GO) and carbon nanotube (CNT)) instead of GNT reinforcement to fabricate Al_2O_3-GONT nanocomposites. Combining these strategies resulted in intensive grain refinement in Al_2O_3-GONT nanocomposites prepared by sol-gel and further improvement in mechanical properties. Although using the same GONT content, there is a further 62% grain size refinement in Al_2O_3-GONT nanocomposite prepared by sol-gel than the similar ones prepared by powder processing. The existence of GONT in AlOOH matrix probably effected the kinetic of phase transformation behaviour of Al_2O_3 during sintering process. In another words, highly dispersed GONT in Al_2O_3-GONT prepared by the sol-gel method act as heterogeneous nucleation sites and reduced the activation energy and temperature of phase transformations in Al_2O_3 phases and refined the grains. Accordingly, fracture toughness and flexural strength of Al_2O_3-GONT composites prepared by sol-gel method at low GONT additions are found to increase by 70% and 14% than the pure Al_2O_3 respectively. Al_2O_3-GONT composites of the same GONT contents but prepared using different mixing technique (powder processing and sol-gel) revealed that the fracture toughness and flexural strength increased by 14% and 13% respectively in the latter.

Based on these results, it can be finally concluded that these newly developed novel hybrid composites possessing promising toughness and tribological performance, could extend their applications to many new fields as advanced structural materials, protective coatings for micro-mechanical systems and contact-damage-resistant components.

Suggestions for future work

Base on the obtained results, some suggestions are recommended for future work as follows.

- To take graphene and related materials from the lab, eventually, to the point where it can be considered for application in industry is the main mission for all scientific communities dealing with graphene. Graphene related composites seem to be the most possible areas which can fulfil this goal in a near future. Accordingly integrating graphene into other host materials ranging from non-oxide and oxide ceramics to polymers, glasses and metals is highly recommended with the aim of augmenting the mechanical, thermal, optical, or electronic properties of the host material.

- Preparing Al_2O_3-GNT nanocomposites with high GNT contents with improved level of dispersion within Al_2O_3 matrix, to fabricate interconnected GNT networks in the Al_2O_3 matrix. Such 3D-GNT networks in a ceramic matrix can considerably improve mechanical properties, particularly its fracture toughness, while tailoring more functionalized properties such as improved electrical properties which can widen CMC applications in advanced engineering areas.

- In-depth investigations of GNT/Al_2O_3 matrix interface will be interesting. For this purpose advanced analytical techniques for sample preparation (focused ion beam-SEM) and characterisation (FEG-TEM) equipment could be utilised. The elemental composition mapping at nanoscale (using EDX or EELS (electron energy loss spectroscopy) could be helpful in predicting the possible interaction of GNT with matrix at interface.

- For structural applications, ceramic matrix could be a promising candidate after reinforcement with GNT for bearings, seals, armour, liners, nozzles and cutting tools. Improved fracture toughness by crack bridging of CNT could also lead to other exciting properties, such as electrical and thermal conductivities that could

be exploited in a number of applications. Based on their high thermal conductivity, GNT-reinforced ceramic nanocomposites are attractive for aerospace applications particularly rocket nozzles and components of jet engine and brake disks for commercial and military aircrafts. High thermal and electrical characteristics of these nanocomposites can also be exploited in the aerospace and automobile industry in particular knock sensors, seat pressure sensors, temperature sensors, oil sensors, impact sensors and road surface sensors. Whilst the outstanding electrical properties of GNT can make Al_2O_3 nanocomposites attractive for specific functional applications like heating elements, electrical igniters, electromagnetic and antistatic shielding of electronic components.

References

1 Liu, B. Q., Huang, C. Z. & Sun, A. L. Toughening Mechanisms and Wear Behavior of a TiC Whisker Toughening Alumina Ceramic Cutting Tool Composite. *Advanced Materials Research* **500**, 634-639 (2012).

2 Mozalev, A., Sakairi, M., Takahashi, H., Habazaki, H. & Hubálek, J. Nanostructured anodic-alumina-based dielectrics for high-frequency integral capacitors. *Thin Solid Films* (2012).

3 Martin, C. A., Lee, G. F. & Fedderly, J. J. (US Patent 8,387,510, 2013).

4 Ighodaro, O. L. & Okoli, O. I. Fracture toughness enhancement for alumina systems: a review. *International Journal of Applied Ceramic Technology* **5**, 313-323 (2008).

5 Wu, Y.-q., Zhang, Y.-f., Huang, X.-x. & Guo, J.-k. Microstructural development and mechanical properties of self-reinforced alumina with CAS addition. *Journal of the European Ceramic Society* **21**, 581-587 (2001).

6 Ohnabe, H., Masaki, S., Onozuka, M., Miyahara, K. & Sasa, T. Potential application of ceramic matrix composites to aero-engine components. *Composites Part A: Applied Science and Manufacturing* **30**, 489-496 (1999).

7 Trusty, P. & Yeomans, J. The toughening of alumina with iron: effects of iron distribution on fracture toughness. *Journal of the European Ceramic Society* **17**, 495-504 (1997).

8 Lin, C.-J., Yang, C.-C. & Wei, W.-C. J. Processing and microstructure of Nano-Mo/Al_2O_3 composites from MOCVD and fluidized bed. *Nanostructured materials* **11**, 1361-1377 (1999).

9 Chmielewski, M. & Pietrzak, K. Processing, microstructure and mechanical properties of Al_2O_3–Cr nanocomposites. *Journal of the European Ceramic Society* **27**, 1273-1279 (2007).

10 Yao, X. *et al.* Alumina–nickel composites densified by spark plasma sintering. *Materials letters* **59**, 2314-2318 (2005).

11 Dogam, C. & Hawk, J. Role of zirconia toughening in abrasive wear of intermetallic and ceramics composites. *Wear* **212**, 110-118 (1997).

12 Chakravarty, D., Bysakh, S., Muraleedharan, K., Rao, T. N. & Sundaresan, R. Spark Plasma Sintering of Magnesia-Doped Alumina with High Hardness and Fracture Toughness. *Journal of the American Ceramic Society* **91**, 203-208 (2008).

13 Carroll, L., Sternitzke, M. & Derby, B. Silicon carbide particle size effects in alumina-based nanocomposites. *Acta Materialia* **44**, 4543-4552 (1996).

14 Hansson, T., Warren, R. & Wasen, J. Fracture Toughness Anisotropy and Toughening Mechanisms of a Hot-pressed Alumina Reinforced with Silicon Carbide Whiskers. *Journal of the American Ceramic Society* **76**, 841-848 (1993).

15 Ostertag, C. P. Influence of fiber and grain bridging on crack profiles in SiC fiber-reinforced alumina-matrix composites. *Materials Science and Engineering: A* **260**, 124-131 (1999).

16 García, D. E., Schicker, S., Bruhn, J., Janssen, R. & Claussen, N. Processing and Mechanical Properties of Pressureless-Sintered Niobium-Alumina-Matrix Composites. *Journal of the American Ceramic Society* **81** (1998).

17 Padture, N. P. Multifunctional Composites of Ceramics and Single-Walled Carbon Nanotubes. *Advanced Materials* **21**, 1767-1770 (2009).

18 Sheldon, B. W. & Curtin, W. A. Nanoceramic composites: tough to test. *Nature materials* **3**, 505-506 (2004).

19 Peigney, A. Composite materials: tougher ceramics with nanotubes. *Nature materials* **2**, 15-16 (2003).

20 Yamamoto, G., Omori, M., Hashida, T. & Kimura, H. A novel structure for carbon nanotube reinforced alumina composites with improved mechanical properties. *Nanotechnology* **19**, 315708 (2008).

21 Fan, J., Zhao, D., Wu, M., Xu, Z. & Song, J. Preparation and Microstructure of Multi-Wall Carbon Nanotubes-Toughened Al2O3 Composite. *Journal of the American Ceramic Society* **89**, 750-753 (2006).
22 Balázsi, C. Silicon nitride composites with different nanocarbon additives. *Journal of the Korean Ceramic Society* **49**, 352-362 (2012).
23 Yamamoto, G., Omori, M., Yokomizo, K., Hashida, T. & Adachi, K. Structural characterization and frictional properties of carbon nanotube/alumina composites prepared by precursor method. *Materials Science and Engineering: B* **148**, 265-269 (2008).
24 Laurent, C., Peigney, A., Dumortier, O. & Rousset, A. Carbon nanotubes–Fe–alumina nanocomposites. Part II: microstructure and mechanical properties of the hot-pressed composites. *Journal of the European Ceramic Society* **18**, 2005-2013 (1998).
25 Zhan, G.-D., Kuntz, J. D., Wan, J. & Mukherjee, A. K. Single-wall carbon nanotubes as attractive toughening agents in alumina-based nanocomposites. *Nature materials* **2**, 38-42 (2002).
26 Siegel, R. *et al.* Mechanical behavior of polymer and ceramic matrix nanocomposites. *Scr. Mater.* **44**, 2061-2064 (2001).
27 Wei, T., Fan, Z., Luo, G. & Wei, F. A new structure for multi-walled carbon nanotubes reinforced alumina nanocomposite with high strength and toughness. *Materials letters* **62**, 641-644 (2008).
28 Novoselov, K. *et al.* Electric field effect in atomically thin carbon films. *Science* **306**, 666-669 (2004).
29 Rao, C., Biswas, K., Subrahmanyam, K. & Govindaraj, A. Graphene, the new nanocarbon. *Journal of Materials Chemistry* **19**, 2457-2469 (2009).
30 Tapasztó, O. *et al.* Dispersion patterns of graphene and carbon nanotubes in ceramic matrix composites. *Chemical Physics Letters* **511**, 340-343 (2011).
31 Ramirez, C., Garzón, L., Miranzo, P., Osendi, M. & Ocal, C. Electrical conductivity maps in graphene nanoplatelet/silicon nitride composites using conducting scanning force microscopy. *Carbon* **49**, 3873-3880 (2011).
32 Kvetkova, L. *et al.* Fracture toughness and toughening mechanisms in graphene platelet reinforced Si_3N_4 composites. *Scr. Mater.* **66**, 793-796 (2012).
33 Ramirez, C., Figueiredo, F. M., Miranzo, P., Poza, P. & Osendi, M. I. Graphene nanoplatelet/silicon nitride composites with high electrical conductivity. *Carbon* **50**, 3607-3615.carbon.2012.03.031 (2012).
34 Walker, L. S., Marotto, V. R., Rafiee, M. A., Koratkar, N. & Corral, E. L. Toughening in Graphene Ceramic Composites. *ACS Nano* **5**, 3182-3190 (2011).
35 Liu, J., Yan, H., Reece, M. J. & Jiang, K. Toughening of zirconia/alumina composites by the addition of graphene platelets. *Journal of the European Ceramic Society*.2012.07.007 (2012).
36 Fan, Y. *et al.* Preparation and electrical properties of graphene nanosheet/Al_2O_3 composites. *Carbon* **48**, 1743-1749 (2010).
37 Shin, M. K. *et al.* Synergistic toughening of composite fibres by self-alignment of reduced graphene oxide and carbon nanotubes. *Nature Communications* **3**, 650 (2012).
38 Stankovich, S. *et al.* Graphene-based composite materials. *Nature* **442**, 282-286 (2006).
39 Kuilla, T. *et al.* Recent advances in graphene based polymer composites. *Progress in Polymer Science* **35**, 1350-1375 (2010).
40 Khan, U., May, P., O'Neill, A. & Coleman, J. N. Development of stiff, strong, yet tough composites by the addition of solvent exfoliated graphene to polyurethane. *Carbon* **48**, 4035-4041 (2010).
41 Layek, R. K., Samanta, S. & Nandi, A. K. The physical properties of sulfonated graphene/poly (vinyl alcohol) composites. *Carbon* **50**, 815-827 (2012).

42 Qiu, L. *et al.* Dispersing carbon nanotubes with graphene oxide in water and synergistic effects between graphene derivatives. *Chemistry-A European Journal* **16**, 10653-10658 (2010).
43 Dong, X. *et al.* The formation of a carbon nanotube–graphene oxide core–shell structure and its possible applications. *Carbon* **49**, 5071-5078 (2011).
44 Chen, S., Yeoh, W., Liu, Q. & Wang, G. Chemical-free synthesis of graphene–carbon nanotube hybrid materials for reversible lithium storage in lithium-ion batteries. *Carbon* **50**, 4557-4565 (2012).
45 Cheng, Y., Lu, S., Zhang, H., Varanasi, C. V. & Liu, J. Synergistic effects from graphene and carbon nanotubes enable flexible and robust electrodes for high-performance supercapacitors. *Nano Letters* **12**, 4206-4211 (2012).
46 Sui, Z., Meng, Q., Zhang, X., Ma, R. & Cao, B. Green synthesis of carbon nanotube–graphene hybrid aerogels and their use as versatile agents for water purification. *Journal of Materials Chemistry* **22**, 8767-8771 (2012).
47 Evans, A. G. Perspective on the development of high-toughness ceramics. *Journal of the American Ceramic Society* **73**, 187-206 (1990).
48 Poser, K., Zum Gahr, K.-H. & Schneider, J. Development of Al_2O_3 based ceramics for dry friction systems. *Wear* **259**, 529-538 (2005).
49 Lim, D.-S., You, D.-H., Choi, H.-J., Lim, S.-H. & Jang, H. Effect of CNT distribution on tribological behavior of alumina–CNT composites. *Wear* **259**, 539-544 (2005).
50 Kim, H. J. *et al.* Unoxidized Graphene/Alumina Nanocomposite: Fracture-and Wear-Resistance Effects of Graphene on Alumina Matrix. *Scientific Reports* **4** (2014).
51 Niihara, K. New design concept of structural ceramics—ceramic nanocomposites. *Nippon seramikkusu kyokai gakujutsu ronbunshi* **99**, 974-982 (1991).
52 Palmero, P. Structural Ceramic Nanocomposites: A Review of Properties and Powders' Synthesis Methods. *Nanomaterials* **5**, 656-696 (2015).
53 Iijima, S. Helical microtubules of graphitic carbon. *Nature* **354**, 56-58 (1991).
54 Falvo, M. *et al.* Bending and buckling of carbon nanotubes under large strain. *Nature* **389**, 582-584 (1997).
55 Fan, J.-P. *et al.* Toughening and reinforcing alumina matrix composite with single-wall carbon nanotubes. *Applied physics letters* **89**, 121910-121910-121913 (2006).
56 Wei, T. *et al.* The effect of carbon nanotubes microstructures on reinforcing properties of SWNTs/alumina composite. *Mater. Res. Bull.* **43**, 2806-2809 (2008).
57 Ahmad, I. *et al.* Carbon nanotube toughened aluminium oxide nanocomposite. *Journal of the European Ceramic Society* **30**, 865-873 (2010).
58 Inam, F., Yan, H., Reece, M. J. & Peijs, T. Dimethylformamide: an effective dispersant for making ceramic–carbon nanotube composites. *Nanotechnology* **19**, 195710 (2008).
59 Vasiliev, A. L. & Padture, N. P. Single-wall carbon nanotubes at ceramic grain boundaries. *Scr. Mater.* **56**, 461-463 (2007).
60 Baron, B., Kumar, C., Le Gonidec, G. & Hampshire, S. Comparison of different alumina powders for the aqueous processing and pressureless sintering of Al 2 O 3–SiC nanocomposites. *Journal of the European Ceramic Society* **22**, 1543-1552 (2002).
61 Ritchie, R. O. The quest for stronger, tougher materials. *Science (New York, NY)* **320**, 448; author reply 448-448; author reply 448 (2008).
62 Li, X. *et al.* Large-area synthesis of high-quality and uniform graphene films on copper foils. *Science* **324**, 1312-1314 (2009).
63 Hass, J., De Heer, W. & Conrad, E. The growth and morphology of epitaxial multilayer graphene. *Journal of Physics: Condensed Matter* **20**, 323202 (2008).
64 Dusza, J. *et al.* Microstructure and fracture toughness of Si3N4+graphene platelet composites. *Journal of the European Ceramic Society* **32**, 3389-3397 (2012).

65 Knieke, C. *et al.* Scalable production of graphene sheets by mechanical delamination. *Carbon* **48**, 3196-3204 (2010).
66 Hummers Jr, W. S. & Offeman, R. E. Preparation of graphitic oxide. *Journal of the American Chemical Society* **80**, 1339-1339 (1958).
67 Li, J., Zeng, X., Ren, T. & van der Heide, E. The Preparation of Graphene Oxide and Its Derivatives and Their Application in Bio-Tribological Systems. *Lubricants* **2**, 137-161 (2014).
68 Geim, A. K. & Novoselov, K. S. The rise of graphene. *Nature materials* **6**, 183-191 (2007).
69 Liu, J., Yan, H. & Jiang, K. Mechanical properties of graphene platelet-reinforced alumina ceramic composites. *Ceramics International* (2013).
70 Wang, X., Padture, N. P. & Tanaka, H. Contact-damage-resistant ceramic/single-wall carbon nanotubes and ceramic/graphite composites. *Nature materials* **3**, 539-544 (2004).
71 Sun, J. & Gao, L. Development of a dispersion process for carbon nanotubes in ceramic matrix by heterocoagulation. *Carbon* **41**, 1063-1068 (2003).
72 Mo, C. B., Cha, S. I., Kim, K. T., Lee, K. H. & Hong, S. H. Fabrication of carbon nanotube reinforced alumina matrix nanocomposite by sol–gel process. *Materials Science and Engineering: A* **395**, 124-128 (2005).
73 He, T., Li, J., Wang, L., Zhu, J. & Jiang, W. Preparation and consolidation of alumina/graphene composite powders. *Materials transactions* **50**, 749-751 (2009).
74 Zhan, G.-D., Kuntz, J. D., Garay, J. E. & Mukherjee, A. K. Electrical properties of nanoceramics reinforced with ropes of single-walled carbon nanotubes. *Applied physics letters* **83**, 1228-1230 (2003).
75 Dusza, J. *et al.* Hot pressed and spark plasma sintered zirconia/carbon nanofiber composites. *Journal of the European Ceramic Society* **29**, 3177-3184 (2009).
76 Balázsi, C. *et al.* Processing of carbon nanotube reinforced silicon nitride composites by spark plasma sintering. *Composites Science and Technology* **65**, 727-733 (2005).
77 Balázsi, C., Sedláčková, K. & Czigány, Z. Structural characterization of Si_3N_4–carbon nanotube interfaces by transmission electron microscopy. *Composites Science and Technology* **68**, 1596-1599 (2008).
78 Guo, S., Sivakumar, R., Kitazawa, H. & Kagawa, Y. Electrical Properties of Silica-Based Nanocomposites with Multiwall Carbon Nanotubes. *Journal of the American Ceramic Society* **90**, 1667-1670 (2007).
79 Boccaccini, A., Thomas, B., Brusatin, G. & Colombo, P. Mechanical and electrical properties of hot-pressed borosilicate glass matrix composites containing multi-wall carbon nanotubes. *Journal of Materials Science* **42**, 2030-2036 (2007).
80 Ramirez, C. & Osendi, M. I. Characterization of graphene nanoplatelets-Si< sub> 3</sub> N< sub> 4</sub> composites by Raman spectroscopy. *Journal of the European Ceramic Society* **33**, 471-477 (2013).
81 Chen, Y.-F., Bi, J.-Q., Yin, C.-L. & You, G.-L. Microstructure and fracture toughness of graphene nanosheets/alumina composites. *Ceramics International* **40**, 13883-13889 (2014).
82 Inam, F., Vo, T. & Bhat, B. R. Structural stability studies of graphene in sintered ceramic nanocomposites. *Ceramics International* **40**, 16227-16233 (2014).
83 Inam, F., Bhat, B. R., Vo, T. & Daoush, W. M. Structural health monitoring capabilities in ceramic–carbon nanocomposites. *Ceramics International* **40**, 3793-3798 (2014).
84 Porwal, H. *et al.* Graphene reinforced alumina nano-composites. *Carbon* **64**, 359-369 (2013).
85 Liu, J., Yan, H. & Jiang, K. Mechanical properties of graphene platelet-reinforced alumina ceramic composites. *Ceramics International* **39**, 6215-6221 (2013).
86 O'Neill, A., Khan, U., Nirmalraj, P. N., Boland, J. & Coleman, J. N. Graphene dispersion and exfoliation in low boiling point solvents. *The Journal of Physical Chemistry C* **115**, 5422-5428 (2011).

87 Kun, P., Tapasztó, O., Wéber, F. & Balázsi, C. Determination of structural and mechanical properties of multilayer graphene added silicon nitride-based composites. *Ceramics International* **38**, 211-216 (2012).
88 Duan, W. H., Wang, Q. & Collins, F. Dispersion of carbon nanotubes with SDS surfactants: a study from a binding energy perspective. *Chemical Science* **2**, 1407-1413 (2011).
89 Sun, J., Gao, L. & Li, W. Colloidal processing of carbon nanotube/alumina composites. *Chemistry of Materials* **14**, 5169-5172 (2002).
90 Tkalya, E. E., Ghislandi, M., de With, G. & Koning, C. E. The use of surfactants for dispersing carbon nanotubes and graphene to make conductive nanocomposites. *Current Opinion in Colloid & Interface Science* **17**, 225-232 (2012).
91 Estili, M. & Kawasaki, A. An approach to mass-producing individually alumina-decorated multi-walled carbon nanotubes with optimized and controlled compositions. *Scr. Mater.* **58**, 906-909 (2008).
92 Garmendia, N., Santacruz, I., Moreno, R. & Obieta, I. Slip casting of nanozirconia/MWCNT composites using a heterocoagulation process. *Journal of the European Ceramic Society* **29**, 1939-1945 (2009).
93 Balázsi, C. *et al.* Development of CNT/Si_3N_4 composites with improved mechanical and electrical properties. *Composites Part B: Engineering* **37**, 418-424 (2006).
94 Smith, R. J., Lotya, M. & Coleman, J. N. The importance of repulsive potential barriers for the dispersion of graphene using surfactants. *New Journal of Physics* **12**, 125008 (2010).
95 Wang, K., Wang, Y. F., Fan, Z. J., Yan, J. & Wei, T. Preparation of graphene nanosheet/alumina composites by spark plasma sintering. *Mater. Research Bulletin* **46**, 315-318 (2011).
96 Zhang, Y. *et al.* Reinforcement of silica with single-walled carbon nanotubes through covalent functionalization. *J. Mater. Chem.* **16**, 4592-4597 (2006).
97 Berguiga, L., Bellessa, J., Vocanson, F., Bernstein, E. & Plenet, J. Carbon nanotube silica glass composites in thin films by the sol–gel technique. *Optical Materials* **28**, 167-171 (2006).
98 Chu, B. T. *et al.* Fabrication of carbon-nanotube-reinforced glass–ceramic nanocomposites by ultrasonic in situ sol–gel processing. *Journal of Materials Chemistry* **18**, 5344-5349 (2008).
99 Otieno, G. *et al.* Processing and properties of aligned multi-walled carbon nanotube/aluminoborosilicate glass composites made by sol–gel processing. *Carbon* **48**, 2212-2217 (2010).
100 Zheng, C., Feng, M., Zhen, X., Huang, J. & Zhan, H. Materials investigation of multi-walled carbon nanotubes doped silica gel glass composites. *Journal of Non-Crystalline Solids* **354**, 1327-1330 (2008).
101 Watcharotone, S. *et al.* Graphene-silica composite thin films as transparent conductors. *Nano Letters* **7**, 1888-1892 (2007).
102 Zeng, Y., Zhou, Y., Kong, L., Zhou, T. & Shi, G. A novel composite of SiO 2-coated graphene oxide and molecularly imprinted polymers for electrochemical sensing dopamine. *Biosensors and Bioelectronics* **45**, 25-33 (2013).
103 Cheng, W.-Y., Wang, C.-C. & Lu, S.-Y. Graphene aerogels as a highly efficient counter electrode material for dye-sensitized solar cells. *Carbon* **54**, 291-299 (2013).
104 Gao, L., Jiang, L. & Sun, J. Carbon nanotube-ceramic composites. *Journal of electroceramics* **17**, 51-55 (2006).
105 Kim, B.-N. *et al.* Dynamic grain growth during low-temperature spark plasma sintering of alumina. *Scr. Mater.* **80**, 29-32 (2014).
106 Zhou, Y., Hirao, K., Yamauchi, Y. & Kanzaki, S. Densification and grain growth in pulse electric current sintering of alumina. *Journal of the European Ceramic Society* **24**, 3465-3470 (2004).
107 Ahmad, I., Yazdani, B. & Zhu, Y. Recent Advances on Carbon Nanotubes and Graphene Reinforced Ceramics Nanocomposites. *Nanomaterials* **5**, 90-114 (2015).

108 Grasso, S. *et al.* Flash spark plasma sintering (FSPS) of pure ZrB2. *Journal of the American Ceramic Society* **97**, 2405-2408 (2014).
109 Langer, J., Hoffmann, M. J. & Guillon, O. Direct comparison between hot pressing and electric field-assisted sintering of submicron alumina. *Acta Materialia* **57**, 5454-5465 (2009).
110 Shen, Z., Johnsson, M., Zhao, Z. & Nygren, M. Spark plasma sintering of alumina. *Journal of the American Ceramic Society* **85**, 1921-1927 (2002).
111 Ahmad, I. & Dar, M. A. Structure and Properties of Y_2O_3-Doped Al_2O_3-MWCNT Nanocomposites Prepared by Pressureless Sintering and Hot-Pressing. *Journal of Materials Engineering and Performance* **23**, 2110-2119 (2014).
112 Zhan, G.-D. & Mukherjee, A. Processing and characterization of nanoceramic composites with interesting structural and functional properties. *Reviews on Advanced Materials Science* **10**, 185-196 (2005).
113 Sarkar, S. & Das, P. K. Microstructure and physicomechanical properties of pressureless sintered multiwalled carbon nanotube/alumina nanocomposites. *Ceramics International* **38**, 423-432 (2012).
114 Michálek, M., Bodišová, K., Michálková, M., Sedláček, J. & Galusek, D. Alumina/MWCNTs composites by aqueous slip casting and pressureless sintering. *Ceramics International* **39**, 6543-6550 (2013).
115 Ghobadi, H., Nemati, A., Ebadzadeh, T., Sadeghian, Z. & Barzegar-Bafrooei, H. Improving CNT distribution and mechanical properties of MWCNT reinforced alumina matrix. *Materials Science and Engineering: A* **617**, 110-114 (2014).
116 Tatami, J., Katashima, T., Komeya, K., Meguro, T. & Wakihara, T. Electrically Conductive CNT-Dispersed Silicon Nitride Ceramics. *Journal of the American Ceramic Society* **88**, 2889-2893 (2005).
117 Cheng, J., Agrawal, D., Zhang, Y. & Roy, R. Microwave sintering of transparent alumina. *Materials letters* **56**, 587-592 (2002).
118 Corral, E. L. *et al.* Engineered Nanostructures for Multifunctional Single-Walled Carbon Nanotube Reinforced Silicon Nitride Nanocomposites. *Journal of the American Ceramic Society* **91**, 3129-3137 (2008).
119 Wang, J., Kou, H., Liu, X., Pan, Y. & Guo, J. Reinforcement of mullite matrix with multi-walled carbon nanotubes. *Ceramics International* **33**, 719-722 (2007).
120 Pasupuleti, S. *et al.* Toughening behavior in a carbon nanotube reinforced silicon nitride composite. *Materials Science and Engineering: A* **491**, 224-229 (2008).
121 Tian, W.-B., Kan, Y.-M., Zhang, G.-J. & Wang, P.-L. Effect of carbon nanotubes on the properties of ZrB 2–SiC ceramics. *Materials Science and Engineering: A* **487**, 568-573 (2008).
122 Huang, Q., Gao, L. & Sun, J. Effect of adding carbon nanotubes on microstructure, phase transformation, and mechanical property of BaTiO3 ceramics. *Journal of the American Ceramic Society* **88**, 3515-3518 (2005).
123 Kumari, L. *et al.* Synthesis, microstructure and electrical conductivity of carbon nanotube–alumina nanocomposites. *Ceramics International* **35**, 1775-1781 (2009).
124 Echeberria, J. *et al.* Hard and tough carbon nanotube-reinforced zirconia-toughened alumina composites prepared by spark plasma sintering. *Carbon* **50**, 706-717 (2012).
125 Kim, S. W., Chung, W. S., Sohn, K.-S., Son, C.-Y. & Lee, S. Improvement of flexure strength and fracture toughness in alumina matrix composites reinforced with carbon nanotubes. *Materials Science and Engineering: A* **517**, 293-299 (2009).
126 Hanzel, O., Sedláček, J. & Šajgalík, P. New approach for distribution of carbon nanotubes in alumina matrix. *Journal of the European Ceramic Society* **34**, 1845-1851 (2014).
127 Michálek, M., Sedláček, J., Parchoviansky, M., Michálková, M. & Galusek, D. Mechanical properties and electrical conductivity of alumina/MWCNT and alumina/zirconia/MWCNT composites. *Ceramics International* **40**, 1289-1295 (2014).

128 Poyato, R. *et al.* Effect of high SWNT content on the room temperature mechanical properties of fully dense 3YTZP/SWNT composites. *Journal of the European Ceramic Society* **34**, 1571-1579 (2014).
129 Bakhsh, N., Khalid, F. & Hakeem, A. S. in *IOP Conference Series: Materials Science and Engineering.* 012059 (IOP Publishing).
130 Zhang, S. C., Fahrenholtz, W. G., Hilmas, G. E. & Yadlowsky, E. J. Pressureless sintering of carbon nanotube–Al 2 O 3 composites. *Journal of the European Ceramic Society* **30**, 1373-1380 (2010).
131 Rutkowski, P., Stobierski, L. & Górny, G. Thermal stability and conductivity of hot-pressed Si3N4–graphene composites. *Journal of Thermal Analysis and Calorimetry* **116**, 321-328 (2014).
132 Tapaszto, O. *et al.* Silicon nitride based nanocomposites produced by two different sintering methods. *Ceramics International* **37**, 3457-3461 (2011).
133 Kvetková, L. *et al.* Influence of processing on fracture toughness of Si< sub> 3</sub> N< sub> 4</sub>+ graphene platelet composites. *Journal of the European Ceramic Society* **33**, 2299-2304 (2013).
134 Zhan, G. D. & Mukherjee, A. K. Carbon Nanotube Reinforced Alumina-Based Ceramics with Novel Mechanical, Electrical, and Thermal Properties. *International Journal of Applied Ceramic Technology* **1**, 161-171 (2004).
135 Ahmad, I., Islam, M., Almajid, A. A., Yazdani, B. & Zhu, Y. Investigation of yttria-doped alumina nanocomposites reinforced by multi-walled carbon nanotubes. *Ceramics International* **40**, 9327-9335 (2014).
136 Ahmad, I., Kennedy, A. & Zhu, Y. Wear resistant properties of multi-walled carbon nanotubes reinforced Al 2 O 3 nanocomposites. *Wear* **269**, 71-78 (2010).
137 Estili, M. *et al.* The homogeneous dispersion of surfactantless, slightly disordered, crystalline, multiwalled carbon nanotubes in α-alumina ceramics for structural reinforcement. *Acta Materialia* **56**, 4070-4079 (2008).
138 Yazdani, B., Xia, Y., Ahmad, I. & Zhu, Y. Graphene and carbon nanotube (GNT)-reinforced alumina nanocomposites. *Journal of the European Ceramic Society* (2014).
139 Hiura, H., Ebbesen, T. W. & Tanigaki, K. Opening and purification of carbon nanotubes in high yields. *Advanced Materials* **7**, 275-276 (1995).
140 Wang, Y., Voronin, G., Zerda, T. & Winiarski, A. SiC–CNT nanocomposites: high pressure reaction synthesis and characterization. *Journal of Physics: Condensed Matter* **18**, 275 (2006).
141 Estili, M., Kawasaki, A. & Sakka, Y. Highly concentrated 3D macrostructure of individual carbon nanotubes in a ceramic environment. *Advanced Materials* **24**, 4322-4326 (2012).
142 Martinelli, J. & Sene, F. Electrical resistivity of ceramic–metal composite materials: application in crucibles for induction furnaces. *Ceramics International* **26**, 325-335 (2000).
143 Puchy, V. *et al.* Wear resistance of Al 2 O 3–CNT ceramic nanocomposites at room and high temperatures. *Ceramics International* **39**, 5821-5826 (2013).
144 Lee, K., Mo, C. B., Park, S. B. & Hong, S. H. Mechanical and Electrical Properties of Multiwalled CNT-Alumina Nanocomposites Prepared by a Sequential Two-Step Processing of Ultrasonic Spray Pyrolysis and Spark Plasma Sintering. *Journal of the American Ceramic Society* **94**, 3774-3779 (2011).
145 Thomson, K., Jiang, D., Yao, W., Ritchie, R. & Mukherjee, A. Characterization and mechanical testing of alumina-based nanocomposites reinforced with niobium and/or carbon nanotubes fabricated by spark plasma sintering. *Acta Materialia* **60**, 622-632 (2012).
146 Sarkar, S. & Das, P. K. Effect of sintering temperature and nanotube concentration on microstructure and properties of carbon nanotube/alumina nanocomposites. *Ceramics International* **40**, 7449-7458 (2014).

147 Zaman, A. C., Üstündağ, C. B., Kaya, F. & Kaya, C. OH and COOH functionalized single walled carbon nanotubes-reinforced alumina ceramic nanocomposites. *Ceramics International* **38**, 1287-1293 (2012).
148 Bi, S. *et al.* Electrical conductivity and microwave absorption of shortened multi-walled carbon nanotube/alumina ceramic composites. *Ceramics International* **39**, 5979-5983 (2013).
149 Che, J., Cagin, T. & Goddard III, W. A. Thermal conductivity of carbon nanotubes. *Nanotechnology* **11**, 65 (2000).
150 Bakshi, S. R., Balani, K. & Agarwal, A. Thermal Conductivity of Plasma-Sprayed Aluminum Oxide—Multiwalled Carbon Nanotube Composites. *Journal of the American Ceramic Society* **91**, 942-947 (2008).
151 Cho, J., Boccaccini, A. R. & Shaffer, M. S. Ceramic matrix composites containing carbon nanotubes. *Journal of Materials Science* **44**, 1934-1951 (2009).
152 Quinn, G. D. & Bradt, R. C. On the Vickers indentation fracture toughness test. *Journal of the American Ceramic Society* **90**, 673-680 (2007).
153 Zhu, Y. *et al.* A seamless three-dimensional carbon nanotube graphene hybrid material. *Nature Communications* **3**, 1225 (2012).
154 Hu, H., Zhao, Z., Gogotsi, Y. & Qiu, J. Compressible Carbon Nanotube–Graphene Hybrid Aerogels with Superhydrophobicity and Superoleophilicity for Oil Sorption. *Environmental Science & Technology Letters* **1**, 214-220 (2014).
155 Shen, X.-J., Pei, X.-Q., Liu, Y. & Fu, S.-Y. Tribological performance of carbon nanotube–graphene oxide hybrid/epoxy composites. *Composites Part B: Engineering* **57**, 120-125 (2014).
156 Zhang, C., Huang, S., Tjiu, W. W., Fan, W. & Liu, T. Facile preparation of water-dispersible graphene sheets stabilized by acid-treated multi-walled carbon nanotubes and their poly (vinyl alcohol) composites. *Journal of Materials Chemistry* **22**, 2427-2434 (2012).
157 Huang, Z.-D., Liang, R., Zhang, B., He, Y.-B. & Kim, J.-K. Evolution of flexible 3D graphene oxide/carbon nanotube/polyaniline composite papers and their supercapacitive performance. *Composites Science and Technology* **88**, 126-133 (2013).
158 Wang, P.-N., Hsieh, T.-H., Chiang, C.-L. & Shen, M.-Y. Synergetic Effects of Mechanical Properties on Graphene Nanoplatelet and Multiwalled Carbon Nanotube Hybrids Reinforced Epoxy/Carbon Fiber Composites. *Journal of Nanomaterials* (2015).
159 Yang, S.-Y. *et al.* Synergetic effects of graphene platelets and carbon nanotubes on the mechanical and thermal properties of epoxy composites. *Carbon* **49**, 793-803 (2011).
160 Zhang, W.-b. *et al.* Largely enhanced thermal conductivity of poly (vinylidene fluoride)/carbon nanotube composites achieved by adding graphene oxide. *Carbon* **90**, 242-254 (2015).
161 Ritchie, R. O. & Dzenis, Y. A. The Quest for Stronger, Tougher Materials: A Letter and a Response. (2008).
162 Curtin, W. A. & Sheldon, B. W. CNT-reinforced ceramics and metals. *Materials Today* **7**, 44-49 (2004).
163 Kramer, D., White, K. & Kelly, M. in *Proceedings of the 6th Annual Conference on Composites and Advanced Ceramic Materials: Ceramic Engineering and Science Proceedings, Volume 3, Issue 9/10.* 512-518 (Wiley Online Library).
164 Tajima, Y. in *MRS Proceedings.* 189 (Cambridge Univ Press).
165 Evans, A. G. Perspective on the development of high-toughness ceramics. *Journal of the American Ceramic Society* **73**, 187-206 (1990).
166 Komeya, K., Matsuo, Y., Goto, T. & Tatami, J. in *Ceramic Engineering and Science Proceedings.* 1-15 (American Ceramic Society, Inc., 735 Ceramic Place Westerville OH 43081 United States).

167 Huang, Q. & Gao, L. Manufacture and electrical properties of multiwalled carbon nanotube/$BaTiO_3$ nanocomposite ceramics. *Journal of Materials Chemistry* **14**, 2536-2541 (2004).
168 Jõgi, I. *et al.* Atomic layer deposition of high capacitance density Ta_2O_5–ZrO_2 based dielectrics for metal–insulator–metal structures. *Microelectronic Engineering* **87**, 144-149 (2010).
169 Duszová, A., Dusza, J., Tomášek, K., Blugan, G. & Kuebler, J. Microstructure and properties of carbon nanotube/zirconia composite. *Journal of the European Ceramic Society* **28**, 1023-1027 (2008).
170 Patsalas, P. & Logothetidis, S. Optical, electronic, and transport properties of nanocrystalline titanium nitride thin films. *Journal of Applied Physics* **90**, 4725-4734 (2001).
171 Carmalt, C. *et al.* Titanium (IV) azido and imido complexes as potential precursors to titanium nitride. *Journal of the Chemical Society, Dalton Transactions*, 553-558 (1998).
172 Janes, R. A., Aldissi, M. & Kaner, R. B. Controlling surface area of titanium nitride using metathesis reactions. *Chemistry of Materials* **15**, 4431-4435 (2003).
173 Kim, I.-s. & Kumta, P. N. Hydrazide sol–gel synthesis of nanostructured titanium nitride: precursor chemistry and phase evolution. *Journal of Materials Chemistry* **13**, 2028-2035 (2003).
174 Cao, M. *et al.* Preparing γ'-Fe 4 N ultrafine powder by twice-nitriding method. *Powder technology* **115**, 96-98 (2001).
175 Chen, J., Chen, Q. & Ma, Q. Influence of surface functionalization via chemical oxidation on the properties of carbon nanotubes. *Journal of colloid and interface science* **370**, 32-38 (2012).
176 Marcano, D. C. *et al.* Improved synthesis of graphene oxide. *ACS Nano* **4**, 4806-4814 (2010).
177 Watt, I. M. *The principles and practice of electron microscopy*. (Cambridge University Press, 1997).
178 Cullity, B. D. & Stock, S. R. *Elements of X-ray Diffraction*. Vol. 3 (Prentice hall Upper Saddle River, NJ, 2001).
179 Demtröder, W. *Laser spectroscopy: basic concepts and instrumentation*. (Springer Science & Business Media, 2013).
180 Bengisu, M. *Engineering ceramics*. (Springer Science & Business Media, 2013).
181 Shen, T. K. & Hing, P. Ultrasonic through-transmission method of evaluating the modulus of elasticity of Al_2O_3–ZrO_2 composite. *Journal of Materials Science* **32**, 6633-6638 (1997).
182 Maensiri, S., Laokul, P., Klinkaewnarong, J. & Amornkitbamrung, V. Carbon nanofiber-reinforced alumina nanocomposites: Fabrication and mechanical properties. *Materials Science and Engineering: A* **447**, 44-50 (2007).
183 Advanced, S. T. M. f. t. D. o. F. T. o. & Temperat, C. M. a. A. in *ASTM Designation C 1421–99* (Annual Book of Standards, Vol. 15.01, Annual Book of Standards, Vol. 15.01, 2011).
184 Boccaccini, A. R. The relationship between wear behaviour and brittleness index in engineering ceramics and dispersion-reinforced ceramic composites. *Interceram* **48**, 176-187 (1999).
185 Committee, J. I. S. (Japanese Standard Association, Tokyo, Japan 1993).
186 Inam, F., Peijs, T. & Reece, M. J. The production of advanced fine-grained alumina by carbon nanotube addition. *Journal of the European Ceramic Society* **31**, 2853-2859 (2011).
187 Milsom, B. *et al.* The effect of carbon nanotubes on the sintering behaviour of zirconia. *Journal of the European Ceramic Society* **32**, 4149-4156 (2012).
188 Inam, F., Yan, H., Peijs, T. & Reece, M. J. The sintering and grain growth behaviour of ceramic–carbon nanotube nanocomposites. *Composites Science and Technology* **70**, 947-952 (2010).
189 Rice, R. W. *Mechanical properties of ceramics and composites: grain and particle effects*. Vol. 17 (CRC Press, 2000).

190 Aman, Y., Garnier, V. & Djurado, E. Spark Plasma Sintering Kinetics of Pure α-Alumina. *Journal of the American Ceramic Society* **94**, 2825-2833 (2011).
191 MURAYAMA, N. & SHIN, W. Effect of rapid heating on densification and grain growth in hot pressed alumina. *Nippon seramikkusu kyokai gakujutsu ronbunshi* **108**, 799-802 (2000).
192 Aman, Y., Garnier, V. & Djurado, E. A screening design approach for the understanding of spark plasma sintering parameters: a case of translucent polycrystalline undoped alumina. *International Journal of Applied Ceramic Technology* **7**, 574-586 (2010).
193 Nishida, T., Hanaki, Y. & Pezzotti, G. Effect of Notch-Root Radius on the Fracture Toughness of a Fine-Grained Alumina. *Journal of the American Ceramic Society* **77**, 606-608 (1994).
194 Demczyk, B. *et al.* Direct mechanical measurement of the tensile strength and elastic modulus of multiwalled carbon nanotubes. *Materials Science and Engineering: A* **334**, 173-178 (2002).
195 Yazdani, B., Xia, Y., Ahmad, I. & Zhu, Y. Graphene and carbon nanotube (GNT)-reinforced alumina nanocomposites. *Journal of the European Ceramic Society* **35**, 179-186 (2015).
196 Ahmad, I., Kennedy, A. & Zhu, Y. Wear resistant properties of multi-walled carbon nanotubes reinforced Al_2O_3 nanocomposites. *Wear* **269**, 71-78 (2010).
197 Ferrari, A. *et al.* Raman spectrum of graphene and graphene layers. *Physical review letters* **97**, 187401 (2006).
198 Porwal, H. *et al.* Tribological properties of silica–graphene nano-platelet composites. *Ceramics International* (2014).
199 Belmonte, M. *et al.* The beneficial effect of graphene nanofillers on the tribological performance of ceramics. *Carbon* **61**, 431-435 (2013).
200 Stankovich, S. *et al.* Synthesis of graphene-based nanosheets via chemical reduction of exfoliated graphite oxide. *Carbon* **45**, 1558-1565 (2007).
201 Chen, Y., Zhang, X., Zhang, D., Yu, P. & Ma, Y. High performance supercapacitors based on reduced graphene oxide in aqueous and ionic liquid electrolytes. *Carbon* **49**, 573-580 (2011).
202 Bo, Z. *et al.* Green preparation of reduced graphene oxide for sensing and energy storage applications. *Scientific reports* **4** (2014).
203 Wang, H., Robinson, J. T., Li, X. & Dai, H. Solvothermal reduction of chemically exfoliated graphene sheets. *Journal of the American Chemical Society* **131**, 9910-9911 (2009).
204 Bose, S., Kuila, T., Mishra, A. K., Kim, N. H. & Lee, J. H. Dual role of glycine as a chemical functionalizer and a reducing agent in the preparation of graphene: an environmentally friendly method. *Journal of Materials Chemistry* **22**, 9696-9703 (2012).
205 Boumaza, A. *et al.* Transition alumina phases induced by heat treatment of boehmite: an X-ray diffraction and infrared spectroscopy study. *Journal of solid state chemistry* **182**, 1171-1176 (2009).
206 Nordahl, C. S. & Messing, G. L. Sintering of α-Al_2O_3-seeded nanocrystalline γ-Al_2O_3 powders. *Journal of the European Ceramic Society* **22**, 415-422 (2002).
207 You, X. *et al.* Effect of grain size on thermal shock resistance of Al_2O_3–TiC ceramics. *Ceramics International* **31**, 33-38 (2005).
208 Hall, E. The deformation and ageing of mild steel: III discussion of results. *Proceedings of the Physical Society. Section B* **64**, 747 (1951).
209 Petch, N. The cleavage strength of polycrystals. *J. Iron Steel Inst.* **174**, 25-28 (1953).
210 Yang, D. *et al.* Chemical analysis of graphene oxide films after heat and chemical treatments by X-ray photoelectron and Micro-Raman spectroscopy. *Carbon* **47**, 145-152 (2009).